United States Department of Commerce
Technology Administration
National Institute of Standards and Technology

NIST Technical Note 1500-5
Materials Reliability Series

Electron-Beam Moiré Technique: Advances, Verification, Application

E.S. Drexler

NIST Technical Note 1500-5
Materials Reliability Series

Electron-Beam Moiré Technique: Advances, Verification, Application

E.S. Drexler

Materials Reliability Division
Materials Science and Engineering Laboratory
National Institute of Standards and Technology
325 Broadway
Boulder, Colorado 80303-3328

August 1998

U.S. DEPARTMENT OF COMMERCE, William M. Daley, Secretary
TECHNOLOGY ADMINISTRATION, Gary R. Bachula, Acting Under Secretary for Technology
NATIONAL INSTITUTE OF STANDARDS AND TECHNOLOGY, Raymond G. Kammer, Director

National Institute of Standards and Technology Technical Note
Natl. Inst. Stand. Technol., Tech. Note 1500-5, 76 pages (August 1998)
CODEN:NTNOEF

U.S. GOVERNMENT PRINTING OFFICE
WASHINGTON: 1998

For sale by the Superintendent of Documents, U.S. Government Printing Office, Washington, DC 20402-9325

Contents

Foreword

The Materials Reliability Series of NIST Technical Notes are reports covering significant research accomplishments of the Materials Reliability Division. The Division develops measurement technologies that enable the producers and users of materials to improve the quality and reliability of their products. Measurement technologies are developed for process control to improve the quality and consistency of materials, for nondestructive evaluation to assure quality of finished materials and products, and for materials evaluation to assure reliable performance. Within these broad areas of measurement technology, the Division has focused its resources on three research themes:

- Intelligent Processing of Materials—To develop on-line sensors for measuring the materials' characteristics and/or processing conditions needed for real-time process control.

- Ultrasonic Characterization of Materials—To develop ultrasonic measurements for characterizing internal geometries of materials, such as defects, microstructures, and lattice distortions.

- Micrometer-Scale Measurements for Materials Evaluation—To develop measurement techniques for evaluating the mechanical, thermal, and magnetic behavior of thin films and coatings at the appropriate size scale.

This report is the fifth in the Materials Reliability Series. It covers recent developments in the electron-beam moiré technique, and the description of a series of mechanical and thermal tests conducted using electron-beam moiré. Previous reports in this series are:

Technical Note 1500-1 Tensile Testing of Thin Films: Techniques and Results, by D.T. Read, 1997

Technical Note 1500-2 Procedures for the Electron-Beam Moiré Technique, by E.S. Drexler, 1998

Technical Note 1500-3 High-Energy, Transmission X-ray Diffraction for Monitoring Turbine-Blade Solidification, by D.W. Fitting, W.P. Dubé, and T.A. Siewert, 1998

Technical Note 1500-4 Nondestructive Characterization of Reactor Pressure Vessel Steels: A Feasibility Study, by H.I. McHenry and G.A. Alers, 1998

Electron-Beam Moiré Technique: Advances, Verification, Application

Elizabeth S. Drexler

Materials Reliability Division
National Institute of Standards and Technology
Boulder, CO 80303

The electron-beam moiré technique was used to measure thermal and mechanical deformation of two isotropically conductive adhesives, one a paste and the other a film. This technique has been developed and used at the National Institute of Standards and Technology in Boulder to study very small deformations in a scanning electron microscope. Efforts were made to determine the source and magnitude of the error associated with this technique and its effect on the measurement resolution. This study compared paste and film conductive adhesives subjected to thermal and mechanical loading. Both conductive adhesives performed well in the temperature range –50 to 150 °C. However, their internal strains increased as temperatures exceeded their glass transition temperatures. The paste performed better than the film in the modified lap-shear test. At ~700 N, it failed cohesively near the interface with the copper. At loads as low as 325 N, the film showed signs of failure at the interface between the silver conducting particles and the epoxy matrix.

Key words: electron-beam lithography; electron-beam moiré; isotropically conductive adhesives; mechanical deformation; thermal deformation

1. Introduction

The choices for resolving displacements on the order of tens of nanometers are limited. If displacement must be correlated to microstructure, even fewer experimental techniques are available. One such technique is electron-beam (e-beam) moiré. This technique was recently developed at the National Institute of Standards and Technology (NIST) in Boulder to measure two-dimensional, in-plane displacements, from which strains can be calculated. With resolutions on the order of tens of nanometers and a specimen grating that is transparent to the microstructure, this technique is versatile and powerful.

Briefly, e-beam lithography is used to imprint a grating onto the cross section of a specimen. Under a scanning electron microscope (SEM), the interference between the specimen grating and the rastering of the electron beam of the SEM produces a moiré pattern. The specimen in the microscope is loaded either thermally or mechanically, and the changes in the moiré patterns are recorded and measured.

In this study, the source and magnitude of the error associated with the e-beam moiré technique were investigated first. Particular attention was paid to a series of tests that indicated that the apparent magnification was changing over time. The source of this temporal variation was never isolated; as a result, the error is unavoidable and, as such, is presumed to be present.

To verify the usefulness of the technique, four tests were conducted to measure the thermal expansion coefficient of copper in the temperature range –50 to 150 °C. The values obtained from four tests were within 21 percent of handbook values.

Then the e-beam moiré technique was applied to copper/conductive-adhesive specimens subjected to mechanical and thermal loads. The hazardous nature of lead in today's solder, along with the growing need to decrease the pitch between leads in electronic packages, has turned the attention of industry toward conductive adhesives (CAs) in its search for a replacement for solder. Although CAs have been used in electronics for decades, the materials have not been fully characterized as replacements for solder. Industry has been assessing the suitability of these CAs by using a pass/fail criterion based on the volume resistivity of the package. However, failure modes, or even failure sites, are not revealed by this evaluation.

To gain insight as to how and why CAs fail, an e-beam moiré study was undertaken on two different CA materials, one a paste and the other a film. Four specimens were assembled and tested. One specimen of each type of material was thermally loaded between –50 and 150 °C, and a second specimen of each material was mechanically loaded to failure. Throughout each test, images of the moiré fringe field were acquired and compared with the initial unloaded image to identify and measure displacements, even on a local scale.

2. Methods of Displacement Measurement

2.1 Background

The moiré effect can be found in any number of circumstances. The effect is seen when two snow fences are viewed one in front of the other, when window screens are stacked, or when persons on television wear striped clothing. The term moiré comes from the patterned fabric that displays this effect of light and dark fringes. In experimental mechanics, displacements are studied by using two nominally identical grids or gratings, with the specimen grating viewed through the reference grating. As deformation occurs in the specimen, the two gratings no longer coincide, and the mismatch produces fringes.

The history of the experimental technique known as moiré is brief. In 1945 a Dutch scientist, D. Tollenaar, published the first account of the moiré effect [1]. Publication of Weller and Shepard's work, in which the moiré effect was used to measure displacements, followed in 1948 [2]. In the 1950s, several groups [3–7] contributed to the geometric analysis of moiré fringes, their spacing, inclination, and so on; strain analysis using moiré; and components of displacement. Since that time the pioneers in moiré strain analysis have been Durelli and Sciammarella (beginning in the early 1960s), Parks (mid-1960s), Theocaris (1960s), and Post (1960s and in the late 1970s), who introduced moiré interferometry.

2.2 Geometric Moiré

Mechanical or geometric moiré is the traditional moiré technique that uses two physical gratings, the reference grating and the specimen grating, with equally spaced light and dark lines. Traditionally, transparent film is used for the reference grating, and a bondable grating is used for the specimen grating. The specimen grating is viewed through the reference grating. When the gratings match perfectly, the superimposed image looks like the surface of the specimen with half the light intensity (see fig. 1). If mismatch occurs between the two gratings, the interference of the lines of the gratings produces fringes (see fig. 2).

The gratings can be produced in one dimension or two and can be linear or circular. The distance between the center of one line on the grating to the center of the adjacent line is called the *pitch* (p). The pitch used for the gratings is usually small with respect to the resolution of the viewing technique. That is, the technique is most useful in resolving small displacements over the area viewed. The pitch of the reference grating p_r typically equals the pitch of the specimen grating p_s in the initial (unstressed) condition. Upon loading, p_s changes in some or all parts of the specimen, depending on the load and the elastic modulus of the material or materials.

The direction perpendicular to the grating lines is called the *primary* direction; the *secondary* direction is parallel to the grating lines. A moiré fringe in the primary direction is produced when the deformation in the specimen perpendicular to the grating lines is equal in magnitude to p_r. Let us assume that the specimen depicted in figure 2 is in tension and uniformly deformed. The reference grating has 15 lines in the field of view. The specimen has only 12.5 lines remaining in the field of view. As light tries to pass through these gratings, it is blocked by lines from both gratings at regular intervals, but not at the same interval. Broad bands of low light intensity result in the dark moiré fringes. In this situation there are 2.5 fringes—the difference in the number of lines between the reference and specimen gratings in the field of view.

The most common method for obtaining moiré fringes is to begin with reference and specimen gratings having the same initial pitch. However, when p_s is nearly an even multiple of p_r, fringes that are called *fringes of multiplication* form. *Fringes of division* form when p_r/p_s is approximately a whole number greater than 1.

In a uniform strain field, if n_f is the number of fringes, then

$$\Delta l = n_f p_r, \tag{1}$$

where Δl is the change in length of the specimen in the primary direction. Therefore, if n_l is the number of lines in the reference grating, the engineering strain is

$$\varepsilon_e = \Delta l / l = n_f p_r / n_l p_r = n_f / n_l. \tag{2}$$

This equation for strain is valid only in a uniform deformation field in the primary direction with no rotation of fringes.

Moiré fringes can also be formed by rotating the specimen grating with respect to the reference grating. Figure 3 is an example of moiré fringes due to rigid-body rotation. If θ

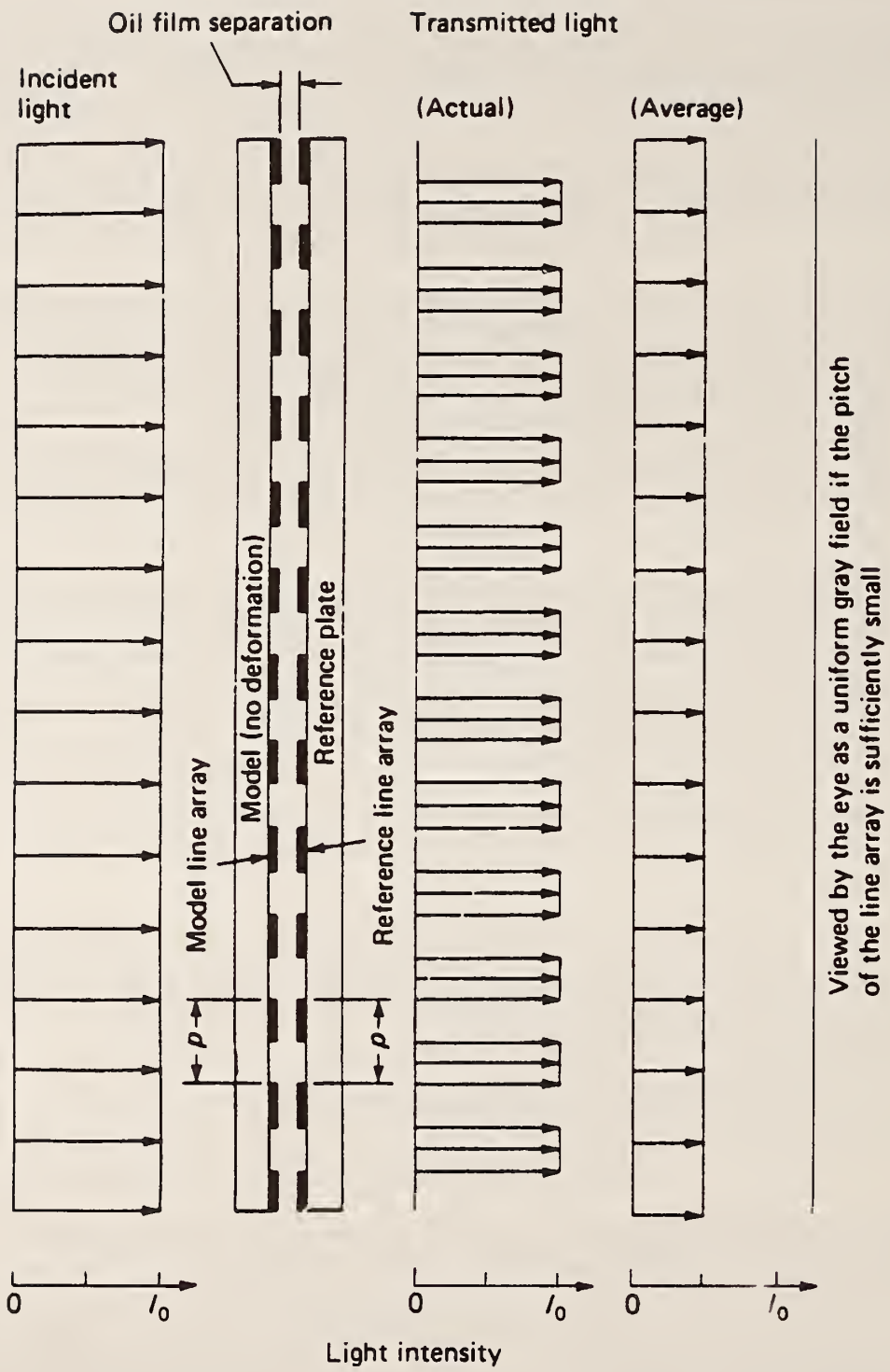

Figure 1. Schematic of light transmission through a specimen and reference grating when $p_r = p_s$. (From J.W. Dally and W.F. Riley, Moiré methods, chapter 11 in *Experimental Stress Analysis*. New York: McGraw–Hill; 1991 [8]. Used with permission of McGraw–Hill.)

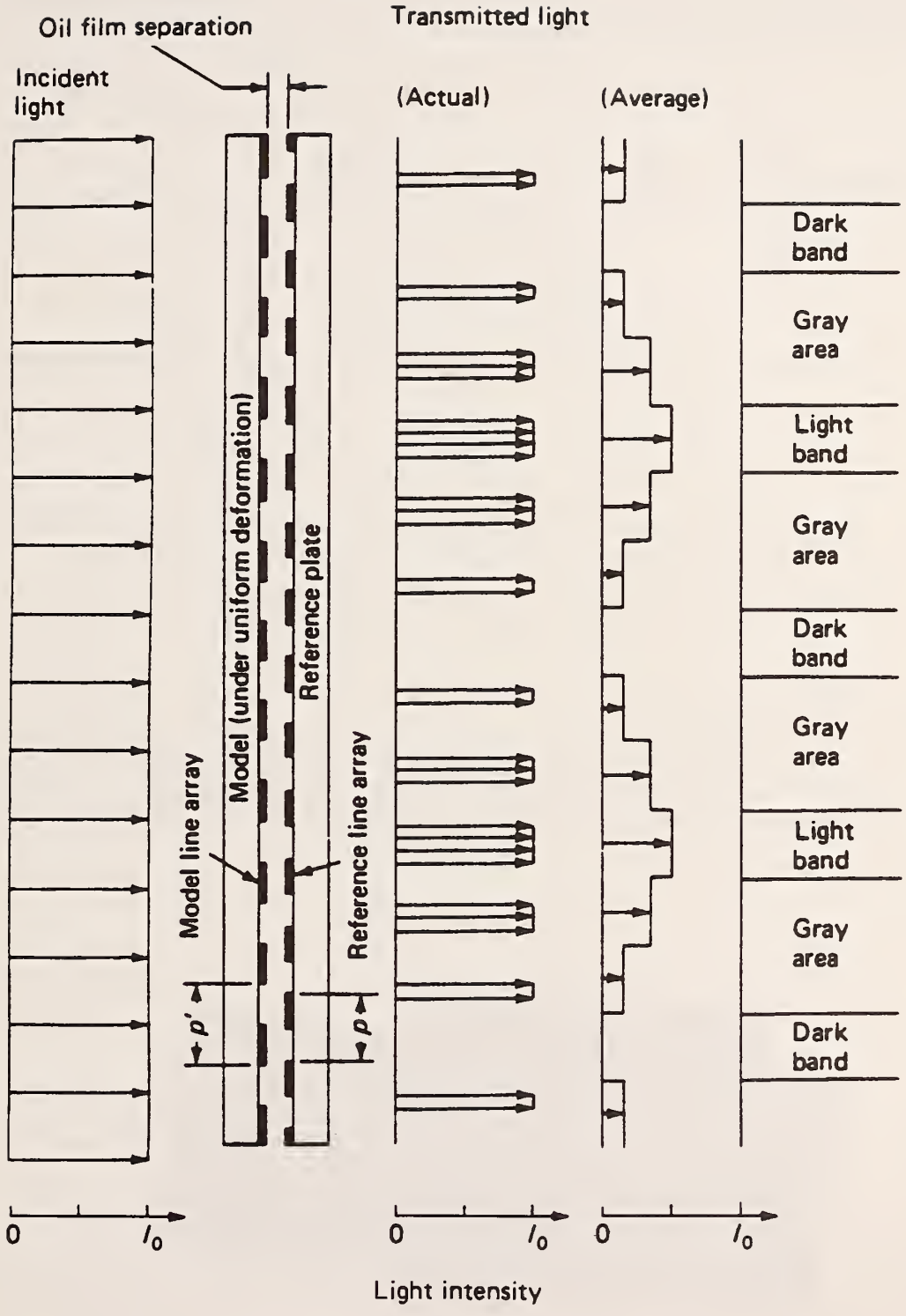

Figure 2. Schematic of light transmission through a specimen and reference grating when $p_r \neq p_s$. (From J.W. Dally and W.F. Riley, Moiré methods, chapter 11 in *Experimental Stress Analysis*. New York: McGraw–Hill; 1991 [8]. Used with permission of McGraw–Hill.)

is the angle of rotation between the two gratings and ϕ is the angle between the lines of the reference grating and the moiré fringes, then

$$\phi = \frac{\pi}{2} + \frac{\theta}{2}. \tag{3}$$

The distance δ between fringes, as shown in figure 4, is [9]

$$\delta = \frac{p}{2 \sin \frac{\theta}{2}}. \tag{4}$$

The most general case of strain under large deformations and rotations can be represented by

$$\varepsilon_x = \left[1 + 2\frac{\partial u}{\partial x} + \left[\frac{\partial u}{\partial x}\right]^2 + \left[\frac{\partial v}{\partial x}\right]^2 + \left[\frac{\partial w}{\partial x}\right]^2 \right]^{1/2} - 1, \tag{5}$$

$$\varepsilon_y = \left[1 + 2\frac{\partial v}{\partial y} + \left[\frac{\partial v}{\partial y}\right]^2 + \left[\frac{\partial w}{\partial y}\right]^2 + \left[\frac{\partial u}{\partial y}\right]^2 \right]^{1/2} - 1, \tag{6}$$

and

$$\gamma_{xy} = \arcsin \frac{\frac{\partial u}{\partial y} + \frac{\partial v}{\partial x} + \frac{\partial u}{\partial x}\frac{\partial u}{\partial y} + \frac{\partial v}{\partial x}\frac{\partial v}{\partial y} + \frac{\partial w}{\partial x}\frac{\partial w}{\partial y}}{(1 + \varepsilon_x)(1 + \varepsilon_y)}, \tag{7}$$

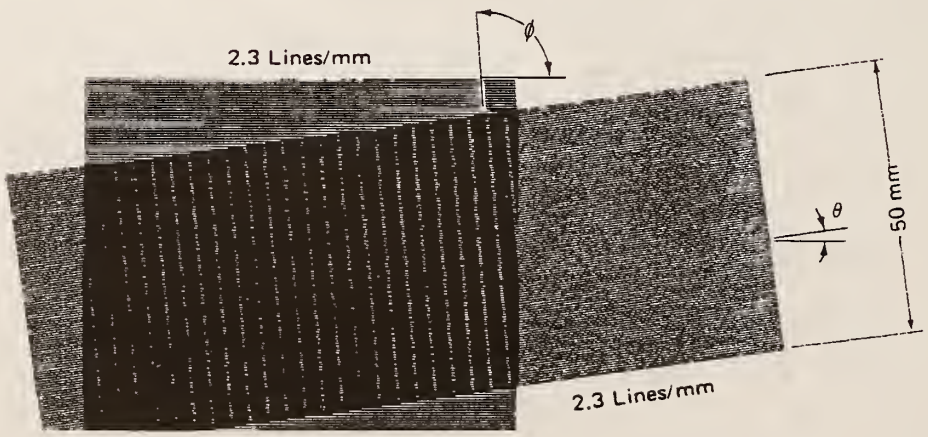

Figure 3. Moiré fringes formed when one grating is rotated with respect to the other. (From J.W. Dally and W.F. Riley, Moiré methods, chapter 11 in *Experimental Stress Analysis*. New York: McGraw–Hill; 1991 [8]. Used with permission of McGraw–Hill.)

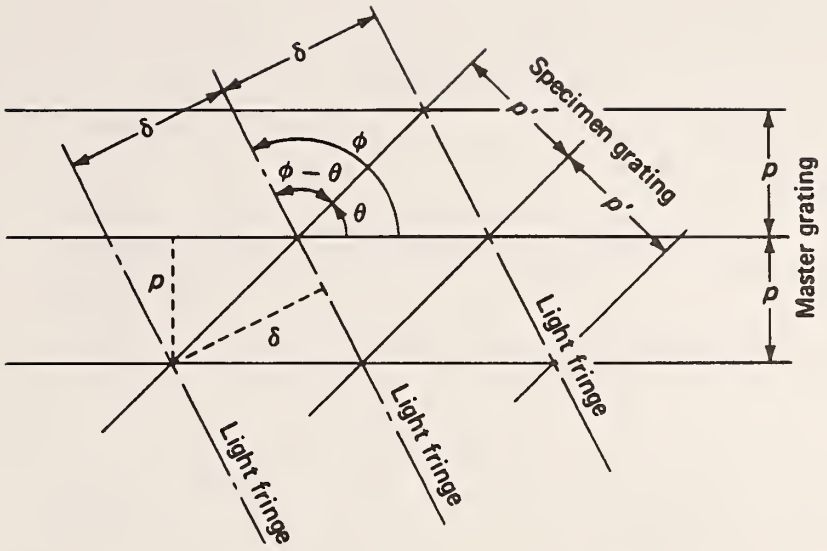

Figure 4. Geometry of moiré fringes in terms of fringe spacing. (From J.W. Dally and W.F. Riley, Moiré methods, chapter 11 in *Experimental Stress Analysis*. New York: McGraw–Hill; 1991 [8]. Used with permission of McGraw–Hill.)

where u, v, and w are the displacement components in the x, y, and z directions, respectively; ε_x and ε_y are the normal strains in the x and y directions; and γ_{xy} is the engineering shear strain. Simplifications to these equations are immediately apparent. Since out-of-plane displacements are not being measured, displacement components in the z direction will be neglected. In cases of small rotations (< 5°) and small strains, the equations for normal strain reduce to

$$\varepsilon_x = \frac{\partial u}{\partial x} \quad \text{and} \quad \varepsilon_y = \frac{\partial v}{\partial y}. \tag{8}$$

For small rotations, the equation for shear strain becomes [9]

$$\gamma_{xy} = \arcsin \left[\frac{\dfrac{\partial u}{\partial y}}{1 + \dfrac{\partial v}{\partial y}} + \frac{\dfrac{\partial v}{\partial x}}{1 + \dfrac{\partial u}{\partial x}} \right]. \tag{9}$$

When strains are small (< 2 percent) and rotations are not, the second power of the strain is small with respect to the strain itself, and the equations reduce to

$$\varepsilon_x = \frac{\partial u}{\partial x} + \frac{1}{2} \left[\left(\frac{\partial u}{\partial x} \right)^2 + \left(\frac{\partial v}{\partial x} \right)^2 \right] \tag{10}$$

and

$$\varepsilon_y = \frac{\partial v}{\partial y} + \frac{1}{2}\left[\left(\frac{\partial v}{\partial y}\right)^2 + \left(\frac{\partial u}{\partial y}\right)^2\right] \tag{11}$$

for the normal strains and to

$$\gamma_{xy} = \frac{\partial u}{\partial y} + \frac{\partial v}{\partial x} + \left[\frac{\partial u}{\partial x}\right]\left[\frac{\partial u}{\partial y}\right] + \left[\frac{\partial v}{\partial x}\right]\left[\frac{\partial v}{\partial y}\right] \tag{12}$$

for the shear strain. This equation reduces further to

$$\gamma_{xy} = \frac{\partial v}{\partial x} + \frac{\partial u}{\partial y} \tag{13}$$

when the strains are small [9].

When both small rotations and small strains are evinced, eqs (8) and (13) prevail. For the majority of work conducted at high magnification, these conditions predominate.

Reducing the moiré data, therefore, requires measuring displacements with respect to position. The moiré fringe is a contour of constant displacement whose magnitude is

$$u = N_f p_r, \tag{14}$$

where N_f is the fringe order. The slope of the displacement-versus-position curve at any place on the curve yields the value for strain at that location. Values of displacement obtained perpendicular to the lines of the reference grating provide values for normal strains, and displacements obtained from line traces oriented parallel to the lines of the reference grating contribute to the shear strains.

2.3 Moiré Interferometry

Moiré interferometry uses the interference properties of light instead of a physical reference grating. Currently available lasers yield a resolution of ~400 nm per fringe order [10]. Figure 5 is a schematic of a configuration used for moiré interferometry. The grating placed on the surface of the specimen is usually produced by exposing a photographic plate to an interference pattern created from a single wavelength (λ) of light from a laser; figures 6 and 7 show the process. The actual grating is an adhesive that bonds the mold to the specimen surface. After curing, the mold is removed, leaving the shape and the mirrored surface from the mold on the specimen surface [10].

The moiré pattern is formed when a beam splitter and mirror are used to illuminate the specimen grating with two symmetrically oblique beams of coherent light. The two beams diffract off the specimen grating (see fig. 5), and the +1 and −1 diffraction orders are recorded on a photographic plate. When the specimen is deformed, the diffracted beams intersect, interfering constructively and destructively and forming a moiré fringe field [10].

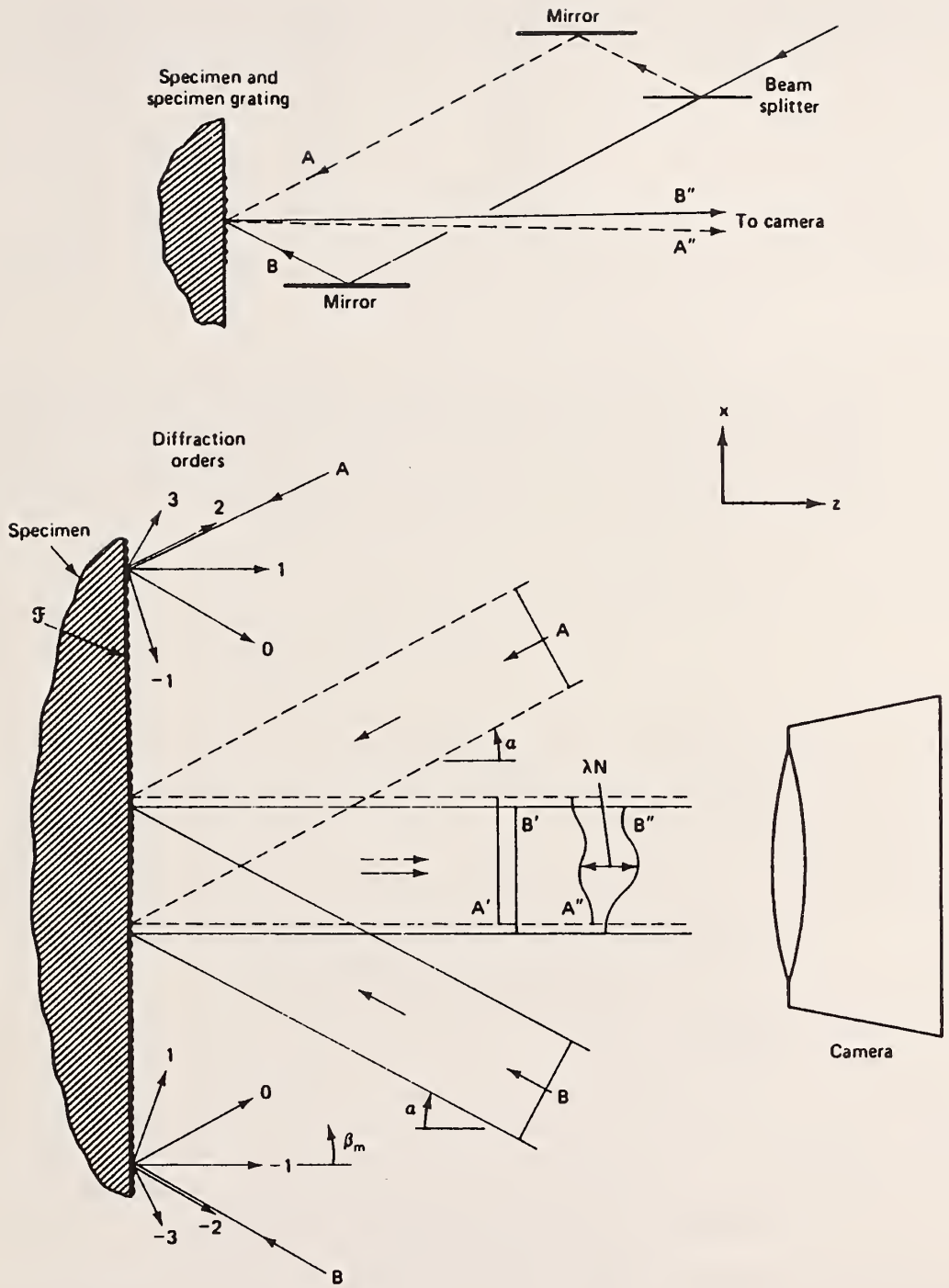

Figure 5. Schematic of configuration used in moiré interferometry. $\mathcal{J} = 1/p$. (From D. Post, Moiré interferometry, in *Handbook on Experimental Mechanics,* edited by A.S. Kobayashi, first edition, published for the Society for Experimental Mechanics, Inc., Englewood Cliffs, NJ: Prentice–Hall; 1987 [10]. Used with permission of Prentice–Hall.)

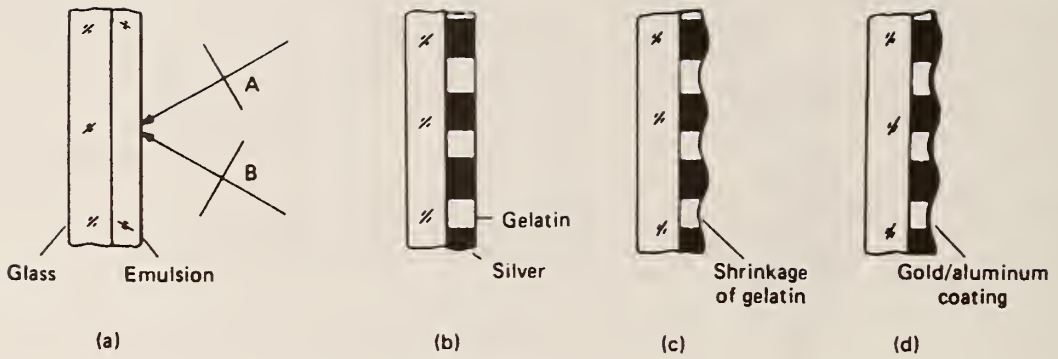

Figure 6. Process for making the mold for the specimen grating: (a) expose photographic plate; (b) develop; (c) dry; and (d) add reflective coating. (From D. Post, Moiré interferometry, in *Handbook on Experimental Mechanics,* edited by A.S. Kobayashi, first edition, published for the Society for Experimental Mechanics, Inc., Englewood Cliffs, NJ: Prentice–Hall; 1987 [10]. Used with permission of Prentice–Hall.)

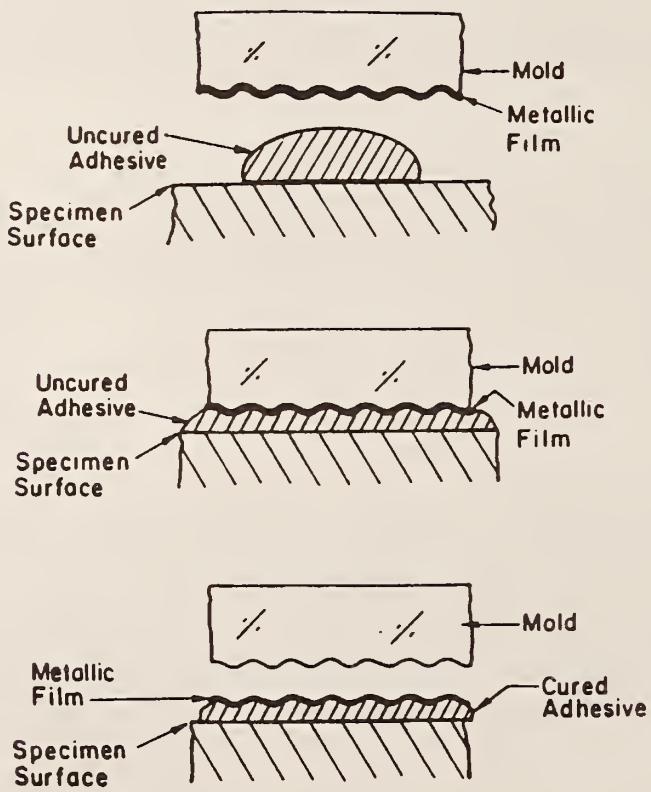

Figure 7. Process for casting the specimen grating whereby the reflective metal film is transferred to the specimen grating. (From D. Post, Moiré interferometry, in *Handbook on Experimental Mechanics,* edited by A.S. Kobayashi, first edition, published for the Society for Experimental Mechanics, Inc., Englewood Cliffs, NJ: Prentice–Hall; 1987 [10]. Used with permission of Prentice–Hall.)

A new method introduced by Han and Post [11] yields improved resolution for moiré interferometry. The wavelength of the laser light is reduced by capitalizing on the index of refraction of the light as it passes through a refractive medium. This improves the resolution to ~200 nm per fringe order.

2.4 Electron-Beam Moiré

Electron-beam moiré is a recently developed technique first described by Robinson in 1981 [12] and Kishimoto et al. in 1991 [13]. The technique has been refined and fostered by Dally and Read [14], and its use is described in references 15 through 18.

Using many of the principles of video moiré [18], e-beam moiré is an advancement in resolution because it is conducted in the scanning electron microscope (SEM). It is based on the fundamentals of optical moiré while exploiting the spatial resolution of the SEM. The limitations of the wavelength of light are circumvented by imaging with an electron beam. As with moiré interferometry, e-beam moiré does not require a separate, tangible reference grating. The reference grating is an integral part of the SEM—the rastering of the electron beam—and exists whenever the current in the filament is sufficient to produce an image. The electron beam rasters across the field of view at regular intervals: 480 raster scans per image for a typical imaging system. The pitch of the "reference grating," therefore, depends on the magnification and the viewing area of the system.

The specimen grating is a series of ridges and trenches generated by e-beam lithography in the SEM with the aid of a computer program that controls the location and dwell time of the electron beam. Figure 8 shows the procedure used to make the specimen grating. The polished surface of the specimen is coated with a conductive material; then a thin coat of radiation-sensitive resist is spun on, and the specimen is baked to drive off volatiles from the resist. An electron beam exposes the resist in the desired pattern, which is developed by dissolving the exposed areas in a solution of alcohol and solvent. Table 1 shows the various grating sizes and pitches that have been obtained with this lithography system.

The magnification for the lithography is nominally the same as for the imaging. The number of lines written is 1 or 2 times the number of rasters of the electron beam so that the initial correlation is approximately 1 to 1 (or 1 to 2). Because the SEM is focussed and tuned by using electromagnetic lenses to adjust for differences in focal distance, it is virtually impossible to replicate tuning conditions between sessions on the SEM. An additional complication is that the SEM used in this study is not capable of continuous magnifications; that is, the only possible magnifications are those preset by the manufacturer. A null field, one for which an exact 1-to-1 correlation exists between the specimen and reference gratings, is very rare.

When the pitch of the specimen grating differs slightly from that of the reference grating, moiré fringes are present for the initial condition. In e-beam moiré, light and dark fringes are not the result of light passing through a grating, but rather the result of the electron beam interacting with the corners of the ridges (light fringes) or being absorbed by the trenches (dark fringes).

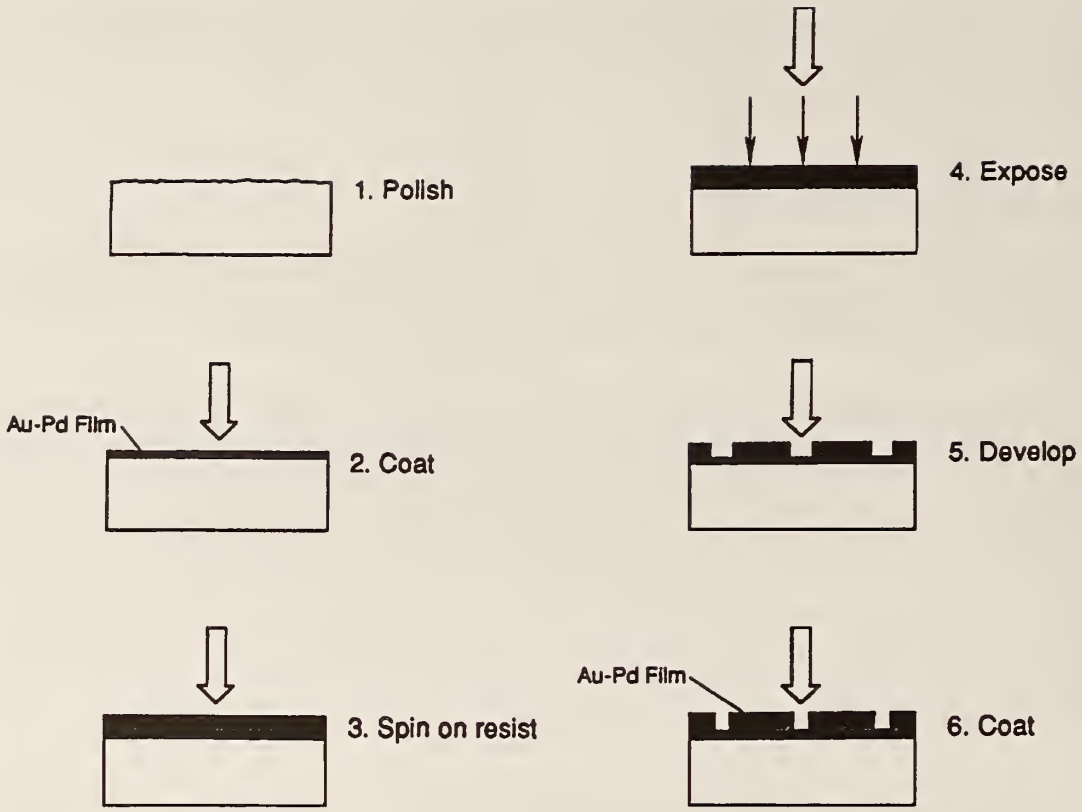

Figure 8. The processing steps in making the specimen grating for e-beam moiré.

Table 1. Sizes and pitches of patterns produced.

Pattern width, μm	Line pitch, nm	Magnification
1000	900	100×
500	900	200×
	450*	
200	350*	500×
	175	
100	175	1000×
50	90	2000×

*Discussed here.

A change in the moiré fringe density is the physical result of the presence of deformation in the region of the grating. Expansion in the specimen can either increase or decrease the density of fringes, depending on the initial condition. If, in the initial condition, the pitch of the specimen grating is larger than that of the reference grating, expansion will lead to more fringes. If, however, the pitch of specimen grating is smaller than that of the reference grating, expansion will move the pitch size closer to a 1-to-1 correspondence and, therefore, fewer fringes. Figure 9 demonstrates this concept. The origin of the x-axis is defined as the null condition; fringes to the right of the origin are fringes of expansion, (+)N; and fringes to the left are fringes of contraction, (–)N. If the initial condition is to the left of the origin and the specimen is expanded, the number of fringes will decrease until the null condition is achieved, after which the number of fringes will again increase. If the specimen is contracted, the number of fringes of contraction will increase. The reverse is true if the initial condition is to the right of the origin. Expansion will result in an increased number of fringes of expansion, and contraction will lead to fewer fringes until the null condition results, followed by an increasing number of fringes of contraction.

Figure 2 shows that for every line from the specimen grating that moves out of the field of view, one moiré fringe appears. From the pitch of the "reference grating" and the initial fringe density, strain either across the entire grating or at a local feature can be calculated.

The resolution of the technique ranges from 90 to 900 nm per fringe order. Calculating values for strain depends on the pitch of the specimen grating and the ability to perceive fractions of fringes. Discernment of fractions of fringes depends on the total number of fringes in the field of view and the fringe contrast. If only 4 fringes are present, it would be easy to

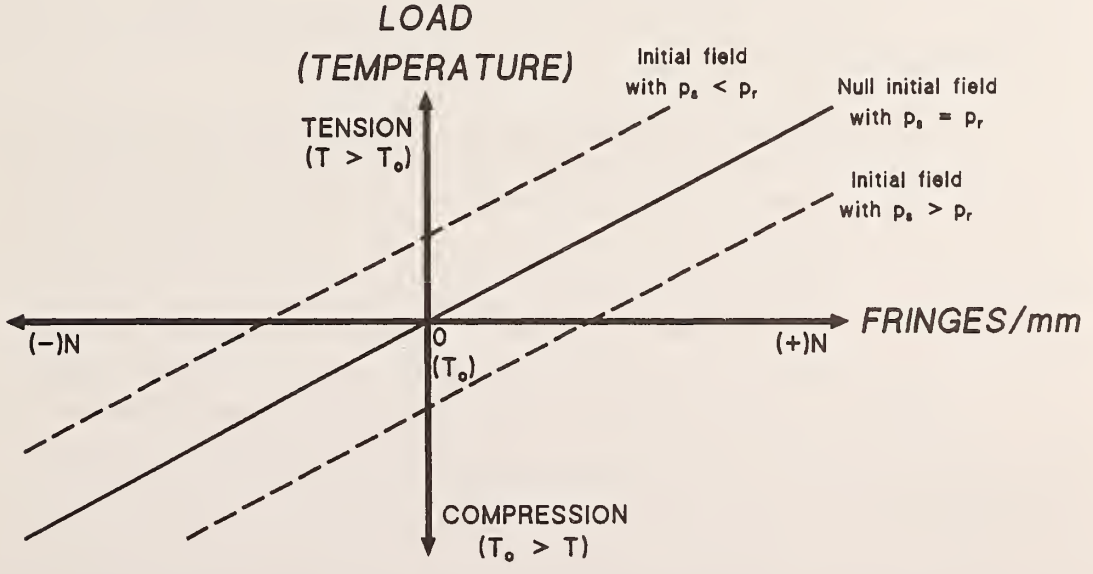

Figure 9. Diagram of the relationship between positive and negative fringes and the relative pitch of the specimen and reference gratings in the initial fringe field. Fringes along (+)N are fringes of expansion and fringes along (–)N are fringes of contraction.

detect, say, 1/10 or even 1/20 of a fringe with good contrast. However, if 25 fringes are in the field of view, perhaps only 1/4 of a fringe would be discernable. Therefore, the resolution of the technique falls in a band ranging from 225 to 9 nm.

There are significant limitations to this technique as it was conducted in this study. Displacements are available only from the in-plane surface of the specimen. A single e-beam moiré image cannot provide any quantitative information; the technique relies on the changes observed in the fringe field from an initial condition. Another disadvantage is the inability to assign a precise fringe order to the moiré fringes observed. Because the pattern covers a limited area and not a region extending to a free surface, fringe orders must be assigned arbitrarily. Thus, absolute displacements are not usually quantifiable, but strains are.

3. New Developments in Electron-Beam Moiré

3.1 Issues and Problems

The basic technique for writing lines and performing experiments with e-beam moiré is essentially unchanged since Dally and Read first published their work in 1993 [14]. However, to advance the experimental technique, the following issues were investigated: grating-line quality, grating-line density, crossed-line gratings, rotation control, heating and cooling stage, and benchmarking.

Occasionally, grating lines such as those made by the method described in reference 14 have either degraded over time or have deteriorated while being thermally loaded. In certain cases, the temperature at which the specimen was exposed may have been under question. In other circumstances, the polymethylmethacrylate (PMMA), of which the lines are made, did not adhere rigorously enough to withstand thermal cycling. Study of the behavior of materials in electronic packaging exposed to thermal fatigue is impossible until lines can be made to withstand thermal cycling.

In the standard pattern, 511 lines are written from bottom to top, which translates to a pitch range of 900 nm at 200× to 90 nm at 2000×. To improve the resolution of patterns covering a larger area, the density of the lines was increased. At 200×, lines with pitches of 450 and 225 nm have been written successfully. At 500×, the pitch of the lines has been halved to 175 nm. Efforts are always being applied toward improving the resolution of the technique.

One of the weaknesses of the original e-beam moiré technique was that the displacement data were available from only one direction. By locating the grating at interfaces and orienting it to maximize displacements in the primary direction, reasonable estimates of strain were obtained. However, both in-plane displacement components u and v are needed to obtain accurate values of shear strain.

Crossed-line gratings to measure displacements in two directions solve one problem and introduce another. The new problem is how to separate fringes due to rigid body-rotation from those due to shear. The rotation of the electron beam in an SEM is typically controlled by a knob on the scan-rotation unit. Control is coarse with respect to the sensitivity to rotation of the fringes, particularly fringes of division. The only way to eliminate fringes of rotation is to

replicate the angle of rotation within 20" when rotating to view the *u*-field to *v*-field images. This is not possible with standard equipment, so modifications were made to the scan-rotation unit of the SEM.

For evaluating electronic components, MIL-STD-883 calls for subambient thermal exposures. The stage used could only heat, not cool, the specimen. In addition, grounding problems caused the observed fringe field to drift. The stage was designed with the thermocouple adjacent to the heater rather than at the surface of the stage where the specimen would be located. All these problems were eliminated with the purchase of a new stage that produces a temperature range of –196 °C to +400 °C.

To attain confidence in the values of thermal deformation measured with e-beam moiré, it was necessary to benchmark the technique against a known material. Pure copper (99.999 percent) was chosen to determine the coefficient of thermal expansion, the repeatablity of the measurement, and the behavior of the SEM.

Each of the issues identified above will now be addressed.

3.2 Processing Improvements for Grating Fabrication

Upon looking for a solution to making lines that can withstand the rigors of thermal cycling, some of the techniques already used in microcircuitry were explored. A possible solution may be to etch the lines into the surface of the specimen. The PMMA is used as a mask, as it is used in the electronics industry when making microcircuits. The cross-sectional profile of the grating resembles a square wave, as it does after lithography:

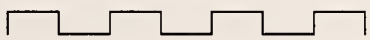

All materials ideally etch at the same rate, so that the material from the bottom of the trenches is removed at the same rate as the PMMA. When the last of the PMMA is etched away, the depth of the grooves cut into the surface of the specimen should equal to the original thickness of the PMMA (~150 nm). All the PMMA should be removed and the lines themselves should be an integral part of the specimen. During thermal loading, the lines should be as durable as the specimen material.

Several attempts to make moiré gratings with an ion-beam etch yielded inconsistent results. The ion-deposition system used to put a conductive coating on specimens for the SEM also has an etch mode. The current is reversed so that the argon plasma removes material from the stage, and anything on the stage, and deposits the material on the source ring.

The first attempt on a plated through-hole packaging specimen and a homogeneous copper specimen gave moderately acceptable results after a total etching time of 120 min for the copper specimen. All the PMMA was gone from patterns with a 900 nm pitch. Faint grooves were cut into the copper. For patterns with smaller pitches, the PMMA remained on the ridges of the lines. Efforts to remove the remaining PMMA with acetone were not successful. However, the lines appeared to be more durable: they showed no signs of breaking up as they were repeatedly viewed and thermally loaded in the SEM.

The second attempt at etching a copper specimen resulted in the removal of all the PMMA, leaving very faint lines etched into the surface of the copper after only 5 min of etching. The notable differences were that the first copper specimen was potted and placed near the center of the stage for etching, and the second copper specimen was unpotted and placed toward the edge of the stage. To compare etching rates, a potted specimen and an unpotted specimen were placed simultaneously in the ion-deposition system in the etch mode; no difference in etching rates was found.

A third attempt to etch a copper specimen, also unpotted, was made. After a 5 min etch, all the PMMA was gone and no patterns were visible optically, but in the SEM all the patterns produced moiré beautifully. The etch was probably too shallow to be optically discernable from the texture of the copper surface, but the regularity allowed the formation of moiré fringes. Lines were also etched on a copper/CA specimen. After 3.5 min of etching, everything was removed from the copper, but some PMMA remained on the CA. Those areas of the CA showed moiré well, but no moiré existed on the copper: etching did not attack the copper.

The inconsistent results point to the etching equipment itself. An ion-beam etching system, designed specifically for etching, would produce more dependable results.

Another possibility for making reliable lines is the lift-off process used in the electronics industry. This technique requires that, after lithography, the bottom of the trench be a teardrop shape rather than square. To achieve the desired shape, the resist is layered so that the bottom layer is more reactive to the electron beam than the top. Once the profile is attained, a metal layer is vapor-deposited on the surface to fill in the trenches. The last step is to remove the resist layer so that all that remains are the metal strips forming the grating. Metal will tolerate the thermal cycling far better than the resist.

A member of the staff at the National Nanofabrication Facility [19] suggested that the desired profile could be achieved by using two different resists, one (for the bottom layer) with a lower molecular weight of PMMA in chlorobenzene, the other (for the top layer) with a higher molecular weight in methyl isobutyl ketone, a solvent that would not attack the sub-layer of PMMA. The electron beam would have a larger interactive region with the lower molecular-weight resist resulting in the teardrop shape. This method for improving the durability of the lines in the specimen grating has not, as yet, been tried,

3.3 Crossed-Line Gratings and Rotational Control

How can shear strains be measured when displacement values are available for only one orientation? The obvious solution is to obtain information from two orthogonal directions. When only isotropic, homogeneous materials in a uniform stress field are considered, two separate gratings oriented 90° from each other suffice. However, the materials studied are neither isotropic nor homogeneous, and the fields are not uniform. The displacement data, therefore, must be obtained from the same location. To accomplish this, crossed-line gratings have been successfully written on copper and copper/CA sandwich specimens. The minimum pitch obtained was 175 nm, which is larger than the 90 nm pitch that can be obtained for a line grating. Contributing to this loss in resolution are the interaction volume and the dose required for adequate exposure. The PMMA is exposed not just where the electron beam touches, but in the area from which electrons are scattered. Because the surface is subjected

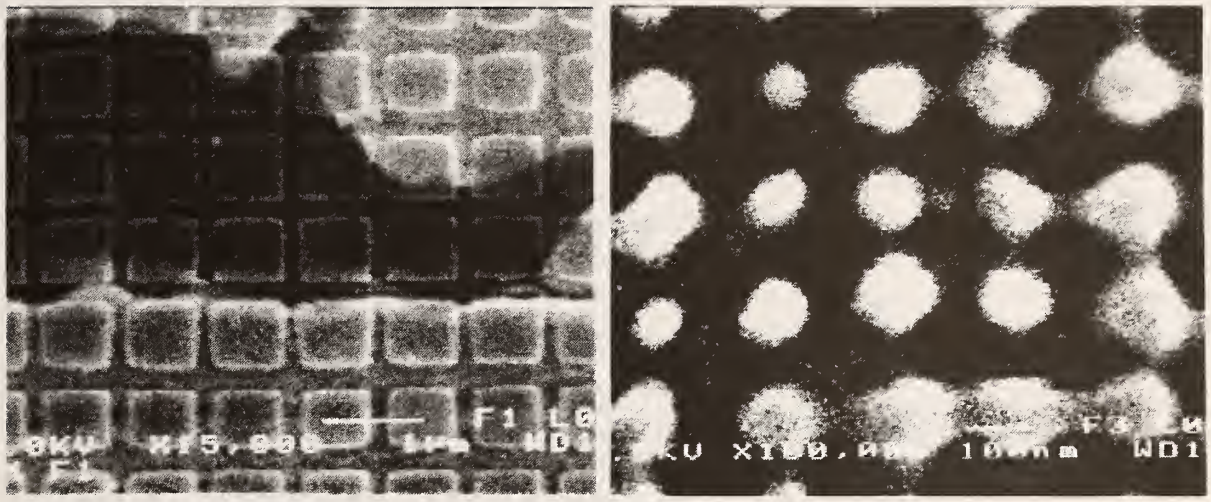

Figure 10. Crossed-line gratings on a copper/CA specimen with pitches of (a) 900 nm (b) 175 nm.

to the electron beam twice, once at 0° and again at 90°, more area is exposed and, therefore, more PMMA removed. Lowering the dose used can reduce the exposure area, but a minimum dose is required to cut through the PMMA to form the grating. Figure 10 shows orthogonal lines on copper/CA specimens with a pitches of 900 and 175 nm. The crossed-line grating with the larger pitch looks like window panes, whereas the material that remains in the grating with the smaller pitch is a regular array of dots. The quality of the moiré from both pitches is excellent in both orientations.

To be used properly, these crossed-line gratings must be repeatably and precisely aligned to the scan of the electron beam in each orientation. As mentioned above, the standard scan-rotation unit of the SEM used in this study is not able to accomplish this. Therefore, the scan-rotation unit was modified to use the sine and cosine of the rotation potentiometer at 0 and 90° to switch between the two angles. A control box was fabricated external to the scan rotation unit; it has a switch that enables toggling between 0 and 90° to write the lines and to view the moiré. This means that the angle of rotation used to write the lines will be the same as that necessary to view the moiré. This modification apparently has solved the rotation problem and enabled shear strains to be measured with confidence.

3.4 Parametric Studies and Error Analysis

A parametric study was undertaken to determine which factors may influence a measurement made with e-beam moiré at "fixed" settings on the SEM, Initial measurements indicated that the fringe pattern changed although the specimen was not subjected to temperature changes or to mechanical loading. Once a specimen grating has been prepared, the pitch of the grating lines on the specimen will not change unless the specimen is thermally or mechanically deformed. Therefore, the pitch of the reference grating must be varying.

Before studying possible error sources with e-beam moiré, identifying the key parameters in formation of the reference grating is instructive. As described in references 14 and 16, the pitch of the reference grating for e-beam moiré can be calculated as

$$p_r = \frac{S}{MR}, \tag{15}$$

where S is the nominal image width, M is the magnification of the SEM, and R is the number of raster scan lines. The nominal image width and the number of raster scan lines are fixed for a given SEM during a given experiment. Therefore, according to eq (15), only a change in magnification over time can contribute to an apparent change in the pitch of the reference grating. Any drift in the instrument (such as working distance, accelerating voltage, electronic magnification control, or other instrument-related issues) can produce an apparent drift in the magnification. The goal was to study the influence of these apparent magnification drifts and not to isolate their precise cause for a given test on a particular instrument. All these sources will be treated as an apparent change in magnification. Note that small changes in the magnification can contribute strongly to the apparent pitch of the reference grating since they are inversely proportional. Read and Dally [16] noted that the value of M must be precisely known for proper interpretation of the moiré fringe fields. They further noted that the apparent magnification from the SEM character display differed from actual measured magnifications by approximately 5 percent for the SEM used in their investigations. No time variation of M was considered.

If some variation occurs in the magnification of the SEM, the pitch of the reference grating can be written as

$$p_r = \frac{S}{(M+\Delta M)R}, \tag{16}$$

where ΔM is the variation in the magnification [20]. The frequency of a moiré fringe field f_f under the assumptions of small rotations and fine pitches is [8]

$$f_f = \frac{p_r - p_s}{p_r p_s}. \tag{17}$$

When the reference grating pitch varies according to eq (16), eq (17) can be rewritten in terms of frequencies,

$$f_f = f_s - \bar{f}_r - \frac{R\Delta M}{S}, \tag{18}$$

where f_s is the frequency of the specimen grating and $\bar{f}_r$ is the ideal reference grating frequency. Further, eq (18) can be written as

$$f_f = \bar{f}_f - f_{\Delta M}, \tag{19}$$

where $\bar{f}_f$ is the frequency of the moiré fringes with no variation in the magnification, and $f_{\Delta M}$ is the additional fringe field due to the variation in magnification,

$$\bar{f}_f = f_s - \bar{f}_r \,, \tag{20}$$

$$f_{\Delta M} = \frac{R\Delta M}{S} \,. \tag{21}$$

Typical values for the nominal image size and number of raster scan lines for the SEM used in this study are S = 89 mm and R = 480 lines. Figure 11 shows the error term $f_{\Delta M}$ as a function of the variation in magnification ΔM for the SEM used here.

As an example of the error, consider a specimen grating with pitch p_s = 180 nm observed in the SEM at a nominal magnification of 1100×. This is essentially the near-match condition for this specimen grating pitch in the SEM used. From eq (15), the nominal reference grating pitch obtained is p_r = 168.6 nm. The spatial frequency of the moiré fringes from eq (20) is then 0.38 μm^{-1}. By assuming the magnification variation is ±0.20× at 1100×, the additional fringe field occurs at a spatial frequency of $f_{\Delta M}$ = 1.1 mm^{-1}. At M = 1100×, a region 81.8 μm across is observed in the microscope. The total number of moiré fringes observed for this example is then 30.7 ±0.09 fringes, which represents a 0.28 percent variation in the fringe field.

In the case of uniform axial strain on a specimen, the error in the strain measurement due to the magnification variation can be calculated. Assuming a null condition, Reed and Dally [16] calculated the tensile strain in terms of frequencies as

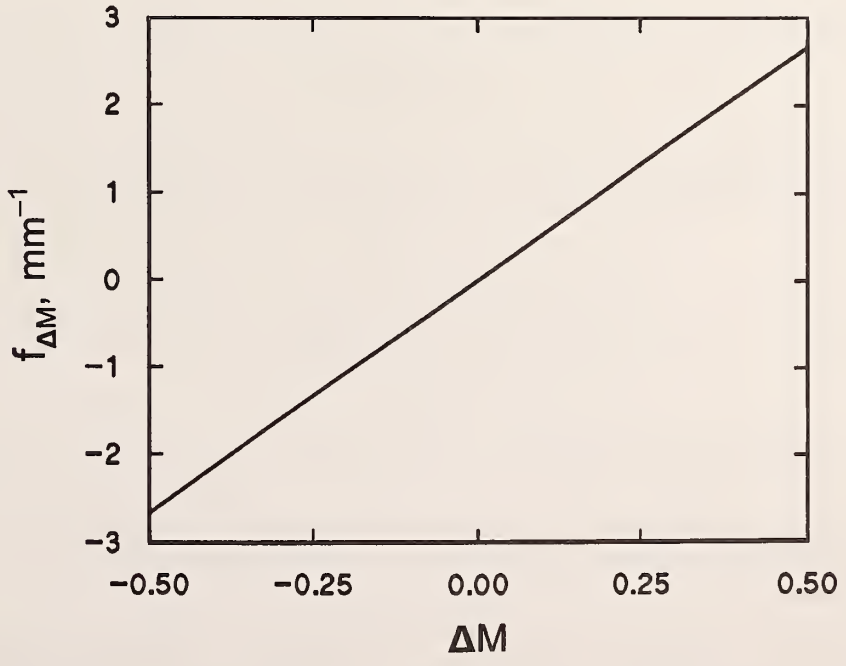

Figure 11. The error term $\bar{f}_{\Delta M}$ as a function of the variation in magnification ΔM for the SEM used in this study.

$$\varepsilon = -\frac{f_f}{f_f + f_r}. \tag{22}$$

Including a variation in magnification that affects both f_f and f_r, eq (22) rewritten in terms of grating pitches is

$$\varepsilon = \frac{p_s M R}{S} - 1 + \frac{p_s R \Delta M}{S}, \tag{23}$$

where the last term represents the error term. It is helpful to consider the total strain as an apparent strain,

$$\varepsilon_{app} = \varepsilon_{true} + \varepsilon_{\Delta M}, \tag{24}$$

where

$$\varepsilon_{true} = \frac{p_s R M}{S} - 1 , \tag{25}$$

and

$$\varepsilon_{\Delta M} = \frac{p_s R \Delta M}{S}. \tag{26}$$

For this analysis, eq (26) can be simplified by assuming small strains,

$$\frac{p_s R}{S} \approx \frac{1}{M}. \tag{27}$$

Equation (26) can then be written as

$$\varepsilon_{\Delta M} \approx \frac{\Delta M}{M}. \tag{28}$$

In the specific example used above (p_r = 168.6 nm), assume a uniform strain of 1200×10^{-6}. From eq (22), by assuming no change in the magnification, the specimen grating has a pitch of p_s = 168.8 nm. For this particular example, figure 12 shows the error term $\varepsilon_{\Delta M}$ as the magnification is varied; the error is significant. At a value of $\Delta M = 0.20\times$ (with a nominal magnification of 1100×), the additional strain is 182×10^{-6}. The error in the strain measurement is then 15 percent. To maintain less than 5 percent error in the strain measurement would require control of the magnification such that $\Delta M < 0.07\times$.

The analysis highlights the necessity of strict control of the magnification for quantitative measurements with e-beam moiré. As noted in reference 16, the nominal magnification must be accurately known for proper interpretation of the moiré field. Clearly, not only must the nominal magnification be known, but the factors influencing the magnification must be exceptionally stable.

A series of experiments were performed to identify and quantify factors that vary with time in a typical e-beam moiré experiment. For each of the experiments, a single, homogeneous, polycrystalline, 99.999-percent-pure copper specimen was used. The disk-shape specimen, with a diameter of 5 mm and a thickness of 2 mm, was instrumented with a line

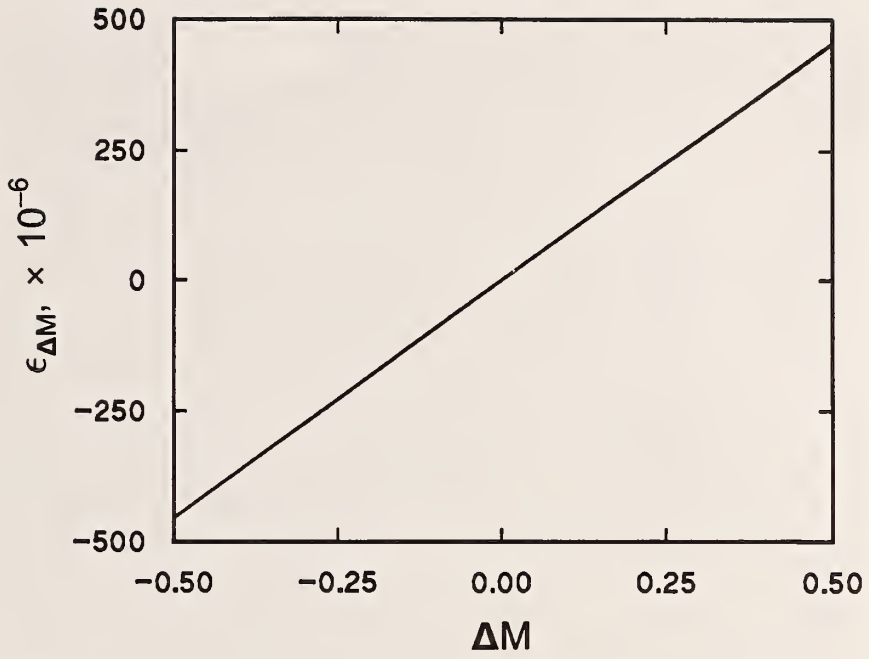

Figure 12. The error term $\varepsilon_{\Delta M}$ as a function of the variation in magnification ΔM for the SEM used in this study.

grating located near the center of the specimen with p_s = 180 nm. The specimen grating was etched into the surface of the copper with an argon sputter etch. The specimen was placed into the SEM, and four separate tests were performed at a magnification of 1100×. This magnification is associated with the near-null field for the specimen grating frequency used in this experiment. The temperature of the testing stage was monitored during the acquisition of images. In the two tests in which the temperature was recorded, the maximum temperature variation observed in the SEM chamber was ±0.6 °C.

In one test, for example, moiré fringe fields were obtained at fixed settings on the SEM over a period of 240 min at 30 min intervals. A typical fringe field is shown in figure 13. The initial fringe field is not an ideal null pattern since the magnification on the SEM is available only in discrete increments. The number of fringes in the initial field may vary for a given specimen grating owing to slight changes in either the working distance or the focus as the SEM is set up for a particular experiment. For the T test analyzed here, the initial field contained approximately four fringes.

Each acquired image was analyzed to obtain the average number of moiré fringes across the image. The analysis was based on a fringe-analysis program developed at NIST. The program requires the user to specify points located along a fringe center. The software then performs a spline fit to the data.

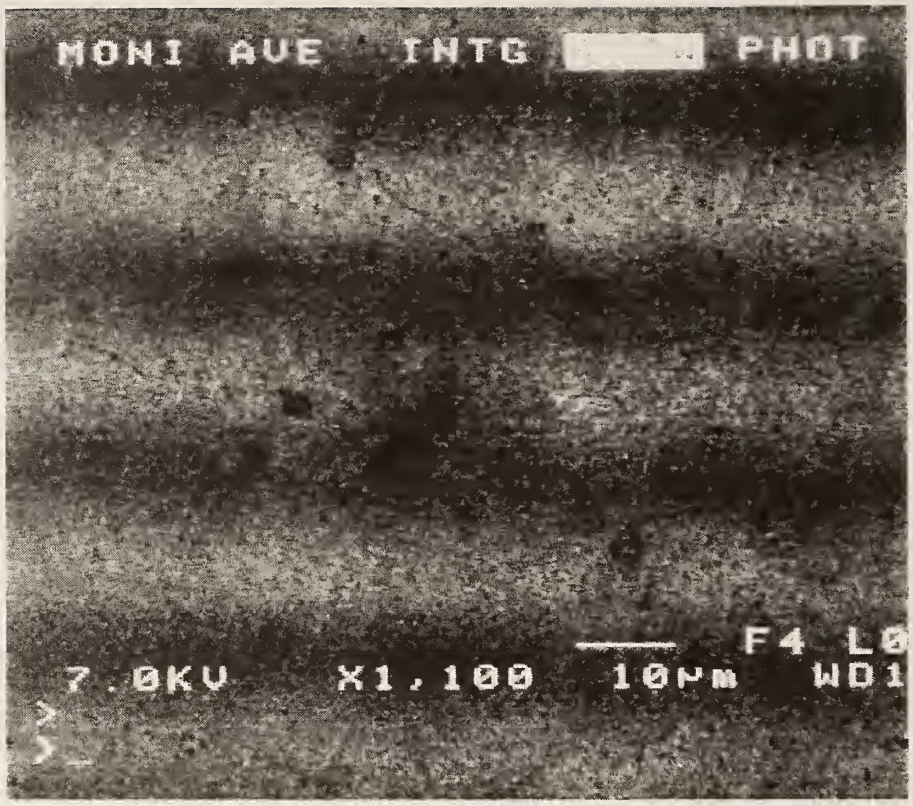

Figure 13. Typical moiré fringe field at 1100× obtained under ambient conditions.

As shown in figure 14, a clear variation in the average number of fringes occurs over time. In all the experiments conducted, the first data point typically showed the greatest variation from the mean value. For the data shown in the figure, the mean value was 4.34 fringes with a standard deviation of 0.14 fringes. The field of observation at 1100× is 80.9 µm, which yields a mean moiré fringe frequency of 0.0536 μm^{-1} with a standard deviation of 0.0017 μm^{-1}. When this variation in the fringe field is assumed to be due strictly to factors influencing the magnification of the SEM, the apparent change in the magnification required to produce one standard deviation can be calculated from eq (21). From eqs (15) and (17), the nominal magnification required to produce the observed moiré field frequency is 1050×. The magnification was set on the SEM at 1100×. (The calculated value is within the usual 5 percent uncertainty allowed in the magnification calibration.) To produce one standard deviation in the fringe field, a value of $\Delta M = 0.32\times$ for the data shown in figure 14 is obtained from eq (21).

When only the data points obtained after 30 min had elapsed are considered, a mean value of 4.30 fringes is obtained with a standard deviation of 0.07. The mean value is comparable to that obtained previously with all data points. Therefore, the nominal magnification is approximately the same ($M = 1050\times$). From eq (21), a value of $\Delta M = 0.16$ required to produce one standard deviation in the fringe field is calculated.

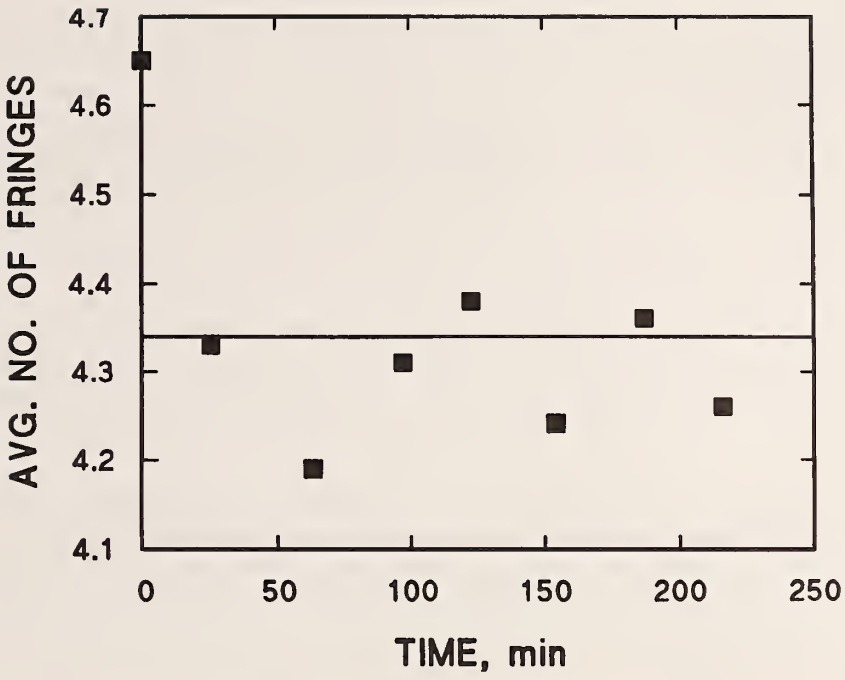

Figure 14. Average number of fringes for the copper specimen as a function of time.

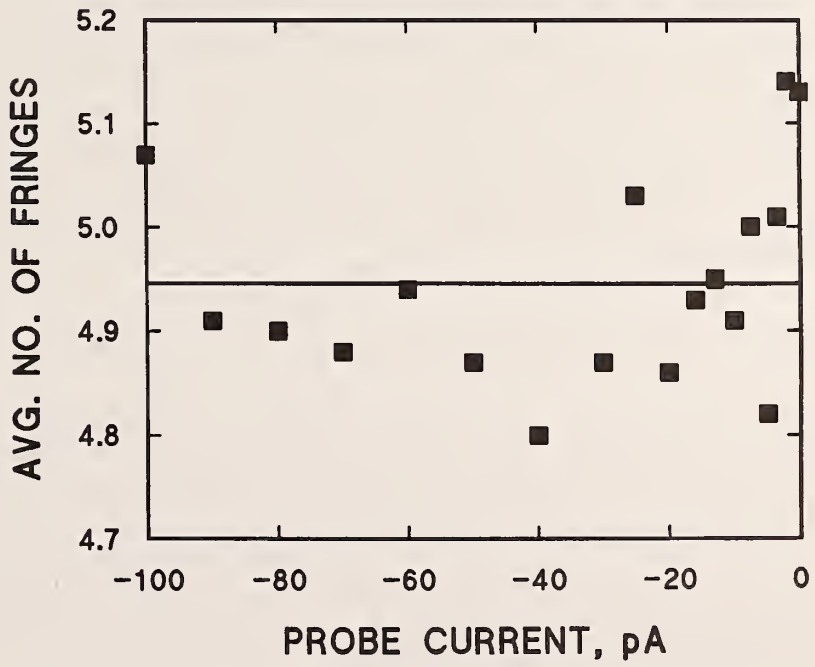

Figure 15. Average number of fringes as the probe current is varied.

The probe current in the SEM was initially suspected of producing the apparent variations in the fringe field. This suspicion was based on recordings of probe current over time as each experiment was performed. To investigate the likelihood of the probe current causing variations in the fringe field, two tests were performed in which the probe current was varied and images were acquired. The average number of fringes plotted as a function of probe current for one test is shown in figure 15. For this data set, the mean number of fringes is 4.95 with a standard deviation of 0.10. Comparing figure 15 with figure 14 shows that the variations observed over time are approximately the same as the variation observed over the time the probe current was varied. Figure 15 shows that the probe current was varied from approximately 0 pA to –100 pA. The observed variation in probe current during tests similar to that which provided the data in figure 14 was only ±0.6 pA. The probe current clearly was not responsible for the observed temporal variation in the fringe field. This is not unexpected, because the probe current should not vary the magnification in a typical SEM.

During operation of an SEM, charge may accumulate on the electromagnetic lenses, which could lead to small variations in magnification. To investigate this possibility, the electromagnetic lens system was degaussed before each image of a series of images was acquired. The average number of fringes as a function of time is shown in figure 16. Again, a variation in the number of fringes over time is observed with a standard deviation of 0.09 fringe. This is comparable to the variation observed in figure 14 where the lens system was not degaussed before acquiring the images. Degaussing of the lens system does not appear to improve the observed variation of the fringe field with time.

Finally, human factors were considered by studying the variation in the average number of fringes due to the fringe-tracing procedure. An image was acquired and six independent tracings were performed of the fringe centers with the fringe-analysis software used in this study. Of concern here was variation in the location of the center of the fringes and the effect of the number of points along each fringe center used in the spline fit to the data. The results are shown in figure 17 for the average number of fringes across the entire image for each tracing. As shown in the figure, a variation of approximately ±0.05 fringes occurred with a standard deviation of 0.02 fringes. This result is far below the observed variation over time shown in figure 14. Fringe tracing, therefore, could not be responsible for the observed variation in the fringe field.

3.5 Benchmark: Coefficient of Thermal Expansion for Copper

To provide a benchmark for the e-beam moiré method in thermal-stress studies, a total of six experiments were performed to determine the coefficient of thermal expansion α of copper. The first two experiments used a copper specimen with a geometry identical to that of the specimen previously described but with a line-grating pitch of 900 nm. The remaining experiments were performed on the same specimen that was used for studying the temporal variation of the fringe field. Both specimens had line gratings that were etched into the surface of the specimen to avoid high-temperature deterioration of the PMMA coating, which is normally used for producing gratings with e-beam lithography.

The procedures for all experiments were similar. For the more recent tests, the specimen was placed in the vacuum chamber of the SEM and thermally cycled twice between –50 °C and +150 °C. The temperature was then set at the starting temperature for the test (–50 °C).

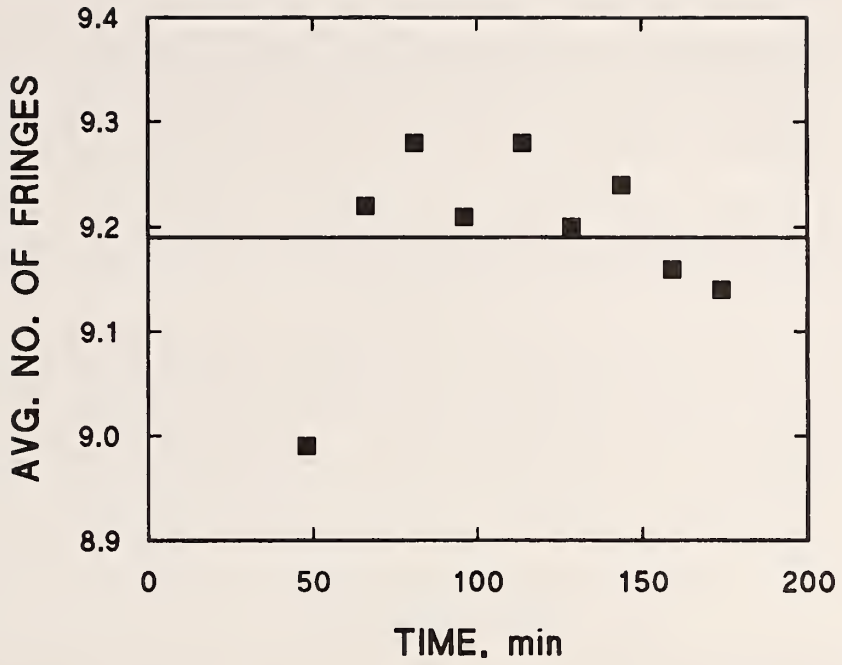

Figure 16. Average number of fringes as a function of time. The lens was degaussed before acquiring each image.

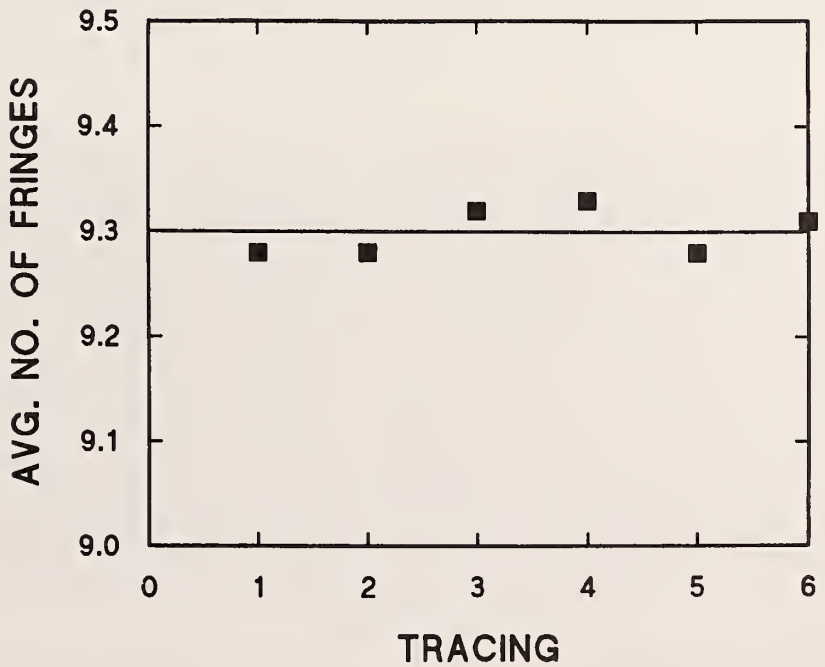

Figure 17. Average number of fringes determined from computer tracings of the fringe patterns.

Images of the moiré field were acquired at intervals of approximately 50 °C. After each increment in temperature, the specimen was allowed to equilibrate before acquisition of the moiré field image. Equilibrium was defined as that time when the observed lines moved less than 0.25 lines in 1 min across the field of view. This required waiting a maximum of 30 min. Typical fringe fields at temperatures of –49.6 °C and 150.6 °C are shown in figure 18.

For two of the tests, the average number of fringes across the field as a function of temperature is plotted in figures 19 and 20. Figure 20 shows the mean values of the data at each temperature; the bars indicate the spread in the data.

The coefficient of thermal expansion was calculated from the fringe field following the procedure given reference 21. Only the change of fringe order with temperature is of interest over the uniform displacement field, so the slope s_f of the average number of fringes with respect to temperature was calculated. Then the coefficient of thermal expansion can be directly calculated as

$$\alpha = \frac{s_f}{R}. \tag{29}$$

From eq (29), α is estimated by dividing the slope of a best-fit line through the data (see the examples in figs. 19 and 20) by R (R = 480 for the SEM used). Table 2 summarizes the results of four tests obtained by using this calculation.

The average coefficient of thermal expansion from the moiré data can be compared with a handbook value of $\alpha = 16.5 \times 10^{-6}$ °C^{-1} for pure copper [22]. The average result is within 1.8 percent of the handbook value. However, the results must be evaluated in light of the parametric studies performed on the apparent magnification drift.

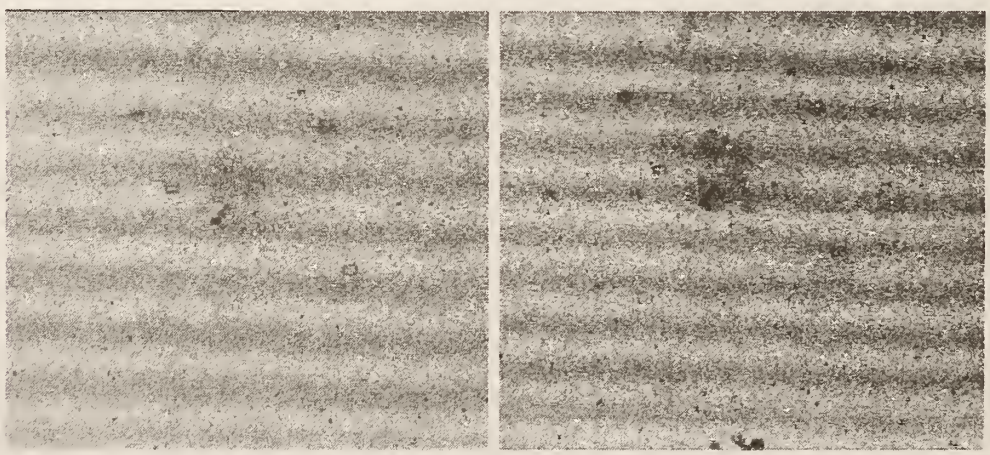

(a) (b)

Figure 18. Typical e-beam moiré fields at 1100× acquired at temperatures of (a) –49.6 °C and (b) 150.6 °C.

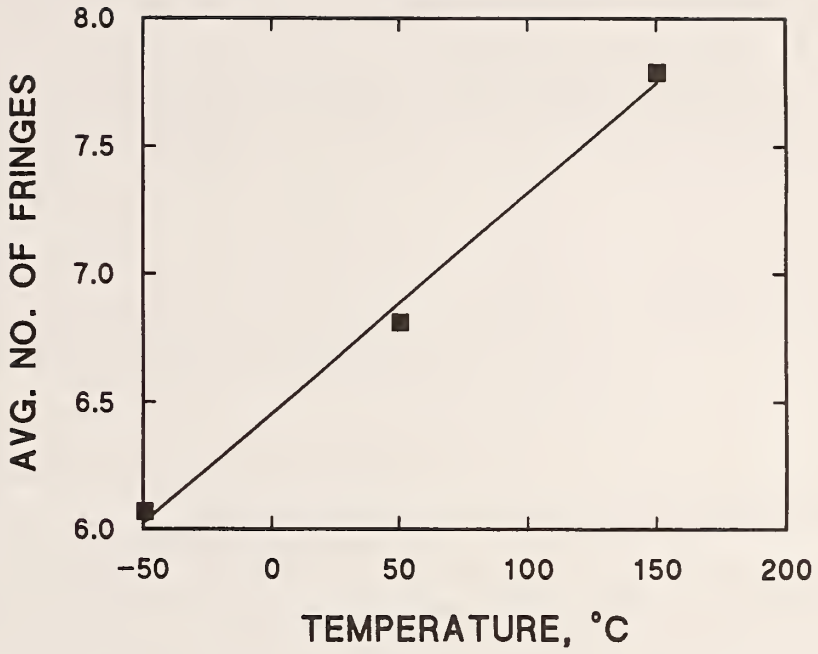

Figure 19. Test no. 1 for the average number of fringes as a function of temperature for the copper specimen.

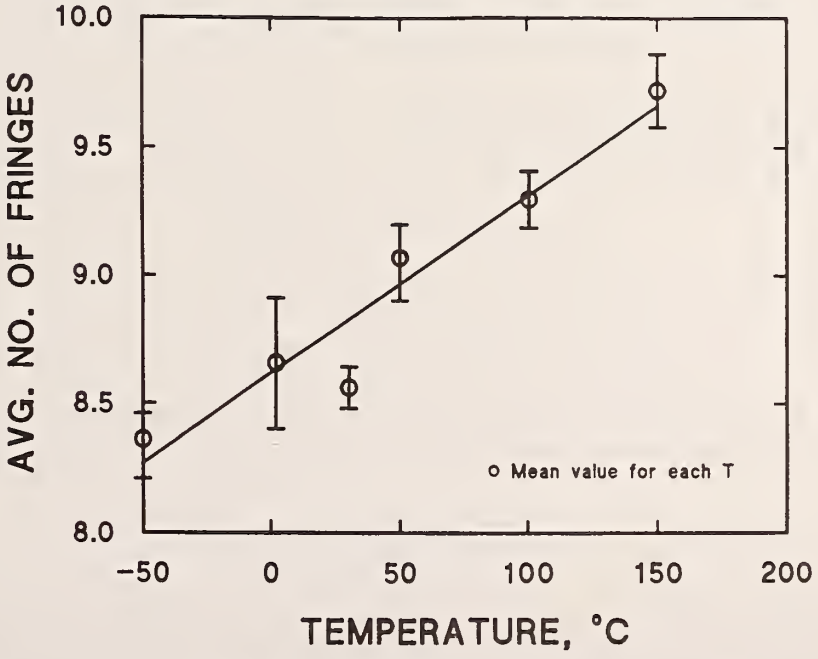

Figure 20. Test no. 4 for the average number of fringes as a function of temperature for the copper specimen. Shown are the mean values obtained at each temperature increment. The error bars indicate the variation in the data.

Table 2. E-beam moiré results on the coefficient of thermal expansion α of copper.

Test	Magnification	Slope, s_f	α, °C^{-1}
1	220×	8.61×10^{-3}	17.9×10^{-6}
2	220×	1.03×10^{-2}	21.4×10^{-6}
3	1100×	6.42×10^{-3}	13.4×10^{-6}
4	1100×	14.5×10^{-3}	14.5×10^{-6}
		Average α =	16.8×10^{-6}

3.6 Uncertainty of the Coefficient of Thermal Expansion

Consider a variation in apparent magnification during a thermal expansion test. The apparent coefficient of thermal expansion can be calculated from the apparent strain as

$$\alpha_{app} = \frac{\Delta\varepsilon_{app}}{\Delta T}, \tag{30}$$

provided that the thermal strains are linear over the temperature increment ΔT. The apparent strains, as shown in eq (24), are [20]

$$\alpha_{app} = \frac{\Delta\varepsilon_{true}}{\Delta T} + \frac{\Delta\varepsilon_{app}}{\Delta T}. \tag{31}$$

This equation can be put in a more useful form:

$$\alpha_{app} = \alpha_{true}\left[1 + \frac{\Delta M}{\alpha_{true} M \Delta T}\right], \tag{32}$$

where

$$\alpha_{true} = \frac{\Delta\varepsilon_{true}}{\Delta T}. \tag{33}$$

On the basis of the data from the time-dependent variations of the fringe field, the apparent variation in magnification is approximately 0.32× at 1100×. From eq (32),

$$\frac{\alpha_{app}}{\alpha_{true}} = 1.088. \tag{34}$$

Therefore, an estimate of the coefficient of thermal expansion should be within ~9 percent. If the average values of the coefficient of thermal expansion from the four experiments discussed in table 2 are considered, $\alpha = 16.8 \pm 3.6 \times 10^{-6}$ °C^{-1} is obtained. This is clearly a larger error than would be expected from the time-dependent data. However, from the standard deviation of these tests, a more accurate estimation of the error becomes available. Multiplying α_{true} through, eq (32) becomes

$$\alpha_{app} = \alpha_{true} + \frac{\Delta M}{M \Delta T}. \tag{35}$$

The second term is the equivalent of the standard deviation, so equating that to 3.6×10^{-6} $°C^{-1}$ to calculate a value for $\Delta M/M$ over a temperature range of 200 °C yields

$$\frac{\Delta M}{M} = 7.2 \times 10^{-4}; \tag{36}$$

the value for a ΔM of 0.32 at 1100× is 2.9×10^{-4}. The value in eq (36) includes data obtained from two magnifications, 220× and 1100×, but this magnification variation can be considered to be characteristic of the SEM during the course of these tests.

4. Application to Conductive Adhesives

4.1 Overview of Conductive Adhesives

Conductive adhesives were first introduced in the 1940s. Early CAs were fundamentally the same as many of those used today. Until recently, CAs were used primarily for die attachment, that is, adhering a silicon chip to the lead frame. Virtually every CA was a silver-filled epoxy. As CAs are being proposed for a wider variety of functions, the chemistry and morphology are being changed to suit the application.

Polymer science enables many material properties to be tailored to the proposed use. It is possible to change the glass transition temperature T_g, the cure temperature T_c, elastic properties, and the coefficient of thermal expansion of a polymer. The matrix may be a thermoset polymer, a thermoplastic polymer, or a silicone. Additionally, the filler material is diverse and function-oriented. The shape of the particles may be spheres, random shapes, or flakes. The particles may be silver, nickel, metal- or carbon-coated glass, polymer spheres, or any of a variety of other materials. Silver is most often the choice because it has the highest conductivity at room temperature and it has a conducting oxide [23], unlike all other commonly used conductors.

Thermoset polymers, such as epoxies, are made up of one or two components, and they irreversibly cure in a chemical reaction with the introduction of heat or light. During curing the polymer chains cross-link to form a very hard, durable material that takes on a permanent shape. Thermoplastics, on the other hand, do not cross-link. They are stored in a solvent and, when employed, are heated to drive off the solvent or are melted for application. They can be remelted to replace components, much as solder, which is an advantage for applications in which reworking may be significant.

The two basic types of conductive adhesives are isotropic and anisotropic. Isotropic conductive adhesives (ICAs) are well-established: they have been used for decades. They have a polymer matrix with conducting particles randomly dispersed throughout. The particles (flakes or spheres) make up 25 to 35 volume percent or 70 to 90 mass percent of the polymer matrix [24–26]. The diameters of the particles range from 0.5 to 30 μm [26,27]. With this solid content, the particles contact each other, causing ICAs to be conductive in all directions (see fig. 21a). Isotropic CAs are used in die attachment and are proposed as a replacement for solder in surface-mount devices (SMDs) [25,28–53].

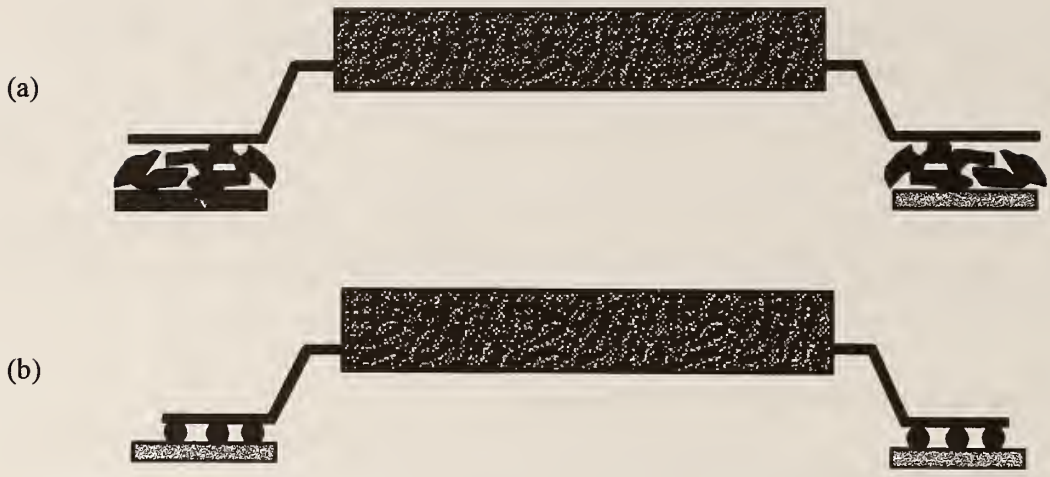

Figure 21. Schematic showing (a) an isotropic conductive adhesive and (b) an anisotropic conductive adhesive in a surface-mount application.

Anisotropic conductive adhesives (ACAs) were introduced to the electronics industry in the early 1990s. The volume fraction of conducting particles is much lower than that of ICAs, in the range 2 to 15 volume percent [54]. The particles do not contact each other; therefore, the conducting path is through each particle in contact with the lead and pad (see, for example, fig. 21b). Most ACAs are now being used to connect flex circuitry, but they are also being considered for some SMDs and direct chip interconnects [27,54–72].

Each of the two types of CAs is available in two forms: paste and film. The ICAs are more commonly found as pastes, and the ACAs are more commonly found as films. The paste is applied by screen printing, by stenciling, or with a syringe. The films are stored between release paper, and when applied, they are cut to the size needed. One side is attached to a prewarmed surface to get good adherence; then the other side is attached; and, finally, the adhesive is cured under pressure to ensure good contact.

The conventional uses for CAs, as with die attachment, are to connect materials that are not solderable, either because they cannot withstand soldering temperatures (for example, flex circuitry) or because they are not metallic (for example, glass in a chip-on-glass configuration). As industry broaches the formidable task of making a more environmentally compatible product to manufacture and dispose of, the toxicity of lead in solder becomes a primary issue. The electronics industry has proven its ingenuity by eliminating the use of chlorofluorocarbons before the year 2000 deadline set in the Montreal Protocol [37]. Now, efforts are being made to determine whether circuits can be made more efficiently and whether the use of hazardous substances can be reduced. Companies are researching the use of CAs to meet both objectives.

In recent years, Gilleo has suggested that it is an inefficient use of time and resources to make microcircuitry with subtractive (etching) techniques [61,73,74]. He intimates that etching is outmoded: "The concept is akin to writing messages by covering a sheet of paper with graphite and creating letters with an eraser" [73]. He further proposes that an additive process

using conductive polymers in place of copper be explored as an alternative. A citation search on the article showed that there was no published response by the electronics industry.

The electronics industry feels pressure to reduce the use of hazardous materials, as evidenced by the number of groups working on CAs as a solder replacement in leading electronics adhesive manufacturers in the United States and in Europe. The driving force appears to be coming from Europe. Germany is considering legislation that will make it the responsibility of the manufacturer to dispose of their products at the end of the product's lifetime [75]. The cost of disposing of hazardous materials gives great impetus to finding alternatives to traditional, toxic, manufacturing practices.

Besides the toxicity of lead, other motivations exist for replacing solder with CAs. The processing temperature for CAs is, on average, 70 °C lower than that for solder [23,47]. Many components and alternative circuits are heat sensitive, so reliability should improve with lower processing temperatures. As an added bonus, popcorning, the destructive escape of gas during processing, occurs at temperatures above 200 °C, 30 to 50 °C higher than the typical processing temperature for CAs. The particles in a CA are typically smaller (10 to 20 μm) than those in a solder paste (20 to 45 μm) [28], resulting in a finer pitch (0.3 mm) [76], about half that of solder, without the risk of bridging.

Like solders, ICAs can be stenciled and screen printed, so very little retooling would be necessary to replace solders with CAs. The differences on the assembly line would be the number of steps required and the amount of material dispensed. When attaching with CAs, the cleaning steps necessary with solder are not required. The volume of material needed when affixing a SMD is less with CAs than with solder. Solder paste comprises particles of solder in a dispensing liquid. This liquid is mainly solvents that evaporate, resulting in a 50 percent loss of volume during processing. Conductive adhesives lose almost no volume and, owing to their lower densities, use a much smaller mass of material to achieve the same volume. The density of a silver-filled epoxy adhesive is about one-third that of solder. Since the loss of volume is 50 percent, only one-sixth as much CA by mass is required [23,24,77]. Some cost comparisons [25] actually indicate that CAs are very competitive when the time saved due to eliminating cleaning steps and the smaller amounts of CA needed to do the same job as solder are considered.

To reiterate, the advantages to CAs over solder are

1. Elimination of hazardous (lead-containing) materials
2. Lower processing temperature
3. Ability to achieve smaller pitch size
4. Elimination of processing steps
5. Ability to attach nonsolderable materials
6. Ability to customize the material for the application

The disadvantages are

1. Longer curing time for CAs than reflowing time for solders
2. Higher cost
3. Lower strength in the drop test
4. More critical planarity and accuracy of placement of components because CAs do not wick
5. Difficulty in reworking (removal and replacement of a component)

Other authors have brought up additional advantages and disadvantages specific to their research. Goward et al. discussed that an advantage to CAs is that they do not contain tin, which is prone to dendritic growth—a source of bridging in solders [78]. They also mentioned the disadvantage of bond-strength degradation when CAs are exposed to humidity. Gilleo discussed the effects of humidity exposure on resistance measurements in CAs [77]. He thinks that the rise in resistance is due to oxidation of the materials being connected, and that the CAs provide a path for the oxygen to reach the pad or lead surfaces. Gilleo also expressed concern for the potential of electromigration to occur, since the silver particles, particularly in ACAs, carry very high current densities. In none of the literature, however, were instances found where Gilleo's concern was substantiated. Kreutter et al. feel that CAs are better able to withstand thermal shock and cycling than solders owing to the elastic nature of the polymer matrix in CAs [65]. Disadvantages that they discussed are the reduced shelf life of CAs (approximately one year when stored at –40 °C for many one-component, epoxy-based CAs), and the operating temperatures of CA joints that are lower than those of solder joints (below T_g for most CAs).

For evaluating conductive adhesives for different applications, the standard tests typically involve assessment of the electrical properties under various environmental conditions. Most laboratories measure the change in the contact resistance of an actual component attached with CA following thermal cycling, thermal soaking, or temperature/humidity exposure. The contact resistance is measured after a given number of cycles or hours of exposure. If the contact resistance has increased by 20 percent, the component has failed. Typically, no further evaluation is conducted to determine why the resistance has increased.

In addition to measuring the contact resistance, some laboratories have also evaluated the mechanical behavior of the CA joint with respect to temperature and/or humidity exposure. Most of these laboratories assessed the shear strength of the attached component through use of a shear-strength tester [29,36,48,50,51,68,79–84]. Values for peel strength, mainly in applications using anisotropic conductive adhesives, have also been reported [42–45,53,63,65,69]. Another mechanical evaluation test—the pop-off or push-off test—was used by Hvims [37–41] and in all the work reported by Chung et al. [59, 85–88]. In none of these cases was the specimen or the test procedure fully described. The tests appear to have been designed strictly to determine the load required to remove the component, for comparison only.

Four research groups used the CA material to make lap-shear specimens to evaluate the shear properties of the CA in a more conventional test [34,89–92].

4.2 Materials Evaluated

Tests presented here were conducted on two materials, both supplied by the same electronic materials and adhesives company. Both materials are ICAs, but one is a paste and the other, a film. Table 3 shows the properties of the materials as specified by the manufacturer. The ICAs were stored in a standard freezer for about three months and then moved to an ultra-low-temperature freezer set at –45 °C.

The specimens were made up of copper and CA, as shown in figure 22. Copper was chosen because it is likely to be used in conjunction with CAs. The copper was not combined

Table 3. Properties of the CAs as supplied by the manufacturer.

Property	5025E Film	8175A Paste
Filler	Silver	Silver
Cure condition	½ h at 150 °C	3 min at 150 °C
Cure option	2 h at 125 °C	6 min at 130 °C
Lap shear strength Al to Al at 25 °C	363 MPa	247 MPa
Volume resistivity	0.0002 Ω·cm	0.0003 Ω·cm
Ionic content:		
chloride	50 ppm	37 ppm
sodium	30 ppm	1 ppm
potassium	5 ppm	1 ppm
T_g	90 °C	80 °C
Coefficient of thermal expansion:		
below T_g	65 ppm °C^{-1}	65 ppm °C^{-1}
above T_g	150 ppm °C^{-1}	250 ppm °C^{-1}
Weight loss at 300 °C	0.60 percent	0.40 percent
Storage life	6 months at 5 °C	6 months at –10 °C 1 year at –40 °C

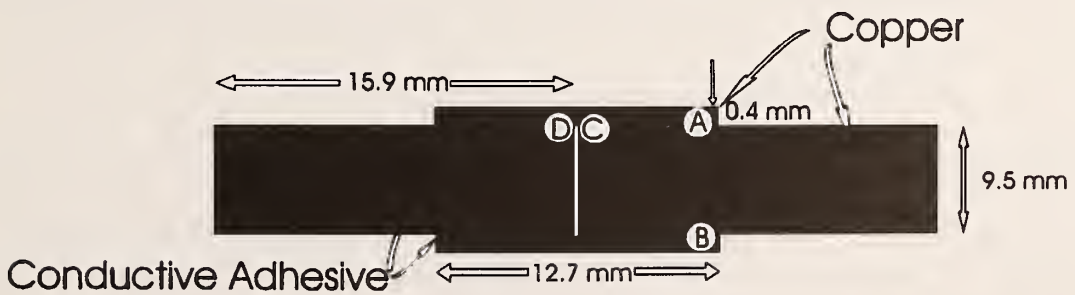

Figure 22. Sketch of the specimen configuration used in the thermal and mechanical-loading tests. The sites of the observed patterns are A—paste thermal test, B—film thermal test, C—paste mechanical test, and D—film mechanical test.

with another material so that the behavior of the CA alone could be easily observed, apart from the influence of mismatch of coeffiecients of thermal expansion in a multiple-material system.

Standard OFHC copper was machined into two sizes, 12.7 mm × 12.7 mm × 0.4 mm and 15.9 mm × 12.7 mm × 9.5 mm. While the CAs thawed at room temperature for 1 h, the copper pieces were soaked in a 50:50 solution of nitric acid (70.6 percent) and deionized water to remove the oxide layer. The larger pieces sat in the acid solution for ~90 s, and the thinner pieces, for ~20 s. The pieces were rinsed in deionized water and then put into a methanol ultrasonic bath for 30 s. The copper pieces were blown dry with compressed air, and the pieces were assembled as shown in figure 22.

The film was applied to both 12.7 mm × 12.7 mm pieces, preheated to 50 °C on a hot plate, then attached to the 15.9 mm × 12.7 mm pieces. A 140 kPa strain-gage clamp was used to apply pressure during cure. The manufacturer recommends preheating the surface to be bonded to 45 °C and curing with continuous pressure of at least 35 to 70 kPa. The specimen was cured in a strain-gage oven with the temperature set to 150 °C. The temperature of the oven was monitored with a 90 mm × 90 mm × 26 mm block of aluminum with an imbedded thermocouple. The specimen cured on the surface of this aluminum block. The thermocouple indicated a temperature of 149.6 °C when the specimen was placed in the oven. When the temperature of the oven began to rise, after dropping from opening the door to put the specimen in, timing began for 30 min, the time required for the film to cure. At the end of this period, the specimen was removed from the oven and allowed to cool to room temperature before removing the clamp.

The other specimen was made with a CA paste. The CA was stroked onto the surface to be bonded with a wooden stick. Teflon tape was wrapped around the 15.9 mm × 12.7 mm pieces to prevent a butt joint from forming. The specimen was assembled and cured without pressure in the oven set to 150 °C. The temperature on the aluminum block was 146.5 °C when the specimen was placed in the oven. The curing schedule for this CA is 3 min at 150 °C or 6 min at 130 °C; 3 min is not enough time to thoroughly cure the CA at 150 °C. (In a previous attempt to cure this CA, the specimen was exposed to 6 min at 130 °C, plus 3 min at 150 °C in an oven, followed by a 3 min cure at 150 °C on a hot plate before it appeared to be fully cured.) Once the temperature started recovering, the specimen was allowed to cure for 6 min. The specimen was then removed from the oven and allowed to cool to room temperature.

4.3 Specimen Preparation

The day after the specimens were cured, each was cut into approximate thirds, so that each piece was about 3 to 4 mm thick. Each piece was ground flat on both sides with silicon carbide paper in several steps, from 120 to 1200 grit. One side of each specimen was then polished with 6 μm diamond spray on a napless synthetic silk polishing cloth. Following the polishing, the surface was cleaned with methanol and cotton batting and dried with canned compressed air.

After the specimens had been prepared and the film and paste's shelf life had expired, it was discovered that the projected shear strength of the CAs exceeded the tensile strength of

the thin copper pieces used in the specimens. The specimens had to be modified to keep the study progressing. The best option appeared to be reinforcing the 0.4 mm thick copper pieces for the mechanical loading specimens. Small pieces (12.2 mm × 3 mm × 1 mm) of 316LN stainless steel were glued onto the copper sheet with a low-shrinkage epoxy that cured at room temperature. During curing they were held together with binder clips, producing an indeterminate pressure. The polishing described above was then repeated.

The crossed-line gratings were prepared on each of the four specimens on a different day. On the day that the crossed-line gratings were written, each specimen received a final polish with 1 μm diamond spray on synthetic silk polishing cloth. Once again, the specimen surface was cleaned with methanol and cotton batting and dried with canned compressed air. The specimen was placed in a methanol ultrasonic bath for 30 s, followed by cleaning the surface with acetone and cotton batting and drying it with canned compressed air.

To apply a thin, even coat of the PMMA, it was spun onto the surface of the specimen. The PMMA was purchased in a chlorobenzene solution with 4-percent solids. This was cut in half by mixing a 1:1 solution of the purchased PMMA with chlorobenzene to form a solution with 2 percent solid content of PMMA. The specimen was held onto the surface of the spinner by a vacuum; 3 to 5 drops of 2 percent PMMA were placed on the surface of the specimen; the specimen was spun at 2250 rpm for 30 s. The specimen was then placed on an aluminum block preheated to 170 °C on a hot plate. The specimen was allowed to bake at this temperature for 1 h to drive off the chlorobenzene. The specimen was now ready for lithography.

4.4 Electron-Beam Lithography

For lithography performed in a SEM, D. T. Read of NIST wrote a BASIC program that controls the location and dwell time of the electron beam, enabling regularly spaced, straight lines to be written. The lines are actually a series of closely spaced, overlapping spots. To obtain crossed-line gratings, the lines are written in one orientation first; then the specimen is "rotated" 90° and the lithography process is repeated. This "rotation" takes place electronically rather than physically—the x output is sent from the photomultiplier to the video y input, and vice versa. The effect is to rotate the specimen clockwise ~90°. (The rotation is accurate to ±1° and precise to ±20 s.)

Using a data file accessed by the program, the operator specifies the size of the pattern in magnification, the number of lines, the probe current, and the number of dwell stops on the scan line. Table 4 shows the settings used for the patterns written on the specimens for this study. The PMMA is very sensitive to the electron beam, so the operator cannot view the surface of the specimen under normal illumination but must locate the pattern with an extremely low probe current (<0.2 pA).

To write the patterns, the microscope was set to 20 kV of accelerating voltage. An aperture of 50 μm was chosen to focus the beam as tightly as possible. The astigmatism, centering of the aperture, working distance, and focus were also carefully adjusted and tuned to obtain as small a spot as possible. A small electron-beam spot is necessary, particularly when attempting to obtain line pitches of 90 to 225 nm.

Table 4. Input values to the lithography program for the patterns written on the specimens for this study.

Form	Magn.	Dose, nC cm^{-2}	Probe current, pA	Pattern size, μm	Pitch, nm
Film	200×	2.4	200	500	450
	200×*	2.5	200	500	450
	200×	2.6	200	500	450
	500×*	1.4	50	200	350
	500×	1.6	50	200	350
	500×	1.7	50	200	350
	500×	0.7	25	200	180
Paste	200×*	2.5	200	500	450
	200×	2.6	200	500	450
	200×	2.7	200	500	450
	500×*	1.3	50	200	350
	500×	1.4	50	200	350
	500×	1.6	50	200	350
	500×	1.7	50	200	350
	500×	0.6	25	200	180
	500×	0.8	25	200	180

*Pattern used in thermal or mechanical test.

Writing the actual patterns is a matter of locating where you want to place the pattern, setting the magnification to the desired viewing area, and adjusting the probe current with the fine and coarse potentiometers on the SEM to that specified in the computer data file. A Faraday cup measures the probe current. It also blocks the beam from reaching the surface of the specimen until the computer takes control of the electron beam to begin writing the pattern.

After all the patterns were written on a given specimen, the specimen was removed from the SEM for development. During exposure the electron beam breaks up the polymer chains of the PMMA, but development of the specimen is required to wash those broken polymer chains away. The developer used was a 3:1 solution of isopropanol and methyl isobutyl ketone (MIBK). The specimen was gently agitated in the isopropanol/MIBK solution for 40 s, then rinsed in a stream of isopropanol for 20 s, followed by a rinse in deionized water for 30 s. Canned compressed air was used to dry the specimen. At this point, often the diffraction of light on patterns with line pitches >350 nm can be seen. The lines are visible in an optical

microscope for line pitches of the same magnitude, but the quality of the lines with finer pitches must be assessed in the SEM. Following development, however, the surface of the specimen is a nonconductive polymer. This surface will charge in the SEM so that it is impossible to view the patterns. To provide a conductive surface, a thin (<10 nm) coating of gold–palladium was deposited over the polymer with a sputter coater. A sputter coater plates material onto a surface by dislodging material from a source with argon ions accelerated in an electric field and depositing the source atoms onto the surface of the specimen. The specimen remains cool throughout the process.

After its surface was coated with gold–palladium, the specimen was returned to the SEM, and the quality of the patterns was evaluated. A pattern can be rejected for use for three reasons: overexposure, underexposure, or inconsistent exposure. Inconsistent exposure arises when the specimen is not perfectly flat in the area of the pattern—either the specimen as a whole is not flat or the softer regions are gouged out. If the electron beam's focal point falls above the specimen surface, the inadequate exposure will result in invisible or poorly contrasting lines. If the electron beam's focal point falls below the specimen surface, the interaction area affected may be so large that adjacent lines may touch each other or all the PMMA is exposed and removed during development.

Achieving acceptable patterns on each of the material forms was straightforward for three of the specimens prepared (both specimens containing the CA film and the paste specimen prepared for thermal loading). The paste specimen prepared for mechanical loading presented more difficulty. The first attempt at lithography generated some usable patterns, but it had been instrumented before it was recognized that the specimens were underengineered. The second attempt did not result in any usable patterns. Greater effort was made to make the specimen flat and the interfaces contiguous. The third attempt at lithography revealed an interference problem that resulted in wavy and discontinuous lines. Investigation revealed that three welding units in use near the laboratory created this interference. It is not clear whether the interference was due to rf or dc fields.

4.5 Thermal Testing

The thermal-load testing of each CA material was conducted in the SEM by using a commercial heating/cooling stage (fig. 23) with a temperature range of –196 to 400 °C, but the testing was conducted in the nominal range of –50 to 150 °C. Cooling was provided by liquid-nitrogen–cooled nitrogen gas that flowed through tubing in the stage. A PDI controller maintained the set temperature by balancing the heater output with the chilled air.

One of the patterns on the paste specimen, location A in figure 22, was observed under a low accelerating voltage (7 kV) to optimize the resolution without damaging the PMMA. The paste specimen was observed at a working distance of 13 mm and a probe current of 10 pA. Before acquiring any images the stage was precycled between 0 °C and 100 °C twice and then returned to the ambient temperature noted when the filament first saturated. The objective was to ensure that any macroscopic adjustments would occur prior to the start of image acquisition. The hour required to do this precycling also gave the electron beam time to stabilize. Images were then stored digitally from both orientations at ambient temperature. (Throughout the remainder of this paper, *u*-field and 0° will refer to the observed images where the grating

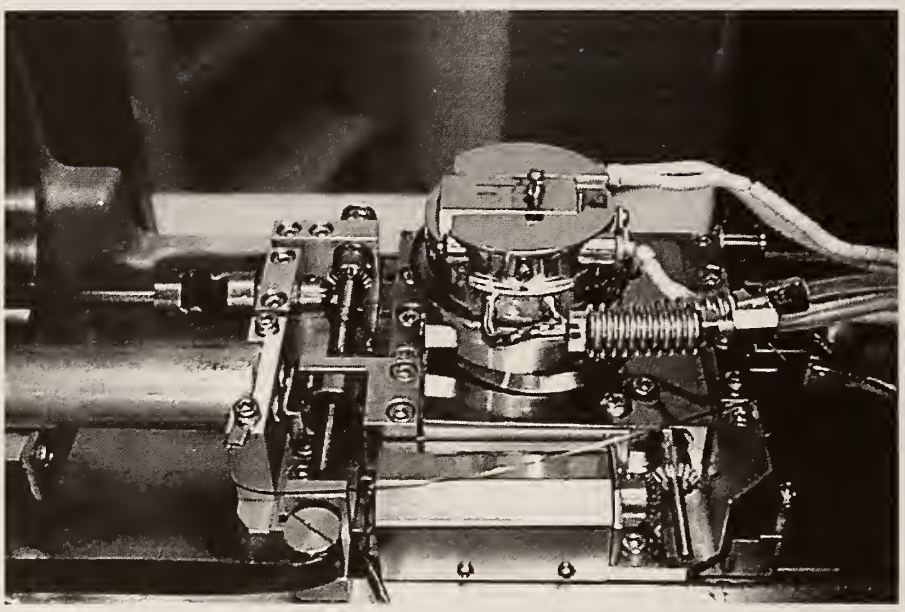

Figure 23. The heating/cooling stage used.

lines were perpendicular to the interface; *v*-field and 90°, to images whose grating lines were parallel to the interface.)

Subsequent 0 and 90° images were acquired at the following nominal temperatures:

–8 °C	–48 °C	6 °C
52 °C	100 °C	150 °C
80 °C	30 °C	

The fringes on every image were traced by using a program for the PC that was written by D. T. Read of NIST.

The pattern on the film specimen (location B in fig. 22) was observed at a working distance of 14 mm and a probe current of 12 pA. In this case, images were collected from the 0 and 90° orientations an hour after saturating the filament but before thermally cycling the stage. The stage was then cycled between 0 and 100 °C twice, as before. A second pair of images was acquired at the noted ambient temperature after the thermal cycling. These images were used as the initial condition for the test. Digital images from the 0 and 90° orientations were stored for the following temperatures:

–10 °C	–50 °C	0 °C
52 °C	101 °C	150 °C
80 °C	10 °C	–45 °C
29 °C		

The fringes on each image were traced with the program described above.

The data appeared to be behaving in an unusual fashion. Fringe density decreased when it was expected to increase. To verify the results of the first test, a second thermal-loading test was run on the same pattern used above. The electron beam was again allowed to stabilize for

an hour before acquiring images from the two orientations. The stage was cycled between 0 and 100 °C twice and then returned to the noted initial temperature. Images from both 0 and 90° were obtained before thermally loading the specimen to the following temperatures:

–50 °C	1 °C	52 °C
101 °C	150 °C	80 °C
13 °C	–47 °C	30 °C

The fringes on each image were traced, as before.

4.6 Mechanical Testing

The mechanical tests were conducted in the SEM on a commercially manufactured stage (fig. 24) with a motor-driven screw-type actuator and a load capacity of ~4450 N. With the present hardware, the stage is capable of only uniaxial compression and tension. A universal joint to drive the stage and the wires that monitor the load and displacement have access into the SEM chamber through a plate that replaces the side port.

The gage length of the specimen is limited to ~15 mm. The modified lap-shear specimen has been described previously (see fig. 22). It is loaded onto the stage with wedge grips, each end of which is tightened with two bolts. The motor speed is regulated with a potentiometer-type knob that sets the rate between 0 and 100 percent of 330 rpm. The stage showed no visually discernable movement below 10 percent, however. Most of the loadings were conducted at ~15 percent; loading to 90 N takes less than a minute. The load was read from a digital display on the controller for the stage.

Both mechanical tests were performed on the same day. The patterns used had crossed-line gratings with a pitch of ~350 nm, so data were again available from both the 0 and 90° orientations. The patterns were located near the midpoint of the copper sheet; that is, near the inside free surface of the larger copper block; their locations in figure 22 are indicated by C for the paste specimen and D for the film specimen.

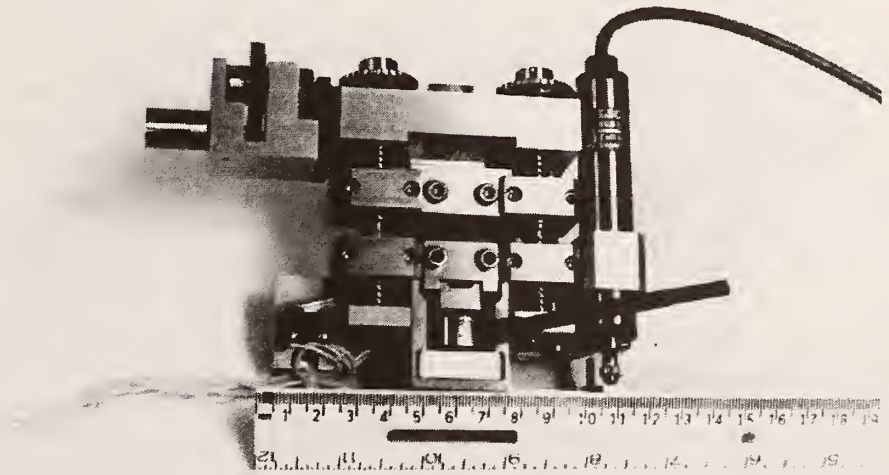

Figure 24. The mechanical stage used in this study.

The first test conducted was on the specimen containing the CA paste. The moiré was observed at an accelerating voltage of 7 kV, a working distance of 18 mm, a probe current of 15 pA, and a magnification of 550×. The filament was saturated 130 min before the first images were acquired. Images from both orientations were accumulated at nominal loads of:

0 N	82 N	178 N	260 N
344 N	429 N	516 N	601 N

A final set of images was also acquired at 0 N after the test was completed. The images were imported onto a PC where the fringes were traced on each image by using the aforementioned tracing program.

The second test was conducted on the specimen containing the CA film. The working distance for this test was 17 mm. The accelerating voltage was 7 kV, the magnification was 550×, and, at the start of the test, the probe current was 15 pA. The probe current was reset to 18 pA after the 247 N load was applied because the contrast was poor and the fringes in the CA were difficult to see. Owing to time constraints, the filament was saturated for only 25 min before the first images were acquired. Images were accumulated from both orientations at the following nominal loads:

0 N	84 N	163 N	247 N
331 N	420 N	504 N	539 N

The images were again imported to a PC, where the fringes from each image were traced with the tracing program.

4.7 Analysis of the Moiré Fields

The fringe-tracing program enables the assignment of point loci that define the center of the fringe. This fringe center is also a contour of equal displacement on the surface of the specimen. The effect of the crossed-line grating is analogous to having a full-view 0-to-90° displacement gage with a resolution on the order of tens of nanometers.

Once the fringe centers have been identified, analysis is completed in the manner described by Parks [93] in his chapter on geometric moiré. Figure 25 shows the general procedure followed. The fringe centers are identified on the *u*-field and *v*-field images. Line profiles are chosen running perpendicular and parallel to the orientation of the lines of reference grating on each image. For the series of tests described here, three line profiles were chosen perpendicular to the orientation of the lines of the reference grating in each of the *u*-field and *v*-field images, and one trace was chosen at the midpoint of the images from the *u*-field and *v*-field images parallel to the orientation of the lines of the reference grating (fig. 26). For the *u*-field images, the three line profiles were chosen such that one was through the CA and the other two were approximately equidistant from the CA, one in the 9.5 mm copper and the other in the 0.4 mm copper.

The distance along the chosen trace versus the assigned fringe order was graphed. The fringe order was then converted into length by multiplying by the pitch p_r of the reference grating. (Recall that each fringe is the result of a frequency mismatch between the specimen and the reference gratings of one complete line.) The example shown in figure 25 assumes that the initial fringe field is null. However, with e-beam moiré the initial fringe field is rarely null; every subsequent image is analyzed by studying the difference between it and the initial image.

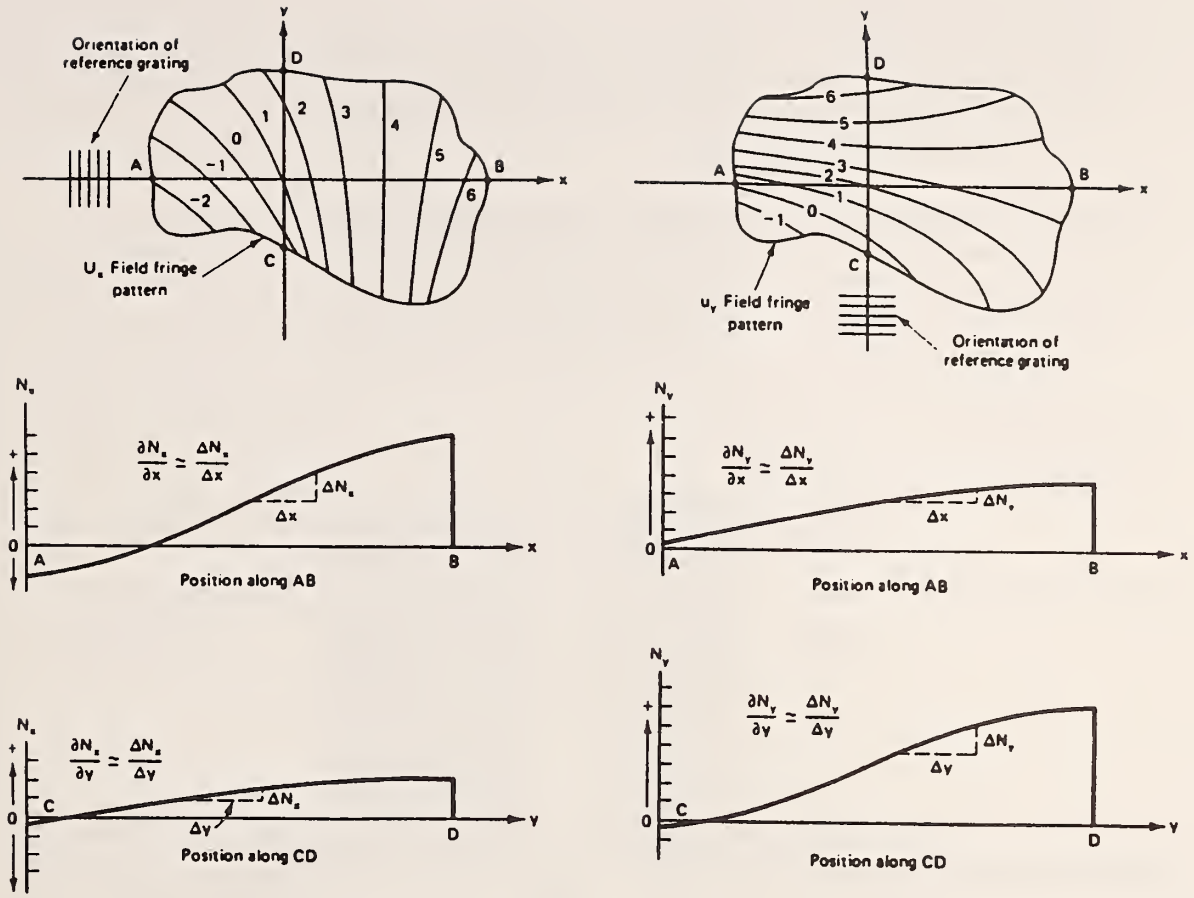

Figure 25. Procedure used to analyze the moiré fringe data. (From V.J. Parks, Geometric moiré, in *Handbook on Experimental Mechanics,* edited by A.S. Kobayashi, first edition, published for the Society for Experimental Mechanics, Inc., Englewood Cliffs, NJ: Prentice–Hall; 1987 [93]. Used with permission of Prentice–Hall.)

In the thermal tests an initial room-temperature image was collected, followed by images collected at regular temperature intervals between –50 and 150 °C. Similarly, in the mechanical-loading tests an image was collected before applying a load; then subsequent images were collected at regular load intervals. The slopes obtained from the line profiles from the initial images must be subtracted from the subsequent images to see how each loading step affected the fringe field. Strain data are calculable from these plots of relative displacement versus position along the trace. The slope of the curves, *du/dx* and *dv/dy*, from the line profiles perpendicular to the orientation of the reference grating in the *u*-field and *v*-field images, respectively, are the normal strains as given by eq (8). The shear strain is the sum of the slopes from the curves obtained parallel to the orientation of the lines of the reference grating, *du/dy* + *dv/dx*, as given by eq (13). The strains are, therefore, quantifiable and locally significant.

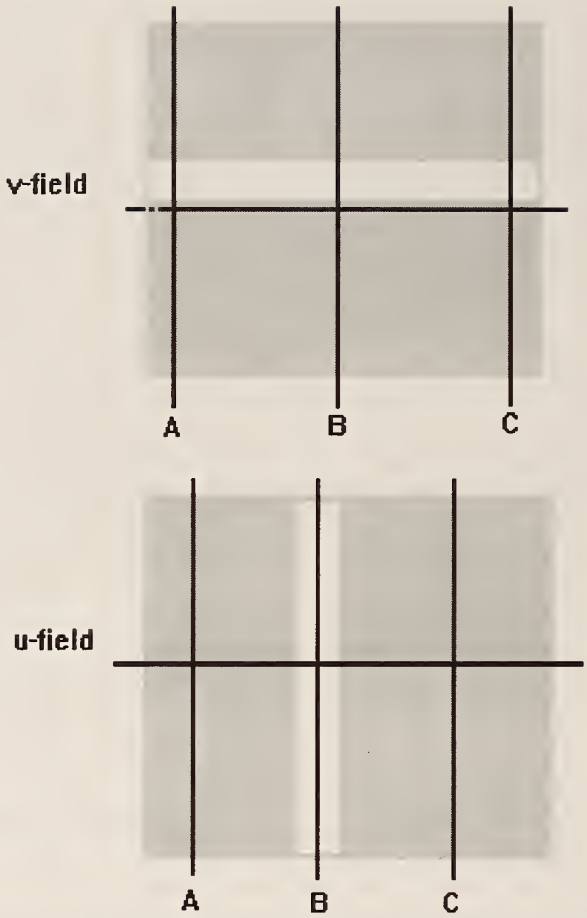

Figure 26. Sketch showing the approximate locations of the line profiles from the *u*-field and *v*-field images used to analyze the moiré data.

4.8 Results

4.8.1 Thermal Loading of Conductive-Adhesive Paste

As one looks at the collected images of the fringe field at each temperature, the amount of local deformation that occurred in the CA is notable. In figure 27a of the *u*-field, the fringes curve through the CA paste and the fringe density is not regular. The corresponding *v*-field image (fig. 27b) shows the fringes following a circuitous path through the CA.

The analysis of the series of the *u*-field images (fig. 28) shows that the behaviors of the thin copper, the CA, and the thick copper were all very similar. Below room temperature the curves exhibit a gentle negative slope, indicative of contraction. Above room temperature there is little sign of expansion at 50 °C, especially in the thin copper. At 100 °C the slope of all three line traces is larger, and the slope is largest at 150 °C. The magnitude of the slope when the temperature increases 100 °C is far greater than it is when the temperature decreases 100 °C. In referring to table 3, a possible reason emerges—the glass transition temperature T_g of the paste is 80 °C, and, beyond T_g, the coefficient of thermal expansion nearly quadruples.

Another significant point is the behavior of the curve at the two highest temperatures, particularly in the thin copper and in the CA. In both cases the slope flattens out as it approaches the top of the image. The pattern is located at the edge of the lap of the specimen. The flattening of the slope is the effect of the free surface on the thin copper and the CA. That is, no normal or shear stresses (or corresponding strains) exist at a free surface.

The displacement-versus-position curves for the *v*-field show very unusual behavior at the higher temperatures (fig. 29). Up through 50 °C, the curves act in a regular and supportable manner. As the temperature decreases, the slope becomes increasingly more negative, with a steeper negative slope occurring in the CA. As the temperature increases, it looks as though the material will behave in the reverse fashion at 50 °C; the curve demonstrates a positive slope, becoming more positive through the CA. However, at 100 °C, the slope becomes slightly negative, and at 150 °C, significantly negative through the CA. It is clear that locally, around the CA, the fringe field passed through null between 50 and 100 °C, and the fringe density started to increase in the region, giving the appearance of being in a state of contraction, whereas the region was actually in a condition of greater expansion.

The shear strain in this test was not significant, so the data were not analyzed and will not be discussed here.

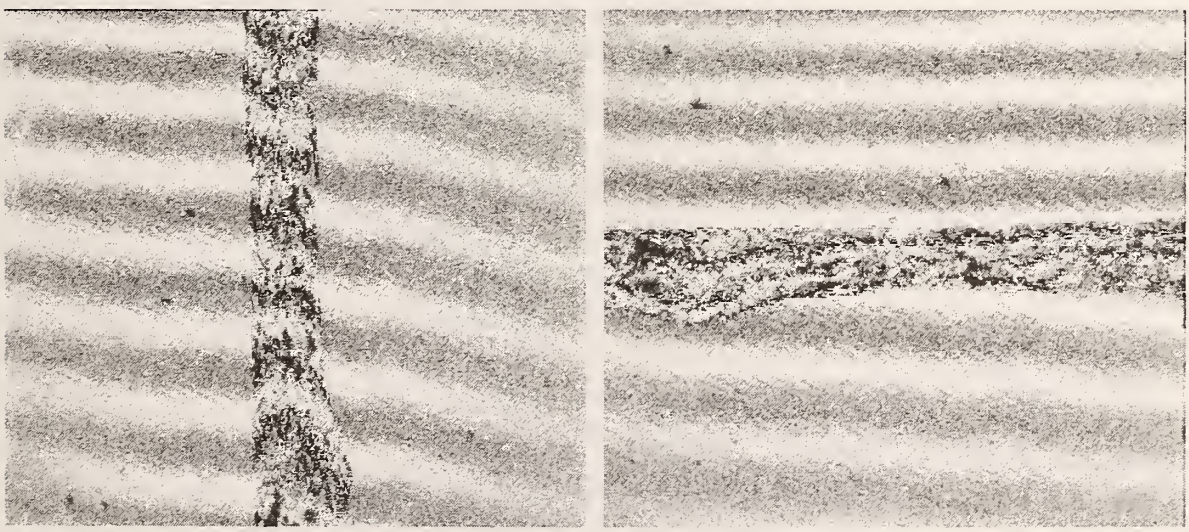

(a) (b)

Figure 27. Images at 220× from the thermal-loading test on CA paste specimen acquired at 150.2 °C of (a) the *u*-field image and (b) the *v*-field image.

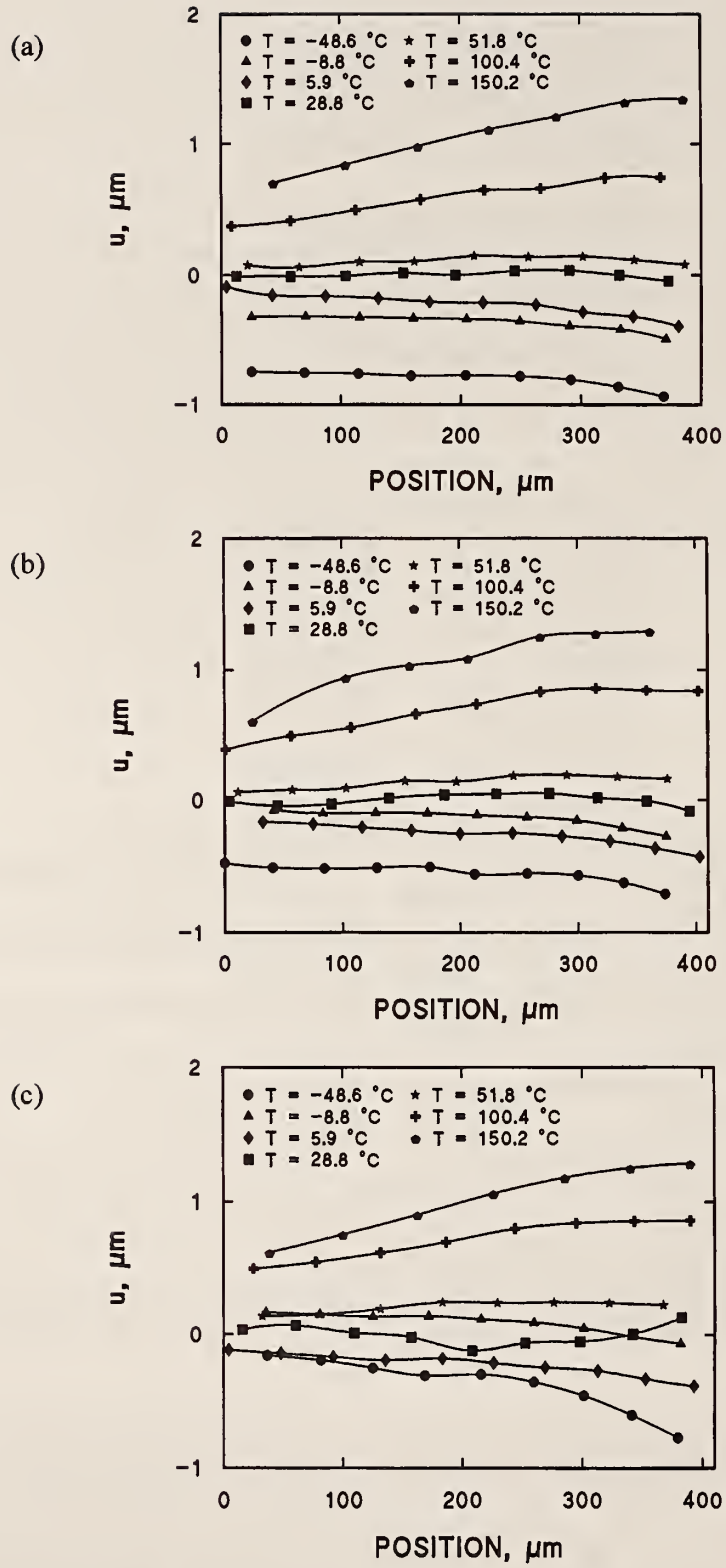

Figure 28. Displacement-versus-position plots of the *u*-field from the thermal-loading test on the CA paste specimen from (a) the 0.4 mm thick copper; (b) the CA; and (c) the 9.5 mm thick copper.

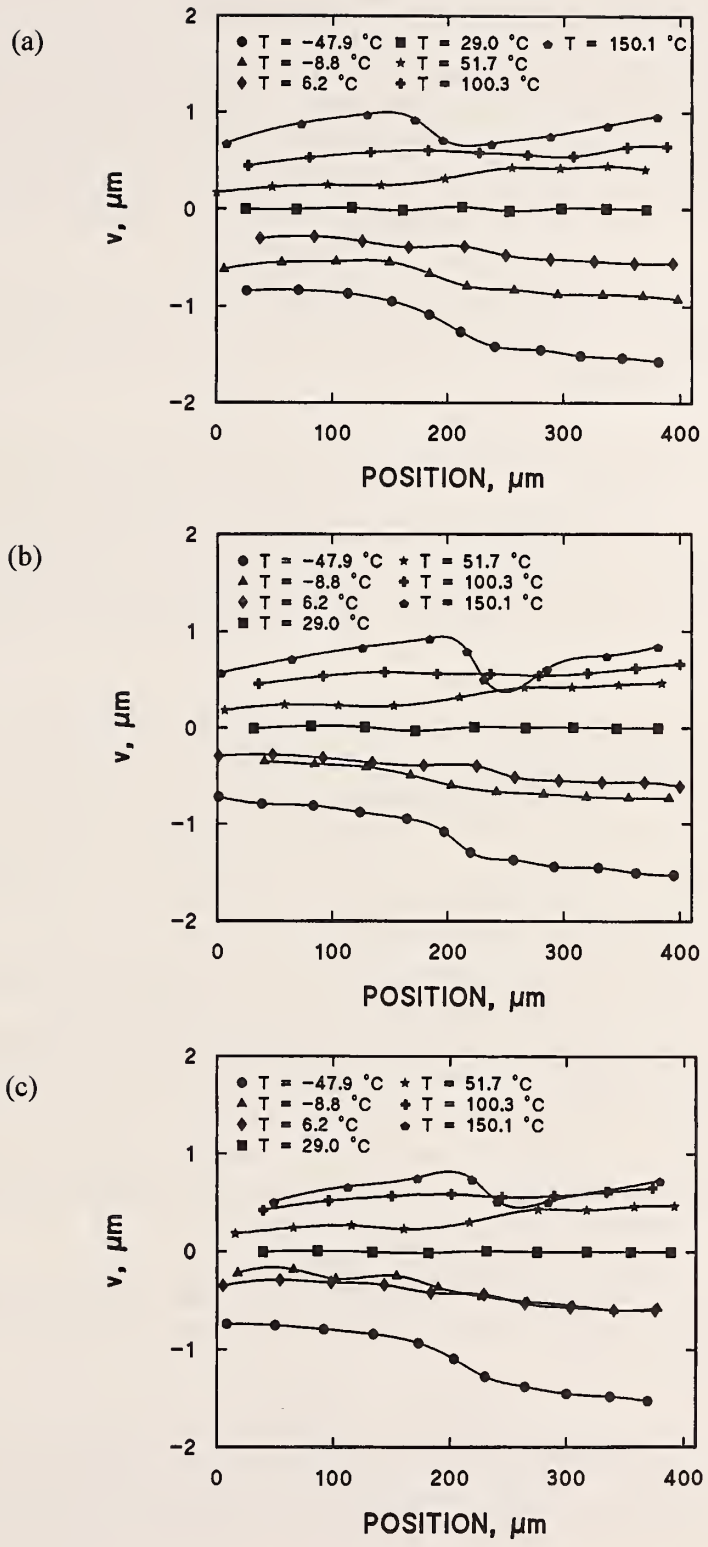

Figure 29. Displacement-versus-position plots of the *v*-field data from the thermal-loading test on the CA paste specimen from the (a) left side; (b) center; and (c) right side of the *v*-field image.

4.8.2 Mechanical Loading of Conductive-Adhesive Paste

The shear strength of the CA paste was evaluated by using the modified lap-shear specimen shown in figure 22 with steel reinforcement added to the 0.4 mm copper pieces. The specimen was loaded in ~90 N increments until catastrophic failure occurred (fig. 30). The failure took place outside the field of view of the pattern studied. It was anticipated by rapid movement of the grating lines, which were being observed, followed by the load dropping to zero.

The images themselves indicated very little activity, either locally or regionally. The fringe density did not change significantly; however, the tilt of the fringes through the CA did change as the test progressed.

At the time the images were collected, an error was made when the microscope was refocussed after the first loading was accomplished. Although the fringe fields did not appear significantly different, it became apparent during analysis that the images acquired at 0 N were not the initial condition for the remaining test. Since plastic deformation could have occurred in the area of the pattern studied, the final 0 N image could not be used for the initial condition either. Therefore, the images from the first load increment (82 N) were used for the initial condition.

Figure 30 shows the displacement-versus-position curves for each line trace in the u-field images. The curves remain essentially horizontal except for the curve acquired at 260 N. That curve displays what seems to be significant compression for all three line profiles as the top of the pattern is neared. This behavior must be considered anomalous for the following reasons:

1. The specimen geometry precludes a location where both the 9.5 mm copper and the 0.4 mm copper on the same perpendicular profile will simultaneously be in compression under uniaxial tensile loading.
2. The pattern itself was located near the midpoint of the specimen, the region where the 0.4 mm copper is subject to the greatest amount of tension.
3. Images acquired at loads above and below 260 N displayed no corresponding behavior, and the loading was smooth and continuous, showing no jumps or drops indicative of a slip occurring outside the field of view.

This anomalous behavior was probably the result of the specimen or stage not being completely stabilized after the loading step was completed, thus, still being in motion during the first 15 s in which the image was being collected.

The horizontal curves for the other load increment show that no strain was detectable. It is intriguing that no strain would be discernable for any load increment applied prior to that which caused catastrophic failure.

Figure 31 of the v-field (displacement-versus-position curves) displays traits similar to those of the u-field images. All the curves are essentially horizontal except for the postfailure 0 N curve. Again, the implication of the horizontal curves is that the material did not strain additionally at any load increment from its initial load of 82 N all the way to nearly 600 N.

The postfailure 0 N curve exhibits a slightly negative slope for all three line traces. There are two possible sources for this fact: (1) This slope difference could be the difference that

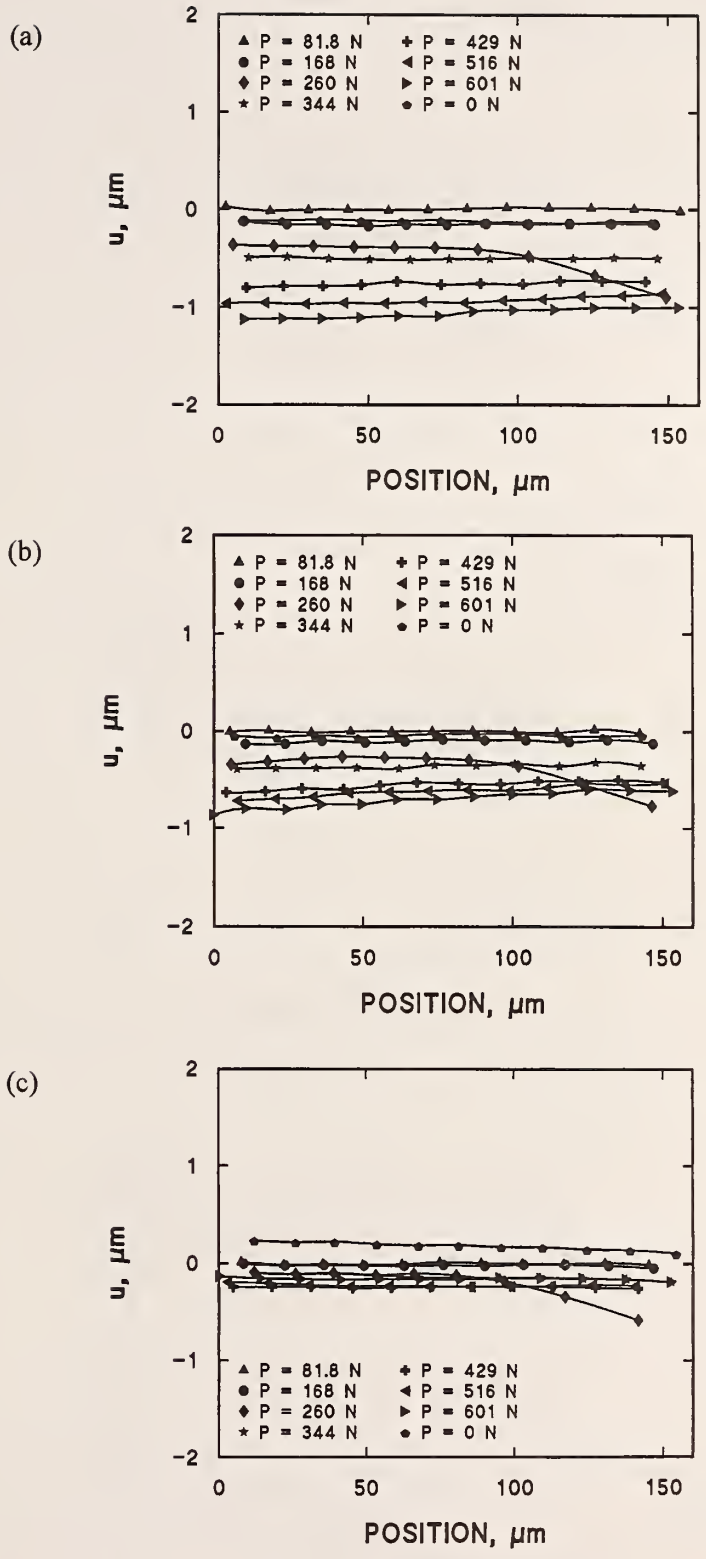

Figure 30. Displacement-versus-position plots of the *u*-field data from the mechanical-loading test on the CA paste specimen from (a) the 0.4 mm thick copper; (b) the CA; and (c) the 9.5 mm thick copper.

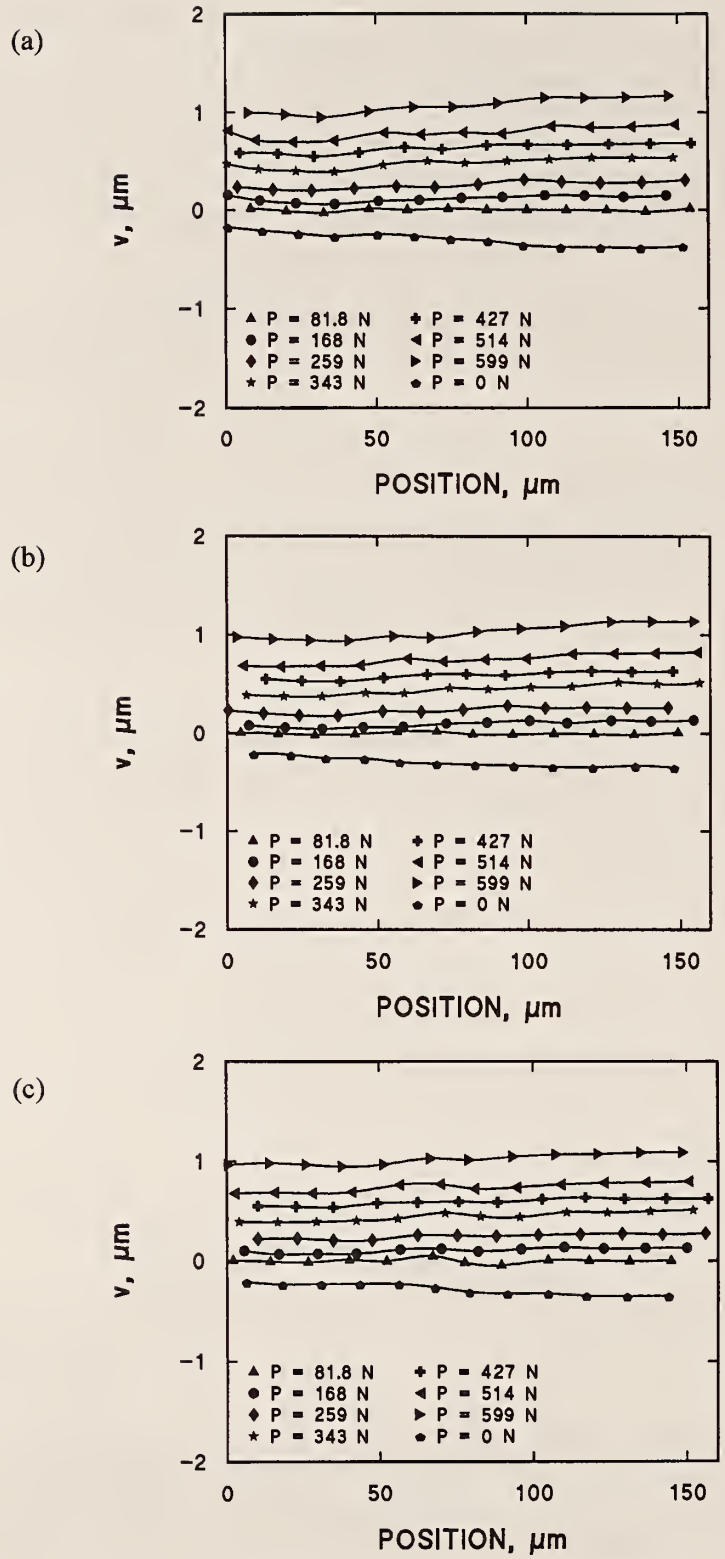

Figure 31. Displacement-versus-position plots of the *v*-field data from the mechanical-loading test on the CA paste specimen from the (a) left side; (b) center; and (c) right side of the *v*-field image.

would have been observed if an initial image with 0 N load had been used. (2) The failure could have caused the specimen to move slightly vertically, changing the focal plane from the surface of the specimen and causing the fringe field to alter.

Even though no normal strains are observed in the *u*- and *v*-fields, the plot of the *u*-field displacement versus the *y* position (fig. 32) shows that shear deformation has taken place. Figure 32 shows that all the deformation was carried in the CA—each additional loading increment results in the slope of the corresponding curve becoming larger in magnitude. In this set of collected images, dv/dx was insignificant, so $\gamma_{xy} \approx du/dy$. Figure 33 shows the shear stress versus shear strain for this data. The elastic region is difficult to identify without a 0 N data point and with so few data points. However, the general shape of the stress-versus-strain curve is distinguishable.

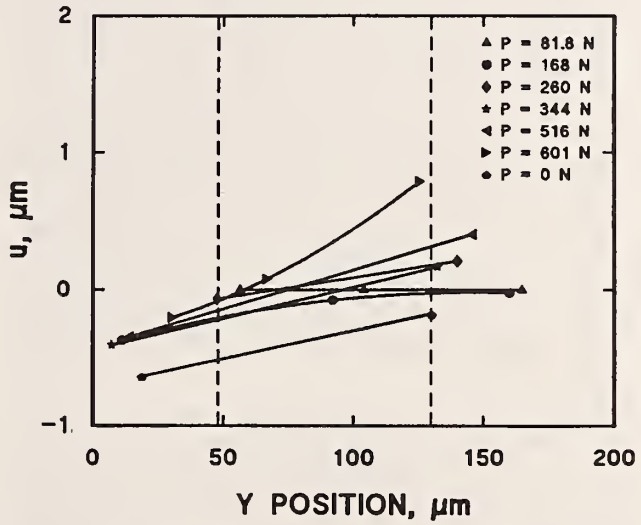

Figure 32. Shear *du/dy* data from the mechanical-loading test on the CA paste specimen.

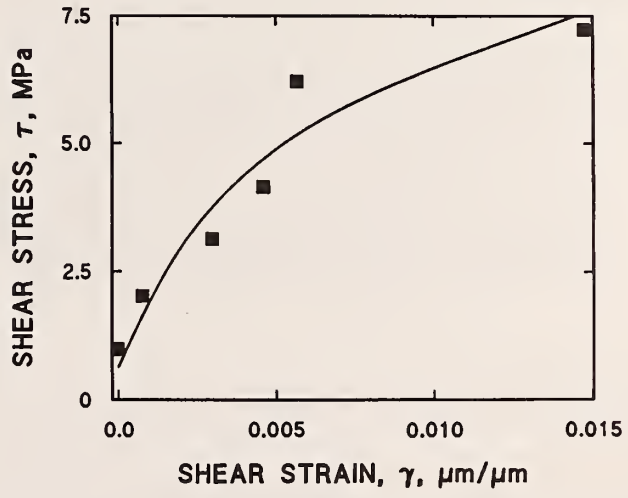

Figure 33. Shear stress-versus-shear strain for the mechanical-loading test on CA paste specimen.

4.8.3 Thermal Loading of Conductive-Adhesive Film

The first image collected from the paste specimen in the 0° orientation showed that the fringes were bending as they crossed the CA. Because the image was acquired after precycling the specimen and stage twice between 0 and 100 °C, whether the shear deformation was the result of relaxation of residual stresses before exposure to temperature extremes or whether it was due to the thermal cycling could not be established. In this test on CA film, images were collected before and after thermally precycling the specimen and stage. Figure 34 shows the ambient-temperature images from the 0° orientation before and after cycling. Evidently, the shear that developed in the CA was the direct result of thermally precycling the specimen and stage between 0 and 100 °C.

When analyzing the data from this test, the postcycling, ambient-temperature images were used for the initial condition The *u*-field data shown in Figure 35 exhibited the anticipated behavior: the slopes became increasingly more negative as temperatures decreased and more positive as temperatures increased for all three line profiles.

Graphs of the *v*-field-displacement versus position are shown in figure 36. Tracing these fringes was very difficult because the fringe center in the CA was ambiguous. The data appear to imply that the CA remains contracted whether the temperature was increasing or decreasing.

A second thermal test was conducted on this same specimen to see if this ambiguity could be cleared. The second test had nearly identical results in the *u*-field, as can be seen from the series of graphs of *u*-field displacement versus position in figure 37. The corresponding *v*-field graphs are shown in figure 38. Very modest strains are exhibited along the line profile furthest from the free edge (fig. 38a), except at 150.2 °C, where a sharply steeper slope is exhibited as the trace position enters the thick copper. Detecting the fringes within the CA was also difficult in these patterns, leaving the strain behavior in the CA somewhat ambiguous. The fringe density in the local region of the CA gives some indication that the pattern experienced a null between 0.7 and 28.4 °C. However, the data are not clear enough to support this claim unequivocally. The line profiles from the center and toward the edge of the specimen (fig. 38, b and c) behave in a regular fashion, with increasing contraction indicated as the profile moves into the thick copper.

Like the thermal-loading test results for the CA paste, the du/dy and dv/dx slopes did not exhibit any significant shearing after the initial deformation took place.

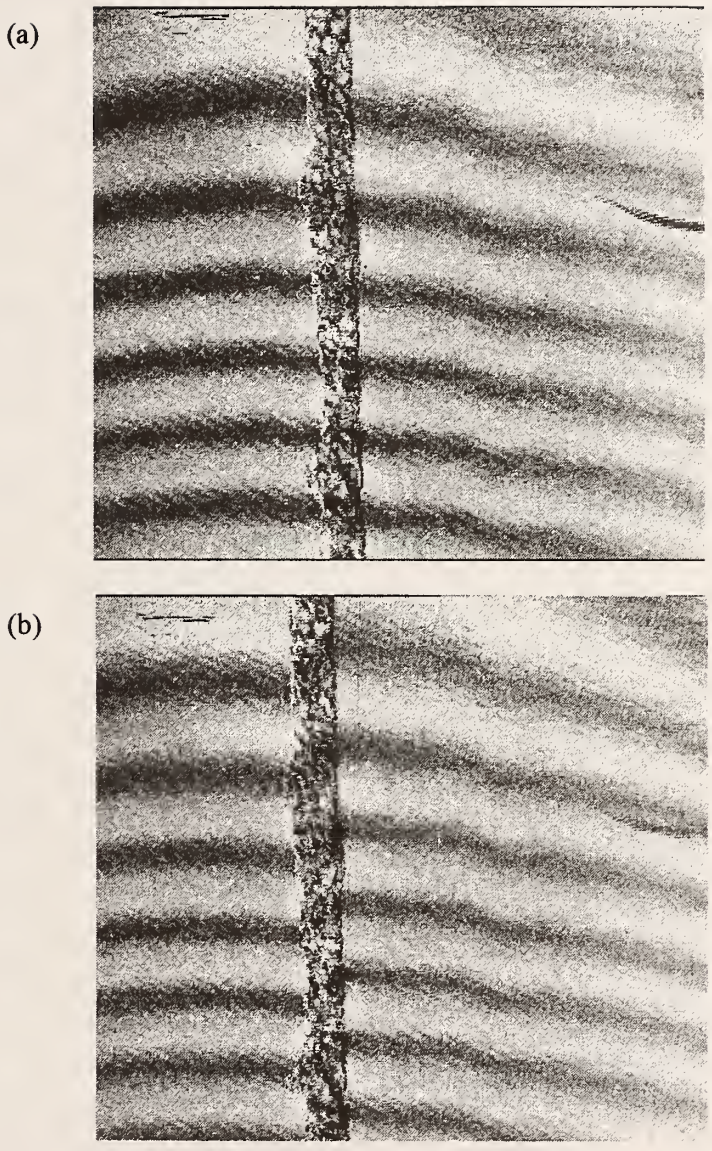

Figure 34. Images of the *u*-field at 220× acquired at ~28 °C (a) before and (b) after thermally cycling the CA film specimen and stage twice between –50 °C and 150 °C.

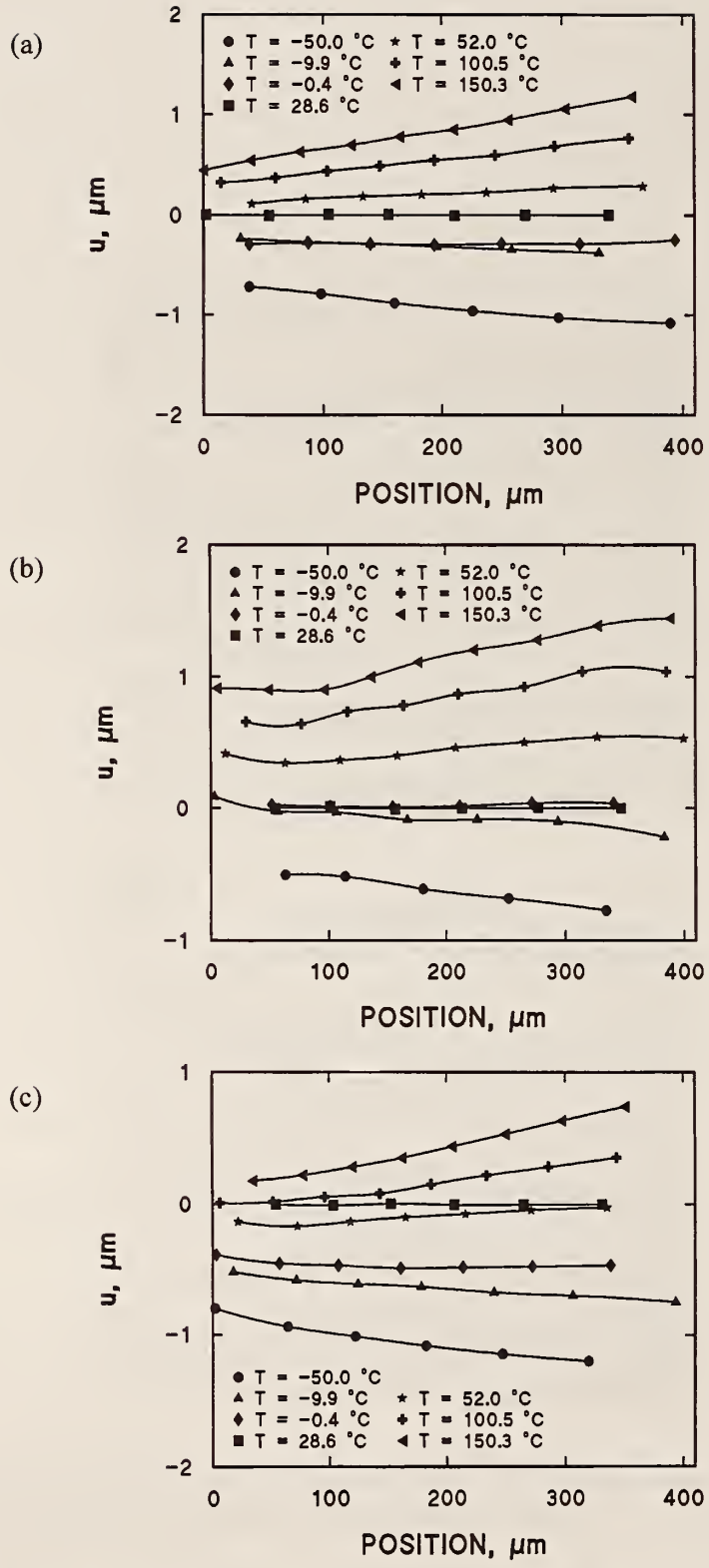

Figure 35. Displacement-versus-position plots of the *u*-field data from the first thermal-loading test on the CA film specimen from (a) the 9.5 mm thick copper; (b) the CA; and (c) the 0.4 mm thick copper.

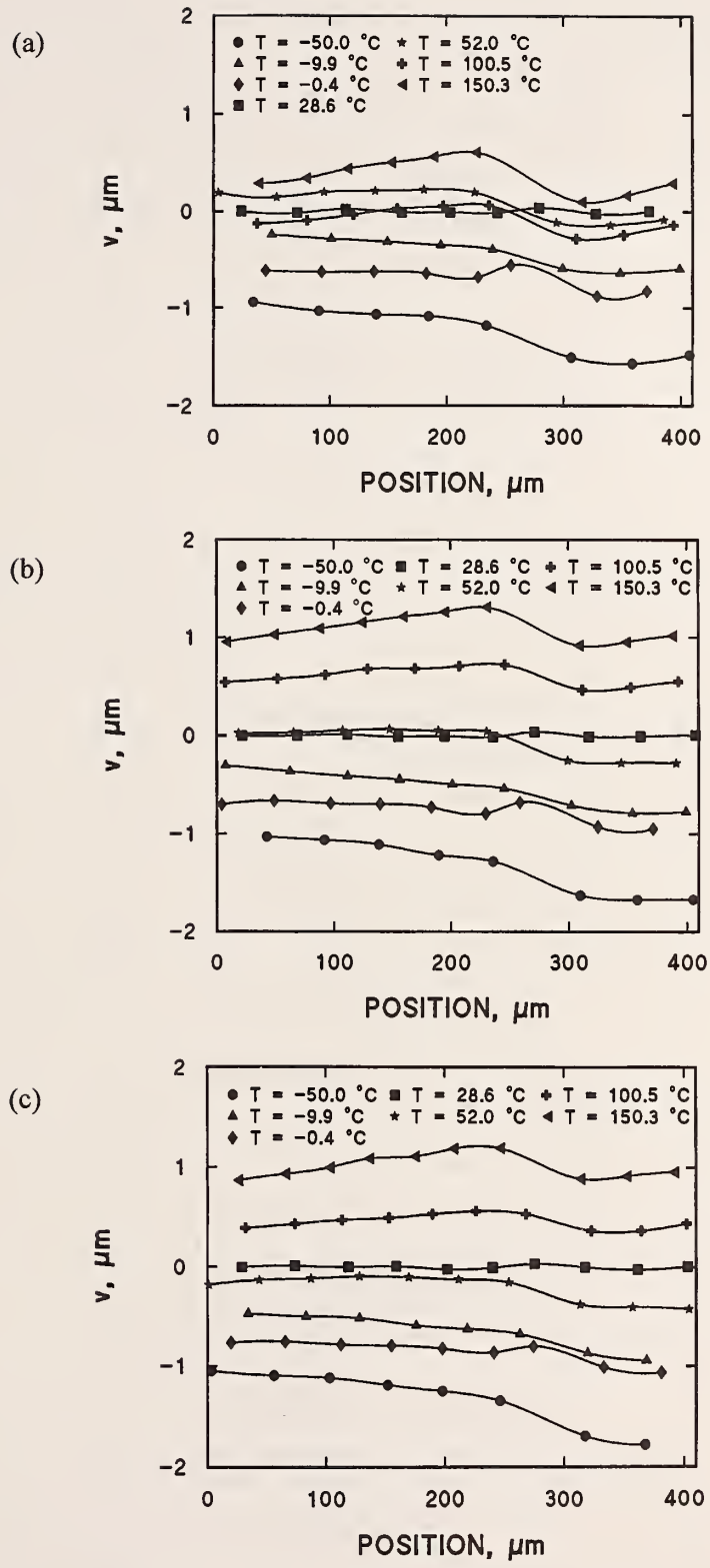

Figure 36. Displacement-versus-position plots of the *v*-field data from the first thermal-loading test on the CA film specimen from the (a) left side; (b) center; and (c) right side of the *v*-field image.

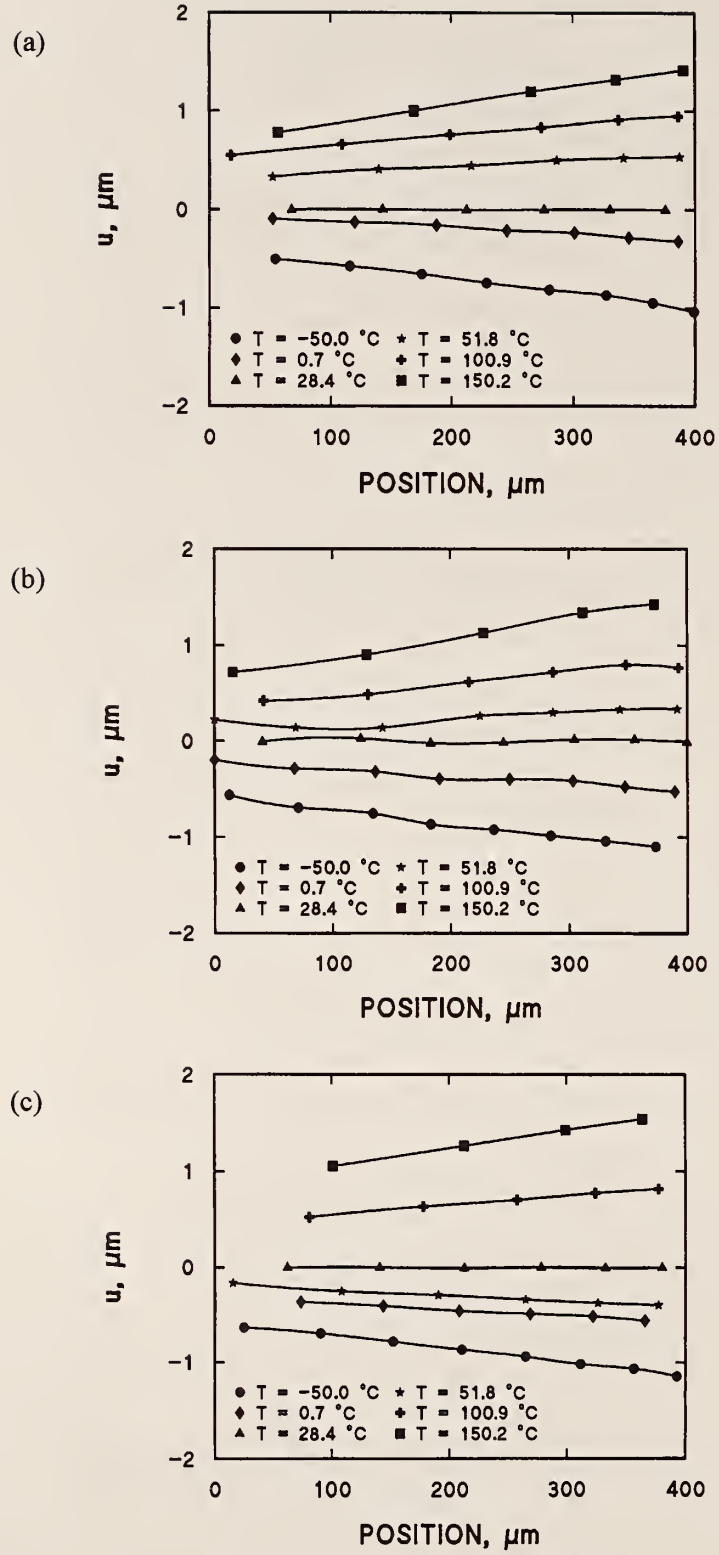

Figure 37. Displacement-versus-position plots of the *u*-field data from the second thermal-loading test on the CA film specimen from (a) the 9.5-mm-thick copper; (b) the CA; and (c) the 0.4-mm-thick copper.

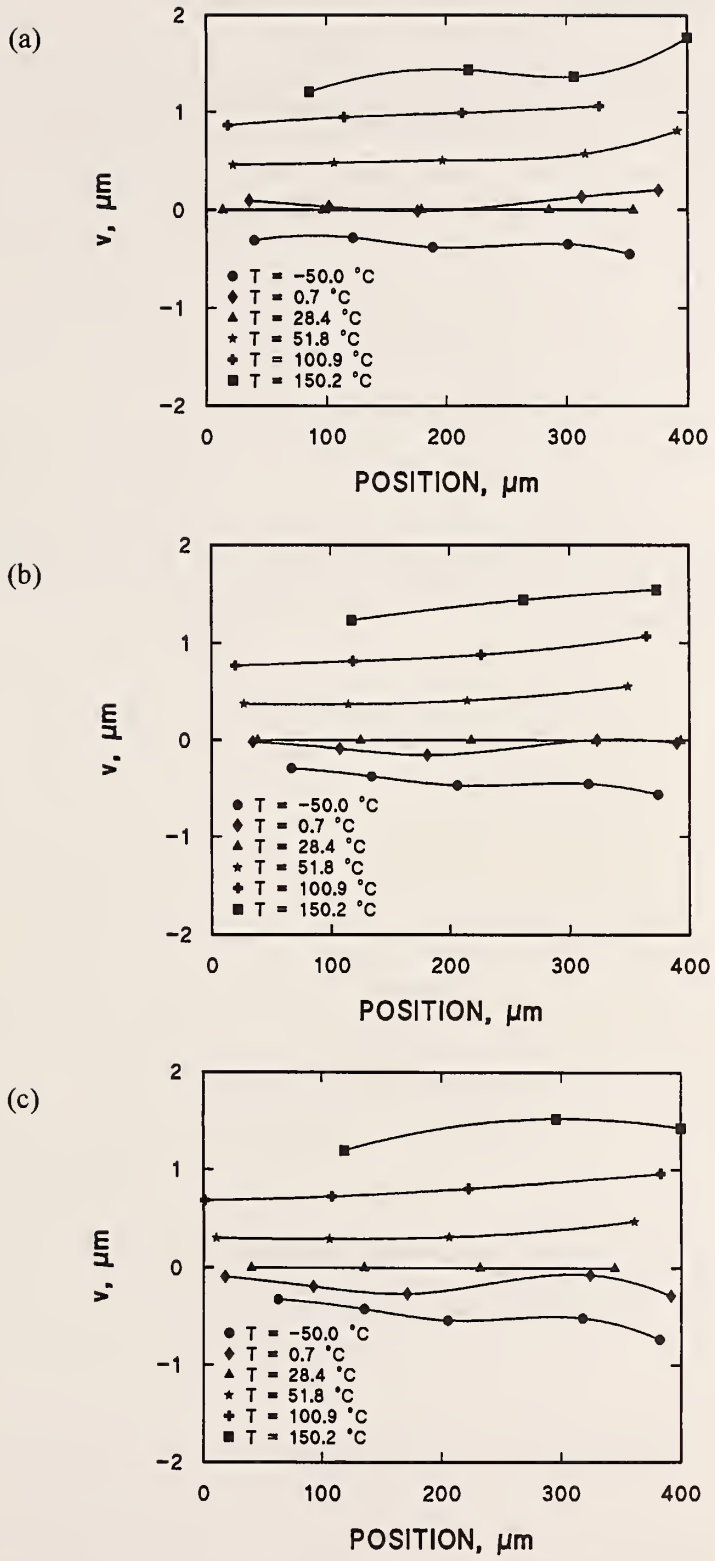

Figure 38. Displacement-versus-position plots of the *v*-field data from the second thermal-loading test on the CA film specimen from the (a) left side; (b) center; and (c) right side of the *v*-field image.

4.8.4 Mechanical Loading of Conductive-Adhesive Film

The mechanical loading of the film specimen resulted in many of the same effects as those observed in the mechanical test on the paste specimen. Insignificant normal strains were observed in the *u*-field or *v*-field images (figs. 39 and 40). However, very little load (246 N) was applied to the specimen before the fringes were no longer traceable in the CA (fig. 41a). At this load, the fringes in the 0.4 mm and the 9.5 mm copper were no longer parallel (see fig. 41b), indicating that significant deformation had occurred in the CA. When the magnification was decreased (see fig. 42), enough shear had taken place to displace the 0.4 mm copper upward with respect to the 9.5 mm copper (note the relative displacement of the grating edges). The specimen continued to carry the load without catastrophic failure, and the images were collected in ~85 N increments to nearly 600 N. At this point, the specimen was no longer carrying the load but was yielding in the 0.4 mm copper (see fig. 43). Data were not available from within the CA from 246 N and beyond, but the *du/dy* data from the first three load increments (fig. 44a) show that the shear strain increased markedly with each load increment. In contrast, the *dv/dx* data (fig. 44b) from the 0.4 mm copper show that the shear strains barely changed with each load increment until the 537 N load was achieved. The slope increased significantly at that load, with evidence pointing to greater shear strains as the center of the specimen was approached.

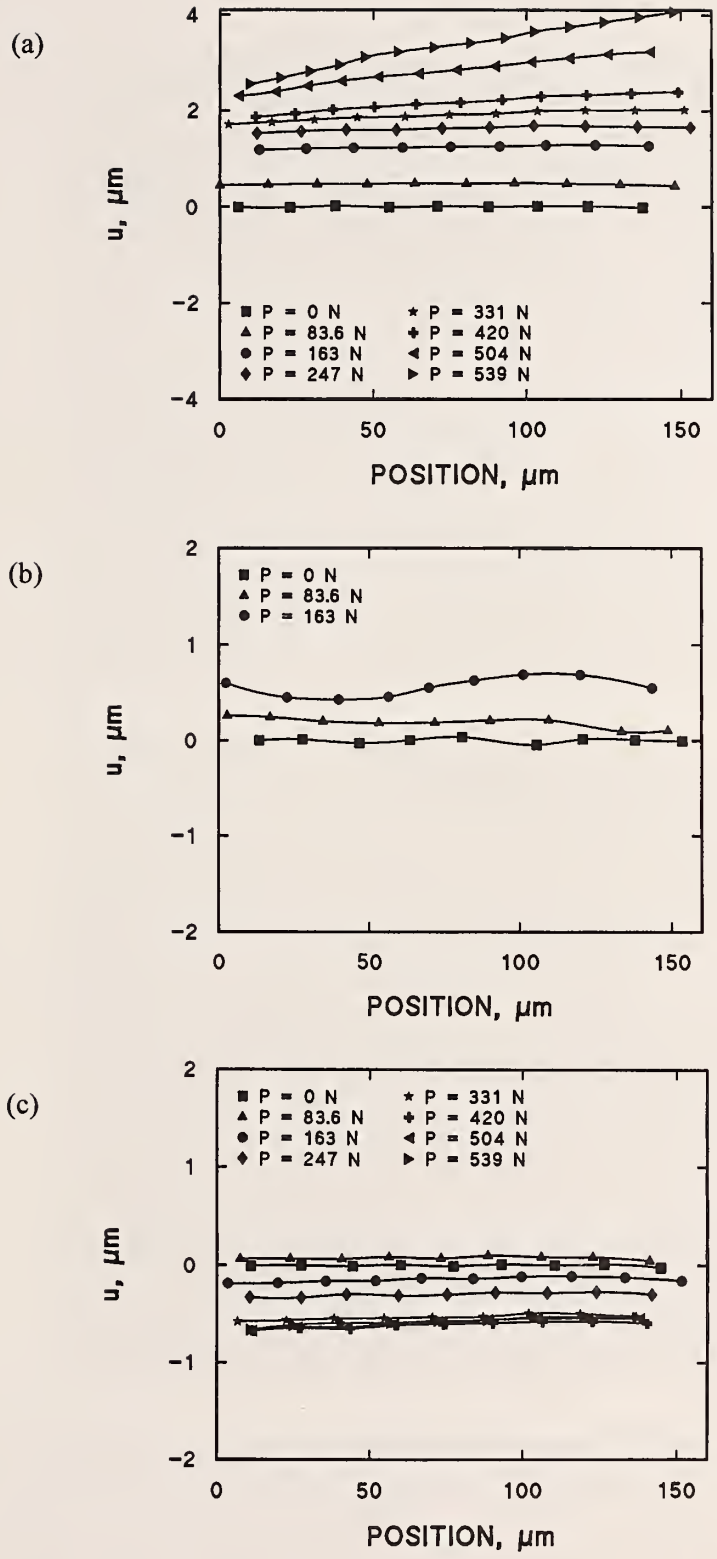

Figure 39. Displacement-versus-position plots of the *u*-field data from the mechanical-loading test on the CA film specimen from (a) the 0.4 mm thick copper; (b) the CA; and (c) the 9.5 mm thick copper.

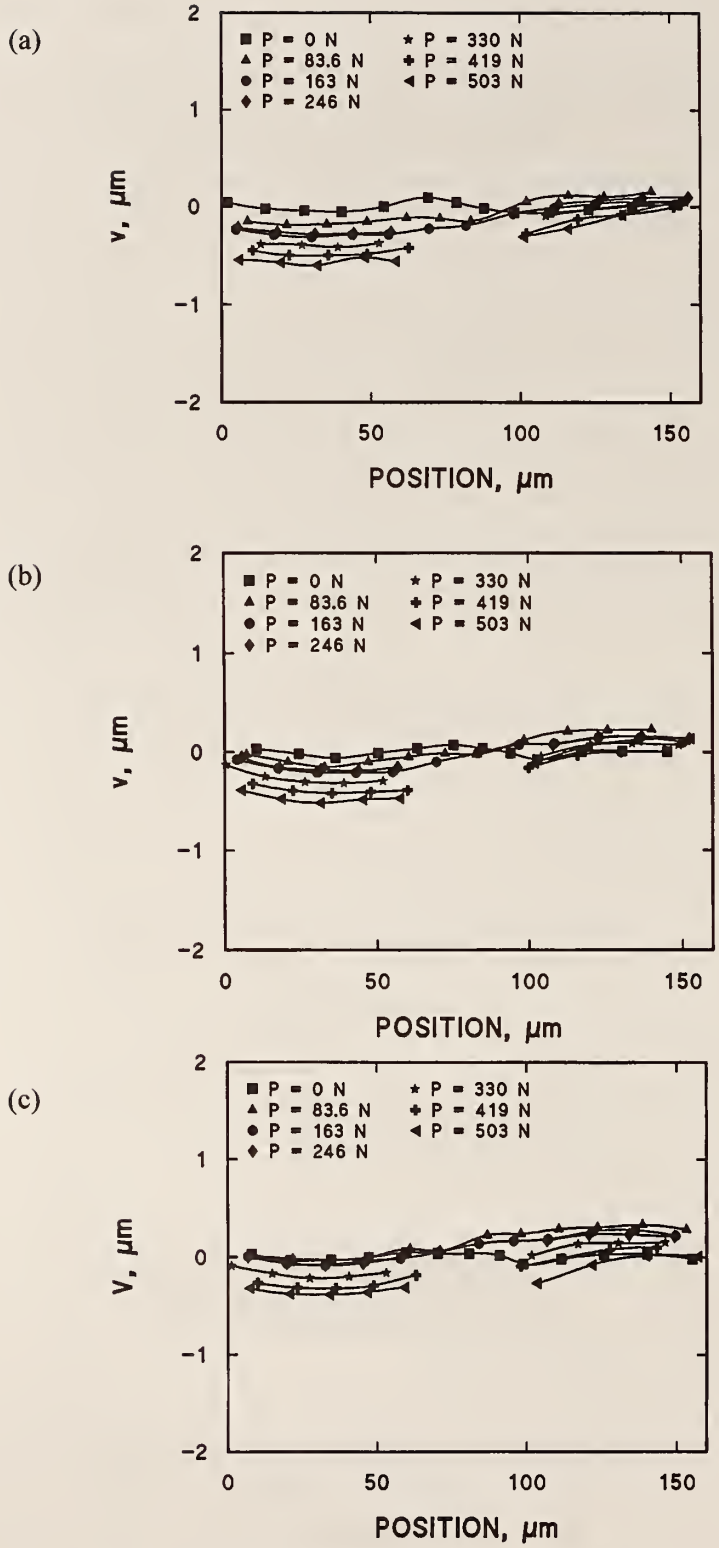

Figure 40. Displacement-versus-position plots of the *v*-field data from the mechanical-loading test on the CA film specimen from the (a) left side; (b) center; and (c) right side of the *v*-field image.

(a)

(b)

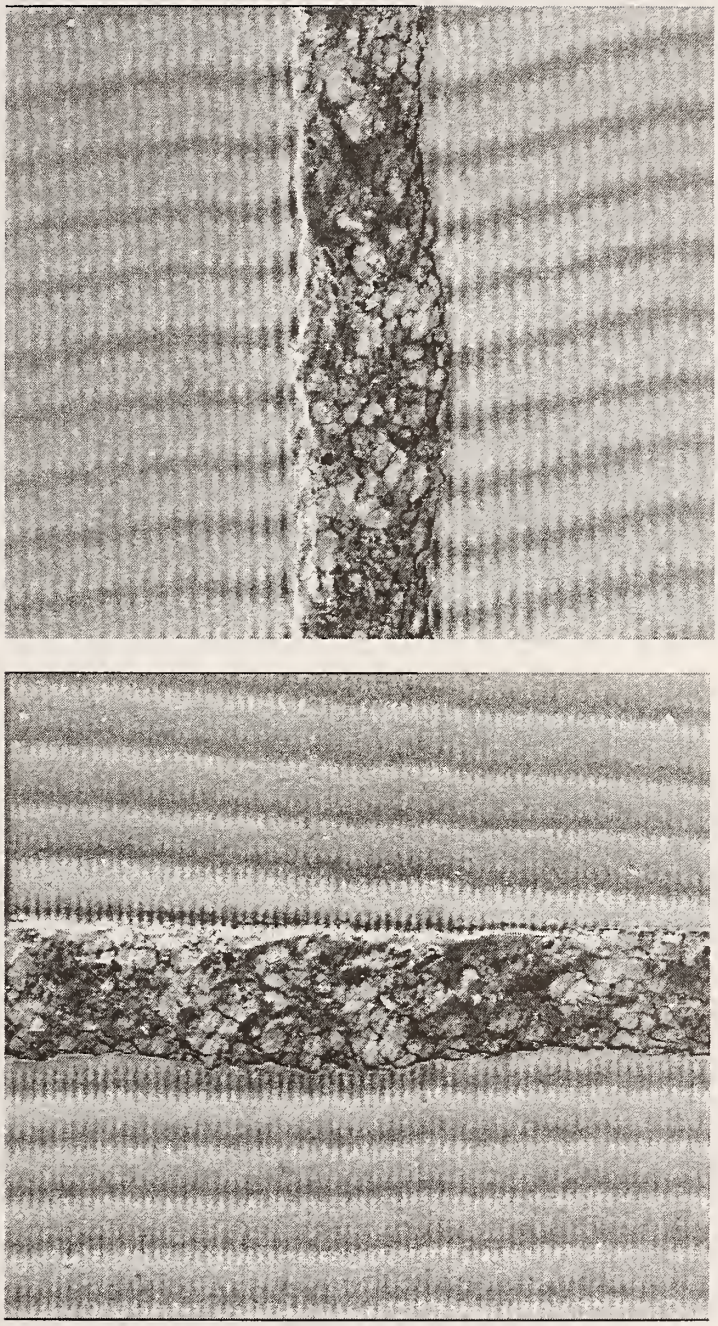

Figure 41. Images at 550× of the (a) *u*-field and (b) *v*-field fringe fields from the mechanical-loading test on the CA film specimen acquired at a load of 247 N.

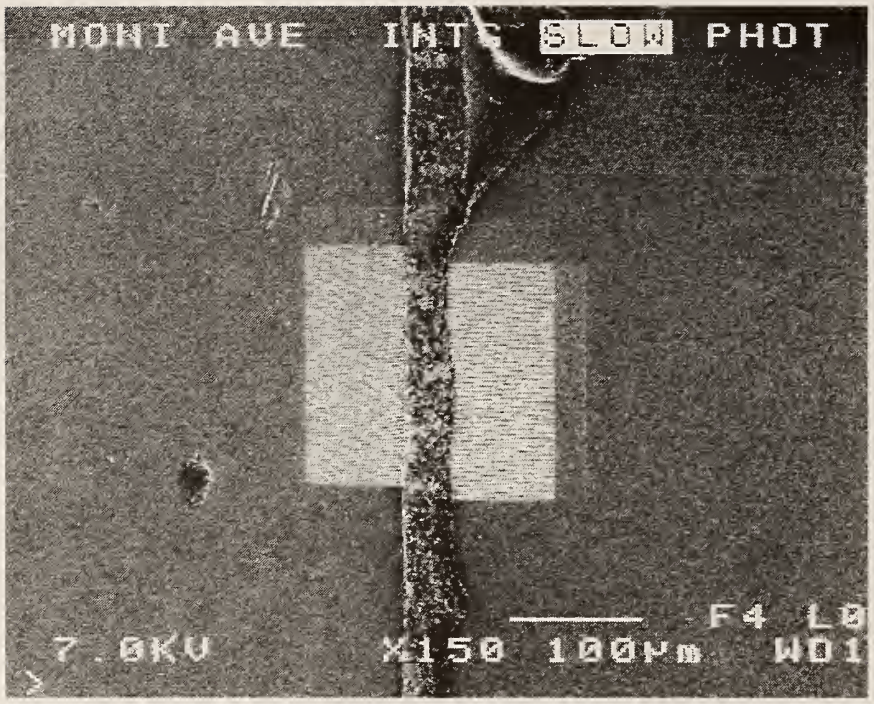

Figure 42. The pattern (150×) on the CA film specimen during the mechanical-loading test.

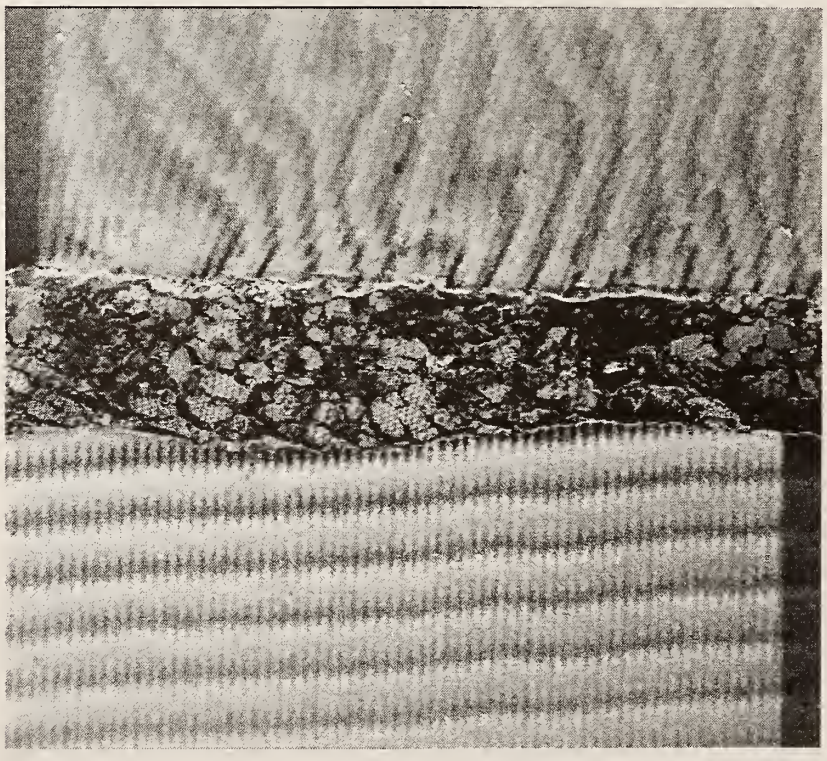

Figure 43. Image of the *v*-field moiré pattern (550×) during the mechanical-loading test on the CA film specimen at a load of 537 N.

(a)

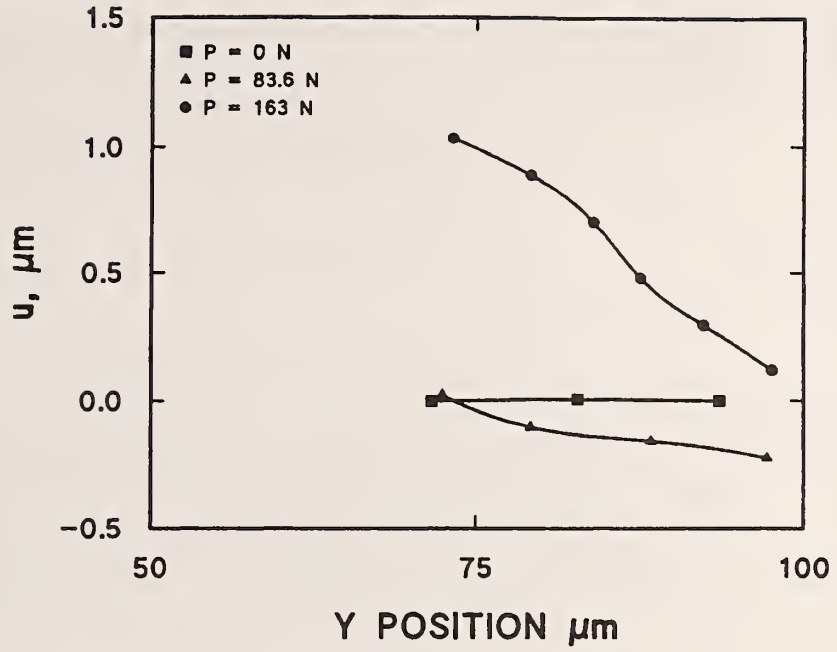

(b)

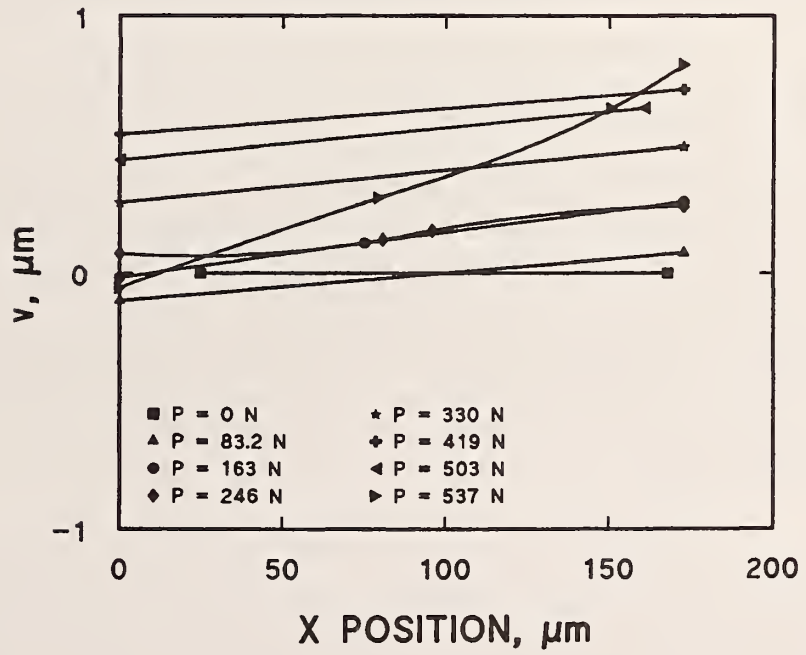

Figure 44. Shear (a) *du/dy* data across the CA film from the first three loads and (b) *dv/dx* data from the 0.4 mm thick copper.

5. Summary and Conclusions

Since its inception, e-beam moiré has grown and developed. The most significant advancement has been the development of crossed-line gratings. Shear strains as well as v-field normal strains can now be calculated from the data obtained from the crossed-line gratings.

Advances have also been made pertaining to the hardware associated with e-beam moiré. Cooling has been added to the capabilities, with the added advantage of a properly grounded and thermally controlled stage. With the new control box, 90° rotation is now precise and routine.

The technique has been proven, benchmarked for credibility, and analyzed for source and magnitude of error. Potential applications to which the technique might be implemented are as varied as materials science problems. The technique could be useful when applied to problems as diverse as crack-tip propagation and adhesion.

The experiments conducted on the two forms of isotropically conductive adhesives yielded useful information on the behavior of these materials under these testing conditions. Both CAs performed well under the imposed thermal loading conditions. Despite exceeding the T_g for each material and the regions of great expansion that resulted, the materials did not debond at the copper/CA interface, nor did the silver particles shift or rotate. The CAs remained stiff enough at the higher temperatures to function as they were designed in this specimen.

If these materials are to replace solder in fine-pitch applications, a concern is that they retain the deformation induced at 100 °C. The bending magnitude of the fringes in the CA after thermal cycling (shown in fig. 34) is approximately half a fringe or 225 nm for a pattern that has $p_s \approx 450$ nm. At the end of the thermal-loading test an image was again acquired at approximately room temperature. Figure 45 shows that the shift through the CA was nearly a full fringe in this final image from the thermal-loading test. Indications are that the deformation did not continue to accumulate at the same rate, however, because the final image from the second thermal-loading test of the same specimen showed that the fringe shift had the same magnitude at the end of the test as it had at the start. Deformations of this magnitude are probably insignificant for a well-placed, properly aligned SMD with a lead pitch of 300 μm. If pitches continue to decrease, these deformations will eventually lead to failed components.

The question that remains unanswered from this thermal-loading test is: How will the CA behave under multiple thermal loadings? To properly answer this question, it would be necessary to devise a specimen that more accurately approximates the actual conditions and materials used in a solder-replacement application. Then the specimen must be thermally fatigued to replicate the conditions encountered by such a device in service.

The mechanical tests revealed some fundamental behavior differences between the conductive adhesive paste and film. The CA paste specimen carried the load to failure with virtually no deformation to the copper and with measurable amounts of shear within the CA. The specimen failed at 8.4 MPa, although the manufacturer predicted a failure shear stress of

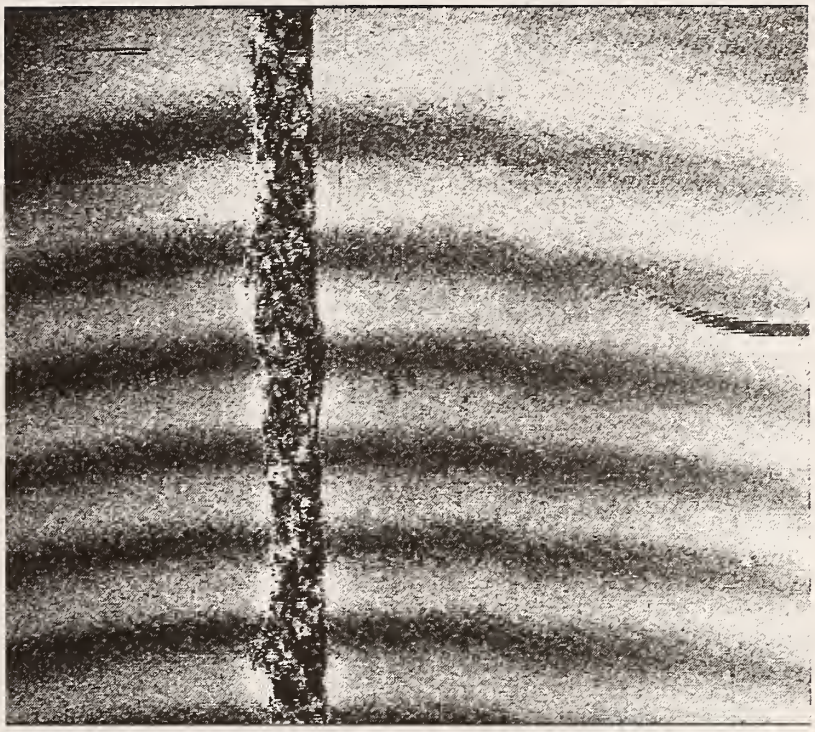

Figure 45. Posttest image at 220× from the first thermal-loading test on the CA film specimen acquired at 29 °C.

11.7 MPa. The only difference between the manufacturer's specification and the test described here was that its shear strength was based on an aluminum-to-aluminum specimen.

A 28% drop in expected shear strength prompts speculation on possible sources. The materials were stored for three months in a standard freezer before being transferred to an ultra-low-temperature freezer. The manufacturer specifies a storage life of six months at –10 °C, and a year at –40 °C for the CA paste. The material should not have degraded in the nine months that it was in storage. The mechanical paste specimen was prepared and instrumented with gratings four times, essentially thermal cycling it four times before any testing was conducted. The thermal-fatigue tests suggested previously may indicate whether thermal cycling affects the shear strength.

The mechanical test on the film specimen revealed glaring inadequacies in the material, as if the film had degraded during storage. The manufacturer suggests that film stored at 5 °C has a shelf life of six months. As with the paste, the film was stored for nine months before the specimen was made, three months in a standard freezer and an additional six months in an ultra-low-temperature freezer.

The film specimen showed curiously contrasting behavior during the test. Although damage occurred in the CA at low loads, catastrophic failure of the CA never occurred in

this test. The CA continued yielding until the strain, carried entirely by the CA, was sufficient to induce yield in the copper, and once the copper started yielding and the CA no longer carried the load, the test was over. The manufacturer predicted a shear strength of 17.2 MPa for an aluminum-to-aluminum specimen. Although loads never approached this level, the CA never actually failed mechanically.

Although the CA never actually failed, damage had occurred. Evaluating the specimen for use as a solder replacement requires determining not only whether it has adequate mechanical strength but also whether it maintains a conducting path during that loading. Although this specimen was not designed to evaluate both situations, figure 46 clearly shows that the conducting path, at least locally, has been compromised. The darker areas are the epoxy matrix; the area to the right is the 9.5 mm copper, and the irregularly shaped areas are the conducting silver particles. The ubiquitous array of dots is the crossed-line grating. The silver particle in the center of the image broke away from the epoxy, isolating it from the copper. As a result, in this image, a conducting path no longer exists between the copper and the conducting silver particles.

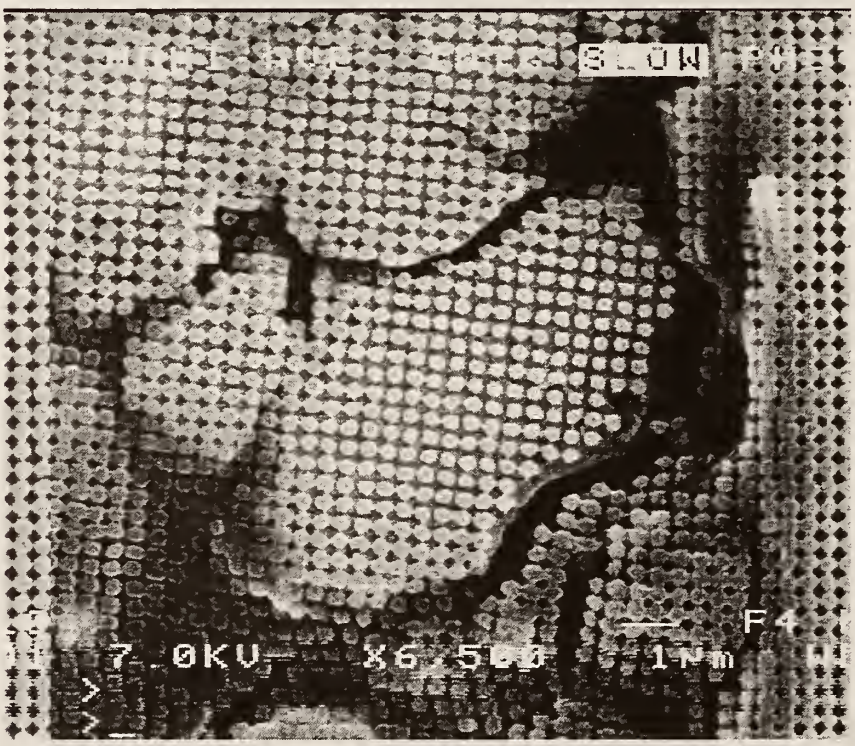

Figure 46. Image of the CA film at 6500× obtained at the 328 N load during the mechanical-loading test.

The author acknowledges David Read (NIST) and James Dally for development of the technique and advice on its use; and David Matlock, Ivar Reimanis, and John Berger (Colorado School of Mines) for their helpful comments and suggestions. I also thank Ablestick, A. I. Technology, and the 3M Corporation for responding to my request for conductive adhesive materials to study.

6. References

[1] Tollenaar, D. Moire—Interferentieverschijnselen bij rasterdruk. Amsterdam: Amsterdam Instituut voor Grafische Technick; 1945.

[2] Weller, R.; Shepard, B.M. Displacement measurement by mechanical interferometry. Proc., SESA 6; 1948.

[3] Kaczer, J.; Kroupa, F. The determination of strains by mechanical interference. Czechoslovak J. Phys. 1: 80 pp.; 1952.

[4] Lehman, R.; Wiemer, A. Untersuchungen zur Theorie der Doppelraster als Mittel zur Messanzeige. Feingerätetechnik Heft: 5–199; 1953.

[5] Vinckier, A.; Dechaene, R. Use of moiré effect to measure plastic strains. J. Basic Eng. 82: 426–434; 1960.

[6] Dantu, M. Recherches Diverses d'Extensometrie et de Détermination des Contraintes. Proc., conference held at GAMAC; 1954.

[7] Dantu, M. Utilisation des Réseaux pour l'Étude des Déformations. Publication 57-6. Laboratorie Central des Ponts et Chaussées; 1957.

[8] Dally, J.W.; Riley, W.F. Moiré methods, chapter 11 in Experimental stress analysis. New York: McGraw–Hill; 1991. 389–423.

[9] Durelli, A.J.; Parks, V.J. Moiré analysis of strain. Englewood Cliffs, NJ: Prentice–Hall; 1970. 399 pp.

[10] Post, D. Moiré interferometry. A.S. Kobayashi, ed. Handbook on experimental mechanics. Englewood Cliffs, NJ: Prentice–Hall; 1987. 317–387.

[11] Han, B.-T.; Post, D. Immersion interferometer for microscopic moiré interferometry. Exp. Mech. 32: 38–41; 1992.

[12] Robinson, D.W. High resolution moiré contouring by a hybrid technique combining light and electron optics. Opt. Laser Technol. 13: 145–149; 1981.

[13] Kishimoto, S.; Egashire, M.; Shina, N. Measurements of grain boundary sliding and observations of microgrids for high temperature use. J. Soc. Mater. Sci. Jpn. 40: 637–641; 1991.

[14] Dally, J.W.; Read, D.T. Electron-beam moiré. Exp. Mech. 33: 270–277; 1993.

[15] Read, D.T.; Dally, J.W. Electron-beam moiré study of fracture of a glass fiber reinforced plastic composite. Trans. Amer. Soc. Mech. Eng. 61: 402–409; 1994.

[16] Read, D.T.; Dally, J.W. Theory of electron-beam moiré. J. Res. Natl. Inst. Stand. Technol. 101: 47–61; 1996.

[17] Read, D.T.; Drexler, E.S. Local deformation of plated through holes under thermo-mechanical loading. Sehen, M.A.; Alop, H.; Suhir, E., eds. Proc., ASME 1994 international mechanical engineering congress and exposition, Mechanics and materials for electronic packaging, Vol. 2: Thermal and mechanical behavior and modeling, AMD-187; 1994 Nov. 6–11; Chicago, IL. New York: ASME; 1994. 185–194.

[18] Morimoto, Y.; Hayashi, T. Deformation measurement during powder compaction with a scanning moiré method. Exp. Mech. 24: 112–116; 1984.

[19] Tiberio, R. Personal communication. National Nanofabrication Facility, Cornell University, Ithaca, New York; 1995.

[20] Berger, J.R.; Drexler, E.S. Error analysis and thermal expansion measurement with electron-beam moiré. Exp. Mech. 38: 167–171; 1998.

[21] Bowles, D.E.; Post, D.; Herakovich, C.T.; Tenney, D.R. Moiré interferometry for thermal expansion of composites. Exp. Mech. 21: 441–447; 1981.

[22] Lide, D.R., ed. Handbook of chemistry and physics, 74th edition. Boca Raton, FL: CRC Press.; 1993.

[23] Gilleo, K. Evaluating polymer solders for lead-free assembly, Part I. Circuits Assem. 5: 52–54, 56; 1994.

[24] Gilleo, K. Assembly with conductive adhesives. Soldering Surface Mount Technol. No. 19: 12–17; 1995.

[25] Guy, J. Manufacturing 25 mil pitch surface mount assemblies using conductive adhesives. Proc., technical program of NEPCON East; 1994. 374–380.

[26] Harris, P.G. Conductive adhesives: A critical review of progress to date. Soldering Surface Mount Technol. No. 20: 19–21, 26; 1995.

[27] Chang, D.D.; Crawford, P.A.; Fulton, J.A.; McBride, R.; Schmidt, M.B.; Sinitski, R.E.; Wong, C.P. An overview and evaluation of anisotropically conductive adhesive films for fine pitch electronic assembly. IEEE Trans. Components Hybrids Mfg. Technol. 16: 828–835; 1993.

[28] Alpert, B.T.; Schoenberg, A.J. Conducting adhesives as a soldering alternative. Electron. Packag. Prod. 31: 130–132; 1991.

[29] Barbieri, R.; Coppari, G.; Rudland, D. The use of adhesive technology in the replacement of solder for the manufacture of the new Fiat 500 ignition system. Proc., Electro '94 international conference; 1994. 879–884.

[30] Buchoff, L.S. Advanced non-soldering interconnection. Electro Int. Conf. Rec. 16: 248–251; 1991.

[31] Burkhart, A. New epoxies for advanced surface mount applications. Proc., technical program of the surface mount international conference and exposition; 1991 August 27–29. 285–294.

[32] Gaynes, M.A.; Lewis, R.H. Evaluation of contact resistance for isotropic electrically conductive adhesives. Proc., 7th international SAMPE electronics conference, Vol. 7; 1994. 69–78.

[33] Gaynes, M.A.; Lewis, R.H.; Saraf, R.F.; Roldan, J.M. Evaluation of contact resistance for isotropic electrically conductive adhesives. IEEE Trans. Components Packag. Mfg. Technol., Part B 18: 299–304; 1995.

[34] Greaves, J.B., Jr. Evaluation of solder alternatives for surface mount technology. Proc., technical program of NEPCON West; 1993. 1479–1488.

[35] Guy, J. Dealing with the issues of lead solder replacements. Proc., technical program of NEPCON West, Vol. 2; 1995. 1066–1076.

[36] Honoré, J.P.; Rubin, H.D.; Zierold, M.K. Reliability testing of conductive adhesives. Proc., technical program of NEPCON West, Vol. 3; 1992 February 23–27; Anaheim, CA; 1992. 1372–1380.

[37] Hvims, H.L. Solder replacement. Proc., 15th IEEE/CHMT international electronics manufacturing technology symposium; 1993. 128–135.

[38] Hvims, H.L. Conductive adhesives as a solder replacement for surface mount assembly. Proc., technical program of surface mount international conference and exposition; 1994 August 28–September 1; San Jose, CA. Edina, MN: Surface Mount International; 1994. 313–325.

[39] Hvims, H.L. Solder replacement. Soldering Surface Mount Technol. No. 17: 12–19; 1994.

[40] Hvims, H.L. Testing of a solder replacement technology. Qual. Rel. Eng. Int. 10: 423–434; 1994.

[41] Hvims, H.L. Conductive adhesives for SMT and potential applications. IEEE Trans. Components Packag. Mfg. Technol., Part B 18: 284–291; 1995.

[42] Keusseyan, R.L.; Dilday, J.L. Electric contact phenomena in conductive adhesive connections. Proc., technical program of the surface mount international conference and exposition; 1993 August 31–September 2; San Jose, CA. Edina, MN: Surface Mount International; 1993. 567–571.

[43] Keusseyan, R.L.; Dilday, J.L. Electric contact phenomena in conductive adhesive interconnections. Proc., ISHM; 1993. 44–49.

[44] Keusseyan, R.L.; Dilday, J.L.; Speck, B.S. Electric contact phenomena in conductive adhesive interconnections. Int. J. Microcircuits Electron. Packag. 17: 236–242; 1994.

[45] Keusseyan, R.L.; Goeller, P.T.; Dilday, J.L.; Waterman, L.L.; Dellis, L.E.; Thrash, J.R.; Critzer, M.S. Thermal cycling reliability of interconnections to low temperature fired–cofired ceramics. Proc., ISHM '91, 1991 international symposium on microelectronics; 1991 October 21–23; Orlando, FL; 1991. 493–497.

[46] Keusseyan, R.L.; LaBranche, M.H.; Hang, K.W. Thick film multilayer material systems for thermal cycle applications. Proc., 27th international symposium on microelectronics, SPIE proceedings series Vol. 2369; 1994 November 15–19; Boston, MA; 1994. 185–190.

[47] Li, L.; Lizzul, C.; Kim, H.; Sacolick, I.; Morris, J.E. Electrical, structural, and processing properties of electrically conductive adhesives. IEEE Trans. Components Hybrids Mfg. Technol. 16: 843–851; 1993.

[48] Li, L.; Morris, J.E. Structure and selection models for anisotropic conductive adhesive films. J. Electron. Mfg. 5: 9–17; 1995.

[49] Liotine, F., Jr. Surface mount solderless attachment using electrically conductive polymer adhesive technology. Proc., technical program of the surface mount international conference and exposition; 1993 August 31–September 2; San Jose, CA. Edina, MN: Surface Mount International; 1993. 572–583.

[50] Liu, J.; Ljungkrona, L.; Lai, Z. Development of conductive adhesive joining for surface-mount electronics manufacturing. IEEE Trans. Components Packag. Mfg. Technol., Part B 18: 313–319; 1995.

[51] Nguyen, G.P.; Williams, J.R.; Gibson, F.W.; Winster, T. Electrical reliability of conductive adhesive for surface-mount applications. Proc., technical program the surface mount international conference and exposition; 1993 August 31–September 2; San Jose, CA; 1993. 561–566.

[52] Rörgren, R.S.; Liu, J. Reliability assessment of isotropically conductive adhesive joints in surface mount applications. IEEE Trans. Components Packag. Mfg. Technol., Part B 18: 305–312; 1995.

[53] Stam, F.; O'Grady, P.; Barrett, J. Characterisation and reliability study of anisotropic conductive adhesives for fine pitch package assembly. J. Electron. Mfg. 5: 1–8; 1995.

[54] Savolainen, P.; Kivilahti, J. Feasibility of some lead-free solder alloys as filler materials for Z-axis adhesives. Soldering Surface Mount Technol. No. 20: 10–12; 1995.

[55] Basavanhally, N.R.; Chang, D.D.; Cranston, B.H. Direct chip interconnect with adhesive-conductor films. Proc., 42nd Electronic components and technology conference; 1992. 487–491.

[56] Basavanhally, N.R.; Chang, D.D.; Cranston, B.; Segar, S.G., Jr. Direct chip interconnect with adhesive conductor films. IEEE Trans. Components Hybrids Mfg. Technol. 15: 972–976; 1992.

[57] Buratynski, E.K. Thermomechanical modeling of direct chip interconnection assembly. Trans. Amer. Soc. Mech. Eng.—J. Electron. Packag. 115: 382–391; 1993.

[58] Chang, D.D.; Fulton, J.A.; Lyons, A.M.; Nis, J.R. Design considerations for the implementation of anisotropic conductive adhesive interconnection. Proc., technical program of NEPCON West '92, Vol. 3; 1992 February 23–27; Anaheim, CA; 1992. 1381–1389.

[59] Chung, K.; Fleishman, R.; Bendorovich, D.; Yan, M. Z-poxy as solder replacement for surface mounting applications. Proc., international symposium on microelectronics, SPIE, Vol. 1847; 1992. 518–522.

[60] Ferguson, P.; Newton, P.G. Cost effective SMT assembly on flexible circuits using polymer solder. Proc., technical program of surface mount international; 1994. 326–330.

[61] Gilleo, K. Direct chip interconnect using polymer bonding. IEEE Trans. Components Hybrids Mfg. Technol. 13: 229–234; 1990.

[62] Gilleo, K. Intrinsically clean polymer bonding: What are the trade-offs? Proc., technical program of the surface mount international conference and exposition; 1993 August 31–September 2; San Jose, CA. Edina, MN: Surface Mount Technology; 1993. 655–661.

[63] Hogerton, P.B.; Carlson, K.E.; Hall, J.B.; Krause, L.J.; Tingerthal, J.M. An evaluation of a heat-bondable, anisotropically-conductive adhesive as an interconnection medium for flexible printed circuitry. Proc., IEPS technical conference; 1990. 1026–1033.

[64] Jin, S.; Tiefel, H.; Chen, L.-H.; Dahringer, D.W. Anisotropically conductive polymer films with a uniform dispersion of particles. IEEE Trans. Components Hybrids Mfg. Technol. 16: 972–977; 1993.

[65] Kreutter, N.P.; Grove, B.K.; Hogerton, P.B.; Jensen, C.R. Effective polymer adhesives for interconnect. Proc., 7th electronic materials and processing congress; 1992 August 24–27; Cambridge, MA; 1992. 249–256.

[66] Lee, C.H.; Loh, K.I. Fine pitch COG interconnections using anisotropically conductive adhesives. Proc., 45th electronic components and technology conference; 1995 May 21–24; Las Vegas, NV; 1995. 121–125.

[67] Lee, C. H.; Loh, K. I.; Wu, F.-J. Flip chip-on-glass with anisotropically conductive adhesives. Electron. Packag. Prod. 35: 74–76, 78; 1995.

[68] Liu, J. Reliability of surface-mounted anisotropically conductive adhesive joints. Circuit World 19: 4–11, 15; 1993.

[69] Liu, J.; Rörgren, R. Joining of displays using thermosetting anisotropically conductive adhesives. J. Electron. Mfg. 3: 205–214; 1993.

[70] Liu, J.; Rörgren, R.; Ljungkrona, L. High volume electronics manufacturing using conductive adhesives for surface mounting. Proc., technical program of surface mount international; 1994. 291–302.

[71] Savolainen, P.; Kivilahti, J. Electrical properties of solder filled anisotropically conductive adhesives. J. Electron. Mfg. 5: 19–26; 1995.

[72] Wong, M. Anisotropically conductive adhesive interconnects—a case study. Proc., technical program of the surface mount international conference and exposition; 1991 August 27–29; San Jose, CA. Edina, MN: Surface Mount International; 1991. 308–310.

[73] Gilleo, K. Solderless assembly reduces cost, hazards, and pollution. J. Electron. Mfg. 2: 37–41; 1992.

[74] Gilleo, K. The polymer electronics revolution. Proc., technical program of NEPCON West '2; 1992 February 23–27; Anaheim, CA; 1992. 1390–1401.

[75] Conway, P.P. An environmental comparison of solder and conductive adhesives for SMT interconnect. 15th IEEE/CHMT international electronics manufacturing technology symposium; 1993. 171–176.

[76] Chang, D.D.; Fulton, J.A.; Ling, H.C.; Schmidt, M.B.; Sinitski, R.E.; Wong, C.P. Accelerated life test of Z-axis conductive adhesives. IEEE Trans. Components Hybrids Mfg. Technol. 16: 836–842; 1993.

[77] Gilleo, K. Are polymer solders the answer to lead-free assembly? Surface Mount Technol. 9: 39, 42–45; 1995.

[78] Goward, J.M.; Whalley, D.C.; Williams, D.J. Conducting adhesives for high density interconnection. Institute of electrical engineers colloquium on interconnection technology; London, England. Digest No. 1994/Issue 220: 2/1–2/4; 1994.

[79] Gilleo, K.; Cinque, T.; Corbett, S.; Lee, C. Thermoplastic adhesives—the attachment solution for multichip modules. Proc., international electronics packaging conference, IPES; San Diego, CA; 1993. 233–242.

[80] Li, L.; Morris, J.E.; Liu, J.; Lai, Z.; Ljungkrona, L.; Li, C. Reliability and failure mechanism of isotropically conductive adhesive joints. Proc., 45th electronic components and technology conference; 1995 May 21–24; Las Vegas, NV; 1995. 114–120.

[81] Nguyen, G.P.; Williams, J.R.; Gibson, F.W. Conductive adhesives: Reliable and economical alternatives to solder paste for electrical applications. Proc., IEPS technical conference, Vol. 1; 1992. 723–731.

[82] Nguyen, G.P.; Williams, J.R.; Gibson, F.W. Conductive adhesives. Circuits Assembly 4: 36–38, 41; 1993.

[83] Nguyen, G.P.; Williams, J.R.; Gibson, F.W. Conductive adhesives: Reliable and economical alternatives to solder paste for electrical applications. Proc., international symposium on microelectronics, SPIE Vol. 1847; 1992. 510–517.

[84] Rusanen, O.; Lenkkeri, J. Reliability issues of replacing solder with conductive adhesives in power modules. IEEE Trans. Components Packag. Mfg. Technol.—Part B 18: 320–325; 1995.

[85] Chung, K.; Dreier, G.; Fitzgerald, P.; Boyle, A.; Lin, M.; Sager, J. Z-axis conductive adhesive for TAB and fine pitch interconnects. Proc., 41st conference on electronic components and technology; 1991. 345–354.

[86] Chung, K.; Fleishman, R.; Bendorovich, D.; Yan, M.; Mescia, N. Z-axis conductive adhesives for fine-pitch interconnection. Proc., technical program of the international electronics packaging conference, Vol. 1; 1992. 678–689.

[87] Chung, K.; Devereaux, T.; Monti, C.; Yan, M.; Mescia, N. Z-axis conductive adhesives as solder replacement. Proc., technical program of the surface mount international conference and exposition; 1993 August 31–September 2; San Jose, CA. Edina, MN: Surface Mount International; 1993. 554–560.

[88] Chung, K.; Devereaux, T.; Monti, C.; Yan, M. Z-axis conductive adhesives as solder replacement. Rasmussen, B.; Wegman, R.; Hirt, A.; Rossi, R., eds. Proc., 7th international SAMPE electronics conference, Vol. 7. Critical materials and processes in a changing world. Corvina, CA: SAMPE; 1994. 473–481.

[89] Lenkkeri, J.; Rusanen, O. Conductive adhesives as die-bonding materials for power electric modules. J. Electron. Mfg. 3: 199–204; 1993.

[90] Adell, J.A.; Molina, M.; Cavero, J.M. Adhesives for electronic applications. Hybrid Circuits No. 31: 54–56; 1993.

[91] Adell, J.A.; Molina, M.; Cavero, J.M.; Mino. E. Adhesives for electronic application. Proc., 20th international conference on microelectronics; 1992. 451–453.

[92] Kang, S.K.; Graham, T.; Purushothaman, S.; Roldan, J.; Saraf, R. New high conductivity lead (Pb)-free conducting adhesives. Proc., 1995 IEEE international symposium on electronics and the environment—ISEE; 1995. 177–181.

[93] Parks, V.J. Geometric moiré, in Handbook on experimental mechanics. Kobayashi, A.S., ed. Englewood Cliffs, NJ: Prentice–Hall; 1987. 282–313.

7. Bibliography

Bolger, J.C.; Gilleo, K. Area bonding conductive epoxy adhesive preforms for grid array and MCM substrate attach. Proc., IEEE multichip module conference; 1994 March 15–17; Santa Cruz, CA; 1994. 77–82.

Bolger, J.C.; Reynolds, M.; Popielarczyk, J. Area bonding conductive (ABC) adhesives for flex circuit connection to LTCC/MCM substrates. Proc., 45th electronic components and technology conference; 1995 May 21–24; Las Vegas, NV; 1995. 529–533.

Date, H.; Hozumi, Y.; Tokuhira, H.; Usui, M.; Horikoshi, E.; Sato, T. Anisotropic conductive adhesive for fine pitch interconnections. Proc., 27th international symposium on microelectronics; 1994 November 15–17; Boston, MA. SPIE proceedings series Vol. 2369; 1994. 570–575.

Dion, J.; Borgesen, P.; Yost, B,; Lilienfeld, D.A.; Li, C.-Y. 1994. Materials and reliability considerations for anisotropically conductive adhesive based interconnects. Børgesen, P.; Jensen, K.F.; Pollack, R.A., eds. Electronic packaging materials science VII. Proc., Materials research society symposium; 1994 November 29–December 3; Boston, MA. Pittsburgh, PA: Materials Research Society, Vol. 323; 1994. 27–32.

Frear, D.R. The mechanical behavior of interconnect materials for electronic packaging. J. Met. 48: 49–53; 1996.

Gengel, G. A process for the manufacture of cost competitive MCM substrates. Proc., international conference on multichip modules; 1994 April 13–15; Denver, CO. 1994; 182–187.

Gilleo, K. A new multilayer circuit process based on anisotropicity. Proc., technical program of NEPCON West; 1990. 8–31.

Gilleo, K. Polymer bonding systems offer alternatives to soldering. Electron. Packag. Prod. 32: 52–54, 56; 1992.

Gilleo, K. Adhesives/epoxies and dispensing. Surface Mount Technol. 8: 54-61; 1994.

Gilleo, K. Assembly with conductive adhesives. Proc., technical program of surface mount international conference and exposition; 1994 August 28–September 1; San Jose, CA. Edina, MN: Surface Mount International; 1994. 279–288.

Gilleo, K. Evaluating polymer solders for lead-free assembly, Part II. Circuits Assem. 5: 50–53; 1994.

Gilleo, K. Organic solders take on new shapes. Rasmussen, B.; Wegman, R.; Hirt, A.; Rossi, R., eds. Critical materials and processes in a changing world, Vol. 7, Proc., 7th international SAMPE electronics conference; 1994 June 20–23; Parsippany, NY. Corvina, CA: SAMPE; 1994. 57–68.

Goward, J.M.; Williams, D.J.; Whalley, D.C. Properties of anisotropic conductive adhesive pastes for fine-pitch surface mount technology. J. Electron. Mfg. 3: 179–190; 1993.

Goward, J.; Williams, D.; Whalley, D. Understanding anisotropic conducting adhesives behavior. Proc., technical program of surface mount international conference and exposition; 1994 August 28–September 1; San Jose, CA. Edina, MN: Surface Mount International; 1994. 303–312.

Howard, C.; Nair, S.; Ang, S.; Schaper, L. An investigation of conductive polymer flip chip attachment in multichip module applications. Proc., 45th electronic components and technology conference; 1995 May 21–24; Las Vegas, NV; 1995. 1244–1249.

Jagt, J.C.; Beris, P.J.M.; Lijten, G.F.C.M. Electrically conductive adhesives: A prospective alternative for SMD soldering? IEEE Trans. Components Packag. Mfg. Technol., Part B 18: 292–298; 1995.

Katz, H.S.; Agarwal, R. Conductive polymer composites as a replacement for conventional lead based solders. Rasmussen, B.; Wegman, R.; Hirt, A.; Rossi, R., eds. Critical materials and processes in a changing world, Vol. 7, Proc., 7th international SAMPE electronics conference; 1994 June 20–23; Parsippany, NY. Corvina, CA: SAMPE; 1994. 44–50.

Li, L.; Chung, D.D.L. Z-axis anisotropic electrically conducting polymer-matrix composite film. Rasmussen, B.; Wegman, R.; Hirt, A.; Rossi, R., eds. Critical materials and processes in a changing world, Vol. 7. Proc., 7th international SAMPE electronics conference; 1994 June 20–23; Parsippany, NY. Corvina, CA: SAMPE; 1994. 482–486.

Lutz, M.A.; Cole, R.L. High performance electrically conductive silicone adhesives. Hybrid Circuits. No. 23: 27–30; 1990.

Lyons, A.M.; Hall, E.E.; Wong, Y.-H.; Adams, G. A new approach to using anisotropically conductive adhesives for flip chip assembly. Proc., 45th electronic components and technology conference; 1995 May 21–24; Las Vegas, NV; 1995. 107–113.

Ogunjimi, A.O.; Boyle, O.; Whalley, D.C.; Williams, D.J. A review of the impact of conductive adhesive technology on interconnection. J. Electron. Mfg. 2: 109–118. 1992.

Pernice, R.F.; Hannafin, J.J.; Estes, R.H. Evaluation of isotropic conductive adhesives for solder replacement. Proc., 27th international symposium on microelectronics; 1994 November 15–17; Boston, MA. SPIE proceedings series Vol. 2369; 1994. 561–569.

Rafanelli, A. J. A mechanical reliability evaluation of several electrically conductive epoxies Part I: Methodology and basic material properties. Proc., winter annual meeting of ASME, Structural analysis in microelectronic and fiber optic systems; EEP Vol. 12; 1995. 67–75.

Rubin, H.-D. Alternate interconnect methods using conductive adhesives. Proc., technical program of the surface mount international conference and exposition; 1993 August 31–September 2; San Jose, CA. Edina, MN: Surface Mount International; 1993. 748–752.

Rusanen, O.; Lenkkeri, J.; Kivimäki, L. The effect of moisture on die attach joints made with silver filled epoxy. Microelectron. Int. No. 37: 25–27; 1995.

Spalding, O. Thermal effects of replacing solder with conductive adhesives. Hybrid Circuits No. 31: 26–28; 1993.

Spitsbergen, J.C. Epoxy resins and electronics reliability. Rasmussen, B.; Wegman, R.; Hirt, A.; Rossi, R., eds. Critical materials and processes in a changing world, Vol. 7, Proc., 7th international SAMPE electronics conference; 1994 June 20–23; Parsippany, NY. Corvina, CA: SAMPE; 1994. 517–525.

Spitsbergen, J.C. Reliability of electronic devices containing epoxy resins. Proc., Electro '95 international electronics conference; 1995. 422–433.

van Noort, H.M.; Kloos, M.J.H.; Schäfer, H.E.A. Anisotropic conductive adhesives for chip on glass and other flip chip applications. J. Electron. Mfg. 5: 27–31; 1995.

Welwyn Systems. Conductive adhesives on trial. Electron. Prod. 23: 19–23; 1994.

NIST Technical Publications

Periodical

Journal of Research of the National Institute of Standards and Technology—Reports NIST research and development in those disciplines of the physical and engineering sciences in which the Institute is active. These include physics, chemistry, engineering, mathematics, and computer sciences. Papers cover a broad range of subjects, with major emphasis on measurement methodology and the basic technology underlying standardization. Also included from time to time are survey articles on topics closely related to the Institute's technical and scientific programs. Issued six times a year.

Nonperiodicals

Monographs—Major contributions to the technical literature on various subjects related to the Institute's scientific and technical activities.

Handbooks—Recommended codes of engineering and industrial practice (including safety codes) developed in cooperation with interested industries, professional organizations, and regulatory bodies.

Special Publications—Include proceedings of conferences sponsored by NIST, NIST annual reports, and other special publications appropriate to this grouping such as wall charts, pocket cards, and bibliographies.

Applied Mathematics Series—Mathematical tables, manuals, and studies of special interest to physicists, engineers, chemists, biologists, mathematicians, computer programmers, and others engaged in scientific and technical work.

National Standard Reference Data Series—Provides quantitative data on the physical and chemical properties of materials, compiled from the world's literature and critically evaluated. Developed under a worldwide program coordinated by NIST under the authority of the National Standard Data Act (Public Law 90-396). NOTE: The Journal of Physical and Chemical Reference Data (JPCRD) is published bi-monthly for NIST by the American Chemical Society (ACS) and the American Institute of Physics (AIP). Subscriptions, reprints, and supplements are available from ACS, 1155 Sixteenth St., NW, Washington, DC 20056.

Building Science Series—Disseminates technical information developed at the Institute on building materials, components, systems, and whole structures. The series presents research results, test methods, and performance criteria related to the structural and environmental functions and the durability and safety characteristics of building elements and systems.

Technical Notes—Studies or reports which are complete in themselves but restrictive in their treatment of a subject. Analogous to monographs but not so comprehensive in scope or definitive in treatment of the subject area. Often serve as a vehicle for final reports of work performed at NIST under the sponsorship of other government agencies.

Voluntary Product Standards—Developed under procedures published by the Department of Commerce in Part 10, Title 15, of the Code of Federal Regulations. The standards establish nationally recognized requirements for products, and provide all concerned interests with a basis for common understanding of the characteristics of the products. NIST administers this program in support of the efforts of private-sector standardizing organizations.

Consumer Information Series—Practical information, based on NIST research and experience, covering areas of interest to the consumer. Easily understandable language and illustrations provide useful background knowledge for shopping in today's technological marketplace.
Order the **above** *NIST publications from: Superintendent of Documents, Government Printing Office, Washington, DC 20402.*
Order the **following** *NIST publications—FIPS and NISTIRs—from the National Technical Information Service, Springfield, VA 22161.*

Federal Information Processing Standards Publications (FIPS PUB)—Publications in this series collectively constitute the Federal Information Processing Standards Register. The Register serves as the official source of information in the Federal Government regarding standards issued by NIST pursuant to the Federal Property and Administrative Services Act of 1949 as amended, Public Law 89-306 (79 Stat. 1127), and as implemented by Executive Order 11717 (38 FR 12315, dated May 11, 1973) and Part 6 of Title 15 CFR (Code of Federal Regulations).

NIST Interagency Reports (NISTIR)—A special series of interim or final reports on work performed by NIST for outside sponsors (both government and non-government). In general, initial distribution is handled by the sponsor; public distribution is by the National Technical Information Service, Springfield, VA 22161, in paper copy or microfiche form.

U.S. Department of Commerce
National Institute of Standards and Technology
325 Broadway
Boulder, Colorado 80303-3337

Official Business
Penalty for Private Use, $300